CZECH TECHNICAL UNIVERSITY IN PRAGUE
Faculty of Nuclear Sciences and Physical Engineering
Department of Physics

Master's Thesis

Photoproduction of J/ψ vector mesons in Pb–Pb ultra-peripheral collisions

Bc. Zuzana Martínez Gajdošová

Supervisor: Mgr. Michal Broz, Ph.D.

Prague, 2019

ČESKÉ VYSOKÉ UČENÍ TECHNICKÉ
V PRAZE
Fakulta jaderná a fyzikálně inženýrská
Katedra fyziky

Diplomová práce

Fotoprodukce vektorových mezonů J/ψ v ultraperiferálních srážkách Pb–Pb

Bc. Zuzana Martínez Gajdošová

Vedoucí práce: Mgr. Michal Broz, Ph.D.

Praha, 2019

Prohlášení

Prohlašuji, že jsem svoji diplomovou práci vypracovala samostatně a použila jsem pouze podklady (literaturu, projekty, SW atd.) uvedené v přiloženém seznamu.

Nemám závažný důvod proti použití tohoto školního díla ve smyslu §60 Zákona č.121/2000 Sb., o právu autorském, o právech souvisejících s právem autorským a o změně některých zákonů (autorský zákon).

V Praze dne ....

Acknowledgements

I would like to express my gratitude to my supervisor, Mgr. Michal Broz Ph.D., for his support, interest in my work, preparing the data sample without which I wouldn't realize this thesis, for his patience and bright advices. Special thanks go to doc. Jesús Guillermo Contreras Nuño Ph.D., for his valuable advices and answers to all my questions. Then I would like to also thank to my colleges for their willingness to consult UPC physics and of course to my sister Katarína Křížková Gajdošová, who in her little spare time was there for me every time. Last but not least I would like to thank to my parents, who would do impossible to support me and help me with everything, to my grandmother, who always shared my happiness of my research and whose optimism and lovely words I will miss very much in my future works. To my husband Javier Martínez Ruiz, who stood by my side with his great support, understanding and kindness during whole realization of my work and studies in University.

Název práce: **Fotoprodukce vektorových mezonů J/ψ v ultraperiferálních srážkách Pb–Pb**

Autor: Bc. Zuzana Martínez Gajdošová

Obor: Experimentální jaderná a částicová fyzika

Druh práce: Diplomová práce

Vedoucí práce: Mgr. Michal Broz, Ph.D.
Katedra fyziky, Fakulta jaderná a fyzikálně inženýrská,
České vysoké učení technické v Praze

Abstrakt: Jedna z mnoha otevřených otázek současné QCD je příčina jevu jaderného stínění. Abychom mohli porozumět tomuto jevu, je důležité studovat gluonové distribuce v jádře při malém x. Existuje mnoho různych modelů, snažících se popsat tyto jevy v QCD, které je potřeba experimentálně ověřit. Jeden z procesů vhodných pro zkoumání gluonové distribuce v jádře je fotoprodukce vektorového mezonu. Měření účinného průřezu tohoto procesu může sloužit jako ověření platnosti jedné nebo více teoretických předpovědí fenoménů v QCD.

V této diplomové práci jsme připravili nástroje potřebné pro výpočet účinného průřezu koherentní a nekoherentní fotoprodukce vektorového mezonu J/ψ, jako jsou určení výtěžku J/ψ, vypočítaní luminozity, určení součinu akceptance a efektivity a odhad souvisejících systematických chyb. Studium, prezentované v této práci bylo provedeno na datech ze srážek Pb–Pb při těžišťové energii $\sqrt{s_{\mathrm{NN}}} = 5.02$ TeV, která byla nabrána během Run 2 na LHC s detektorem ALICE v střední rapiditě.

Klíčová slova: ultra-periferální srážky, ALICE, J/ψ, účinný průřez

Title: **Photoproduction of J/ψ vector mesons in Pb–Pb ultra-peripheral collisions**

Author: Bc. Zuzana Martínez Gajdošová

Abstract: One of the open questions in QCD today is the cause of the shadowing phenomenon in nuclei. To understand this phenomenon it is necessary to study gluon distributions in nuclei at small x. There are several models trying to describe such phenomenon in QCD which have to be experimentally scrutinized and confirmed. One of the suitable processes to investigate gluon distributions in nuclei is the photoproduction of a vector meson. The measurement of its cross section can serve as a verification of one or more theoretical predictions of this QCD phenomenon.

During this Master's Thesis were prepared tools for the calculation of the cross section of the coherent and incoherent photoproduction of the vector meson J/ψ. The studies presented here were performed with data from Pb–Pb collisions at a center-of-mass energy $\sqrt{s_{\mathrm{NN}}} = 5.02$ TeV collected during the Run 2 data-taking period at the LHC with the ALICE detector at mid-rapidity.

Key words: ultra-peripheral collisions, ALICE, J/ψ, cross section

Contents

1 Introduction **19**
- 1.1 Deeply inelastic scattering . . . 19
  - 1.1.1 Bjørken scaling . . . 20
  - 1.1.2 The fruits of the scaling . . . 21
  - 1.1.3 Small-x physics . . . 22
  - 1.1.4 Shadowing . . . 23

2 Ultra-peripheral collisions **29**
- 2.1 Definitions . . . 30
  - 2.1.1 Coordinate system . . . 30
  - 2.1.2 Impact parameter, centrality, multiplicity . . . 30
  - 2.1.3 Cross section . . . 31
  - 2.1.4 Luminosity . . . 31
  - 2.1.5 Rapidity and pseudorapidity . . . 32
- 2.2 The photon flux and processes of UPC . . . 32
  - 2.2.1 The experimental observables of a VM . . . 33
  - 2.2.2 Types of exclusive photoproduction . . . 34
- 2.3 The J/ψ vector meson . . . 35
  - 2.3.1 Discovery . . . 35
  - 2.3.2 Characteristics of J/ψ . . . 36

3 Brief review of models and previous measurements **37**
- 3.1 Models for J/ψ photoproduction in photon-nucleus interactions . . . 37
  - 3.1.1 A. Adeluyi and C.A. Bertulani (AB) model . . . 37
  - 3.1.2 V. Rebyakova, M. Strikman, M. Zhalov (RSZ) model . . . 38
  - 3.1.3 V.P. Goncalves and M.V.T. Machado (GM) model . . . 40
  - 3.1.4 A. Cisek, W. Schäfer and A. Szczurek (CSS) model . . . 40
  - 3.1.5 T. Lappi and H. Mäntysaari (LM) model . . . 41
  - 3.1.6 STARLIGHT by Spencer R. Klein and Joakim Nystrand . . . 41
- 3.2 Photoproduction of J/ψ and high mass e^-e^+ in ultra-peripheral Au+Au collisions at $\sqrt{s_{\rm NN}} = 200$ GeV. . . . 43
  - 3.2.1 Selection criteria and results . . . 43
- 3.3 Coherent J/ψ photoproduction in ultra-peripheral Pb–Pb collisions at $\sqrt{s_{\rm NN}} =$ 2.76 TeV . . . 43
  - 3.3.1 Analysis and the results . . . 44
- 3.4 Charmonium and e^+e^- pair photoproduction at mid-rapidity in ultra-peripheral Pb–Pb collisions at $\sqrt{s_{\rm NN}} = 2.76$ TeV . . . 45
  - 3.4.1 Event selection and results . . . 45
- 3.5 Coherent ψ(2S) photo-production in ultra-peripheral Pb–Pb collisions at $\sqrt{s_{\rm NN}} = 2.76$ TeV . . . 46

3.5.1 Analysis and results . . . 48
3.6 Coherent J/ψ photoproduction in ultra-peripheral PbPb collisions at $\sqrt{s_{\rm NN}}$ = 2.76 TeV with the CMS experiment . . . 49
3.6.1 Results . . . 49

4 Experimental setup **51**
4.1 The Large Hadron Collider . . . 51
4.2 A Large Ion Collider Experiment (ALICE) . . . 51
4.2.1 Inner Tracking System (ITS) . . . 52
4.2.2 Time Projection Chamber (TPC) . . . 54
4.2.3 Time Of Flight (TOF) . . . 55
4.2.4 The forward rapidity detectors: V0, ZDC and AD . . . 56
4.3 The ALICE trigger system . . . 57
4.3.1 Online control system of ALICE . . . 57
4.3.2 Offline Framework - Aliroot . . . 58

5 Analysis results **59**
5.1 Processing of the data until analysis . . . 59
5.2 Analysis of the coherent and incoherent photoproduction of J/ψ vector mesons . . . 60
5.3 Global event selection . . . 60
5.4 AD and V0 vetoes . . . 61
5.5 Selection of tracks . . . 63
5.6 The extraction of the J/ψ signal . . . 66
5.7 Calculation of the cross section . . . 66
5.7.1 Coherent and incoherent yield $\mathbf{N}^{\rm coh/inc}_{\rm J/\psi}$ . . . 66
5.7.2 Acceptance and efficiency $(A \times \epsilon)_{\rm J/\psi}$ . . . 72
5.7.3 Study of $\Delta\varphi$ distribution . . . 72
5.7.4 Luminosity . . . 76
5.7.5 The ratio of the cross sections of J/ψ . . . 76
5.7.6 Systematic error . . . 76

6 Summary and Discusion **79**

List of Figures

1.1 The schematic view of the single photon exchange (2) where is depicted the lepton current (1) and the hadron current (3). 20
1.2 The ratio of the structure functions showing the parton spin to be $\frac{1}{2}$. Taken from [1]. 21
1.3 a) The short wavelength probe "seeing" a quark. b) The long wavelength probe "seeing" the subprocesses of the QCD. 23
1.4 The violation of the scaling behavior. The data from ZEUS are shown at different values of x and Q^2. Taken from [11]. 24
1.5 Parton distribution function with decreasing x at experiment HERA. For small-x there are dominant slow partons, the sea quarks xS and gluons xg while in small x are dominant valence quarks in proton xu_v and xd_v. Note the logarithmic scale. Taken from [10]. 25
1.6 The behavior of the ratio $R^A_{F_2}(x, Q^2)$ as a function of x at fixed scale Q^2. Taken from [12]. 25
1.7 The diagrams, which relates the diffraction with two scattering contributions to the total cross section. Taken from [12]. 26

2.1 Schematic draw of an ultra-peripheral collision - the interaction of the cloud of virtual photons of ions of lead at impact parameter b greater than the sum of their radii. 29
2.2 Schematic draw of the central barrel and of the coordinate system in high-energy physics. 30
2.3 Schematic draw of a central a) and a peripheral b) collision. 31
2.4 Schematic draw of the coherent photoproduction of a vector meson. 34
2.5 An event of the coherent photoproduction of a VM in this case the ψ(2S) decaying into a J/ψ and a π^+ π^-, with the J/ψ decaying into a muon pair, from a Pb–Pb collision in ALICE at $\sqrt{s_{NN}}$ = 2.76 TeV from Run1. The red lines correspond to the $\mu^\pm$ and the yellow lines to the $\pi^\pm$. Taken from ALICE repository. 35
2.6 The ratio of the e^-e^+ annihilation. Taken from [27]. 36

3.1 Nuclear gluon modification $R^A_g(x, Q^2)$ in particular for Pb ion $R^{Pb}_g(x, Q^2 = M^2_{J/\psi})$ as a function of x with different prediction depicted. Taken from [29]. 39
3.2 Rapidity distributionss of exclusive photoproduction of J/ψ in PbPb collisions at the LHC compared to different model predictions, see text. Taken from [29]. 39
3.3 The ratio R_{coh} of the nuclear cross section for vector mesons J/ψ and Υ to the impulse approximation as a function of W. Taken from [32]. 41
3.4 The model prediction with data from ALICE. Taken from [32]. 42
3.5 The Feynmann diagrams for exclusive photoproduction of J/ψ a) and di-electrons b) in UPC Au+Au collision at PHENIX. Taken from [36]. 43

3.6 The cross section of J/$\psi + Xn$ at mid-rapidity at $\sqrt{s_{\rm NN}} = 200$ GeV compared to the theoretical predictions of STARligt, Strikman, Goncalves-Machado and Kopeliovich. Coherent and incoherent theoretical calculations are shown separately in a) and summed up in b). Taken from [36]. 44
3.7 The cross section of J/ψ at forward rapidity at $\sqrt{s_{\rm NN}} = 2.76$ TeV compared to the theoretical predictions. Taken from [37]. 45
3.8 Coherent cross section a) compared to different models and incoherent cross section b). Taken from [37]. 47
3.9 Measured differential cross section of ψ(2S) photoproduction in UPC Pb–Pb collisions at $\sqrt{s_{\rm NN}} = 2.76$ TeV at mid-rapidity at ALICE. Taken from [39]. 48
3.10 Measured differential cross section of J/ψ photoproduction in UPC Pb–Pb collisions at $\sqrt{s_{\rm NN}} = 2.76$ TeV at CMS compared to ALICE data and different model predictions. Taken from [40]. 49

4.1 The schematic view of cross section of the LHC and its intersection point. ALICE is situated in Point 2. Taken from [44]. 52
4.2 The schematic view of the ALICE during Run2 data taking. The red solenoid magnet L3 surrounds the central barrel. The blue magnet is dipole magnet in part where forward muon spectrometer is located. Taken from [45]. 53
4.3 Up: The schematic view of the ITS upgrade for Run2 data taking. Down: the cross section along the beam line of the Silicon Drift Detector (SDD) [45, 46]. 54
4.4 Schematic view of the MWPC and TPC during Run2 data taking [46, 47]. . 55
4.5 The scheme of DAQ. Taken from [46]. 58

5.1 Correlations of the offline trigger decisions in the CCUP8 triggered events; ADA vs ADC (top) and V0A vs V0C (bottom). 62
5.2 The scheme of time slewing in V0 and AD detectors with charge Q as a function of time t. With a given threshold the high multiplicity events, depicted with red line, trigger an earlier signal at t_1, while the low multiplicity events, shown with a green line, trigger a signal at $t_2 > t_1$ with the same threshold. 63
5.3 Energy loss dE/dx of electrons (top) and of muons (bottom) both after the PID cut. 64
5.4 $p_{\rm T}$ distribution of lepton pairs of muons (top) and electrons (bottom) from Monte Carlo reconstructed tracks. The red line represents the transverse momentum of incoherent photoproduction of J/ψ, while the blue line the coherent one. The green line is the cut to distinguish the coherent photoproduction of the incoherent. Distributions are normalized to unity. 65
5.5 Invariant mass distributions of the J/ψ candidates in the coherent sample (left) and MC (right). The fitting function and results of the fit are shown. 66
5.6 Invariant mass distributions of the J/ψ candidates in the incoherent sample (left) and MC (right). The fitting function and results of the fit are shown. 67
5.7 Invariant mass distributions of the J/ψ candidates in the coherent sample (left) and MC (right). The fitting function and results of the fit are shown. 67
5.8 Invariant mass distributions of the J/ψ candidates in the incoherent sample (left) and MC (right). The fitting function and results of the fit are shown. 68

5.9 The feed down efficiency of coherent (left) and incoherent (right) $\psi(2S) \rightarrow J/\psi + \pi^-\pi^+$, where $J/\psi \rightarrow \mu^-\mu^+$. 71
5.10 The feed down efficiency of coherent (left) and incoherent (right) $\psi(2S) \rightarrow J/\psi + \pi^-\pi^+$, where $J/\psi \rightarrow e^-e^+$. 71
5.11 On this figure is depicted the acceptance and efficiency ($A \times \epsilon$) of coherent (top) and incoherent (left) $J/\psi \rightarrow \mu^-\mu^+$. 73
5.12 On this figure is depicted the acceptance and efficiency ($A \times \epsilon$) of coherent (top) and incoherent (left) $J/\psi \rightarrow e^-e^+$. 74
5.13 Two $\Delta\varphi$ distributions of tracks coming from coherently (blue line) and incoherently (green line) produced J/ψ in muon channel. 75
5.14 Two $\Delta\varphi$ distributions of tracks coming from coherently (blue line) and incoherently (green line) produced J/ψ in electron channel. 75
5.15 The integrated luminosity run-by-run. 76
5.16 Calculated ratios of cross section with Pb–Pb collisions from 2015 data taking at ALICE for the decay channel $J/\psi \rightarrow e^-e^+$ (left) and for the $J/\psi \rightarrow \mu^-\mu^+$ (right) with systematic error depicted as a box and statistical error bar. 78
5.17 Calculated weighted ratios of cross section of J/ψ vector meson with Pb–Pb collisions from 2015 data taking at ALICE. The results are compared to the red point, i.e. the ratio of weighted cross section of J/ψ measured in 2011 Pb–Pb data taking at ALICE [38]. 78

List of Tables

2.1 The properties of J/ψ with branching ratios. Taken from [28]. 36

3.1 Summary of the correction to feed down f_D, coherent f_C and incoherent f_I contribution of the yield. Taken from [38]. 46

5.1 Table of good runs. 61
5.2 The different offline decisions of AD and V0 detectors in different classes. . 61
5.3 Event statistics at various stages of the data selection. 64
5.4 The calculated values of corrections on coherent and incoherent fractions f_I and f_C. 70
5.5 Total cross sections calculated by STARLIGHT. 70
5.6 Total branching ratios for different decay channels of J/ψ and ψ(2S). Taken from [28]. 70
5.7 The summarized values of calculated corrections for feed down, where $f_D = f_D^{\text{charged}} + f_D^{\text{neutral}}$. 71
5.8 The corrected number of J/ψ for both lepton channels in coherent and incoherent photoproduction. 72
5.9 The table with integrated values of $\Delta\varphi \in (150°, 180°)$ distributions of two tracks coming from coherently and incoherently produced J/ψ. 73
5.10 Summary of values for the calculation of the ratio of differential cross section as a function of rapidity y for J/ψ vector meson at 2015 Pb–Pb collisions data taking with ALICE. 77
5.11 Table of systematic error of signal extraction for each decay channel. 77

Preface

One of the most interesting recent topics in perturbative Quantum Chromodynamics in recent years is the internal structure of nucleons and nuclei in terms of quarks and gluons. A useful tool for these studies are the so-called ultra-peripheral collisions (UPC) at the LHC. Here, ultra-relativistic protons or heavy ions interact through the electromagnetic fields, which means that we are able to study photon-hadron interactions. Besides providing this type of interactions the large energy available at the LHC means that we can reach Bjørken-$x \sim 10^{-4} - 10^{-5}$. Interest in this small-x physics is due to its sensitivity to the gluonic structure functions of nucleons through the measurement of the cross section of the process called photoproduction of vector mesons, very useful tool to study QCD phenomena. This work focuses on such process, in particular coherent and incoherent photoproduction of the J/ψ vector meson analyzed from Pb–Pb collisions data collected in Run2 at a center-of-mass energy $\sqrt{s_{\mathrm{NN}}} = 5.02$ TeV with the J/ψ produced at mid-rapidity. This work should put more constraints to some of the model predictions for the nuclear phenomenon of shadowing.

This thesis briefly introduces deeply inelastic scattering, continues with small-x physics and presents the QCD nuclear phenomena shadowing, all in Chapter 1. Next, Chapter 2 firstly focuses on a preview of basic definitions used in experimental physics and then it concentrates into characteristics of UPC ending with a section dedicated to the vector meson J/ψ.

In Chapter 3 are introduced model predictions used to explain either the origin of shadowing or its evolution into small-x. Measured cross sections are compared with these models. The second part of this chapter is dedicated to a review of charmonium measurements in UPC.

The ALICE detector layout is presented in Chapter 4 with a brief explanation of the ALICE trigger system. The analysis of coherent and incoherent vector meson photoproduction is described in Chapter 5, which is followed by a discussion and a summary of the results.

Chapter 1

Introduction

1.1 Deeply inelastic scattering

One of the most important experiments in the 60's of the last century was a study of the parton distribution in nucleons in deeply inelastic experiments (DIS) [1]. Probing the structure of the nucleons by an interaction with charged or neutral leptons, the DIS experiments provided the first dynamical evidence of the existence of quarks and thus supported the idea of the parton model by Richard Feynman that nucleons are formed by smaller constituents: partons [2].

DIS is a process where, as already mentioned, a charged or neutral lepton with high energy scatters off a nucleon, which is accompanied with the breaking of this nucleon and consequently creating some new state X as seen in Fig. 1.1.

The two main observables in deeply inelastic scattering are the energy lost by the lepton, ν, which is given by the simple difference between the energy at the beginning E_i and in the final state E_f, Eq. (1.1)

$$\nu = E_i - E_f \tag{1.1}$$

and the momentum transferred, which is the momentum of the virtual photon, q^2, related to the E_i, E_f and the angle θ through which the lepton is scattered off the nucleon by Eq. (1.2)

$$q^2 = 2E_iE_f(1 - cos\theta). \tag{1.2}$$

The main measurement is then the variation of the cross section with the energy loss of lepton and the angle through which this lepton is scattered.

To describe mathematically the single-photon exchange mechanism, three parts - factors of this process must be considered. The so called lepton current, see Fig. 1.1 1, i.e. the process describing the progress of the lepton through the interaction. It is well known from QED together with the factor including the propagation of the virtual photon, Fig. 1.1 2. The flow of the nucleon in the reaction including its disintegration is called the hadron current, Fig. 1.1 3, and it is a complicated unknown. It can be characterized by a structure functions which are to be determined from the DIS experiments. Writing down all possible combinations of the momenta in the interaction and applying some theoretical principles to simplify the formula, we can obtain the form of the structure functions dependent on the observables ν and q^2 - $F_1(q^2, \nu)$ and $F_2(q^2, \nu)$. The separate behavior of the two structure functions can be determined from experiments observing the lepton scattering angle in the reaction [1].

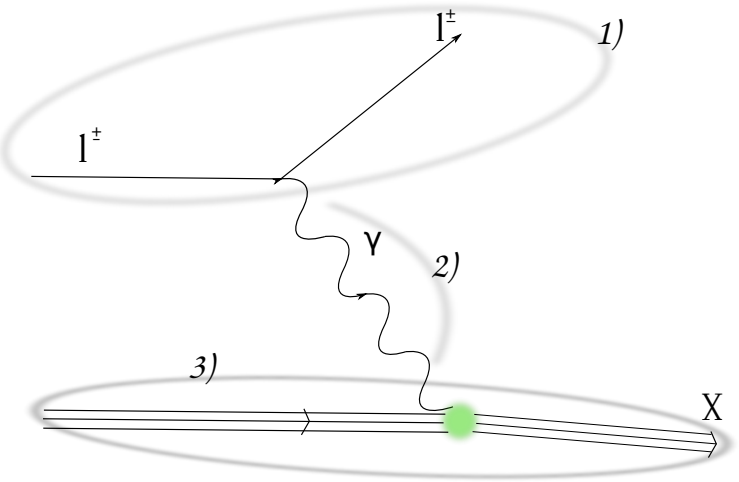

Figure 1.1: The schematic view of the single photon exchange (2) where is depicted the lepton current (1) and the hadron current (3).

1.1.1 Bjørken scaling

The structure functions are dimensionless quantities describing the shape of the nucleon target, they do not have a physical dimension, however they have a dependence on the dimensional quantities, ν the energy loss, and q^2, the transfered momentum. Since the cross section is usually in the units of area given by the Rutherford elastic scattering multiplied by a form factor, i.e. cross sections = unit of area $\times$ pure number, any dependence of the structure functions on the dimensional magnitudes must cancel [1]. This can be obtained by scaling the reaction to the nucleon mass and then the cross section is as following:

$$\frac{d\sigma}{dq^2} = \frac{4\pi\alpha^2}{q^4} F\Big(\frac{q^2}{M_N^2}\Big). \tag{1.3}$$

This is relevant in a range of low-energy elastic scattering. However when we move to the region where the observables q^2 and ν tend to the infinity, this approach is no more valid.

Probing the nucleon structure is like using a microscope with very good resolution. The resolution depends on the wavelength of the light scattered from the object which is observed. The smaller the object is, the shorter wavelength is necessary to view the object. The DIS experiment is an analogue to the microscope. The momentum of the probing particle is related to its wavelength as $p\lambda = h$. Thus to see any structure of the nucleon, we must go beneath the $\approx 10^{-15}$ m, which is the diameter of the nucleon [3]. Then from the formula is clear that the momentum must be greater then 1 GeV/c. Thus, at very high energy when the transferred momentum q^2 and $\nu \to \infty$, the photon will have a very short wavelength and will be able to resolve the internal structure of the nucleon. In this case the scaling factor of the interaction - the mass of the nucleon does not make a sense, in fact any other scaling with a mass wouldn't be useful to determine the scale of the deeply inelastic scattering regime. This was used by James Bjørken to establish his scaling hypothesis [4]. If there is no mass to cancel out the dimensionality of the structure functions which consists in the dependence on the ν and q^2, then they must be dependent on the ratio of these two dimensional magnitudes as following, Eq. (1.4):

$$x = \frac{q^2}{2M_N\nu}, \tag{1.4}$$

thus we can write $F_{1,2}^{eN}(q^2, \nu)$ as a function of Bjørken-x $F_{1,2}^{eN}(x)$. The scaling has an important physical interpretation. The choice of x reflects the fraction of the momentum of the nucleon carried by the parton struck by the photon. It effectively measure the momentum distribution amongst the constituent partons.

The scaling hypothesis was a very important step in understanding the structure of the nucleon as formed from point-like constituents [5]. Early experiments at medium values of x and in a limited range of q^2 confirmed the scaling and showed that the structure function depends only on x and not on q^2 separately.

1.1.2 The fruits of the scaling

The results from deeply inelastic scattering experiments reveal a lot about the quarks [1]. Writing down the formula for electron-proton scattering and comparing it with the QED formula for electromagnetic interactions of electrons with other electrically charged particle of spin $\frac{1}{2}$, it is possible to derive the relationship between the structure functions, Eq. (1.5):

$$2xF_1(x) = F_2(x), \tag{1.5}$$

which is the famous Callan-Gross relation [6]. Experimentally, the ratio $2xF_1/F_2$ is found to be one, which can be interpreted as an evidence for the partons having spin $\frac{1}{2}$, see Fig. 1.2.

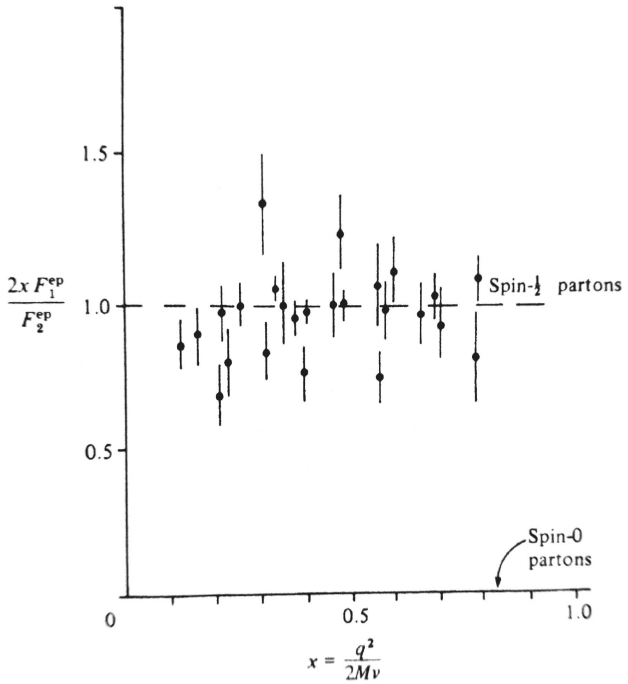

Figure 1.2: The ratio of the structure functions showing the parton spin to be $\frac{1}{2}$. Taken from [1].

Another interesting thing is the measurement of the fractional momentum carried by the quarks. The total share of the momentum in the proton carried by the up quarks is double than that of the down quarks, $P_u = 0.36$ and $P_d = 0.18$. This again support the

picture of the quark model. Not only this information can be read from the experiment. It is clear that only one-half of the total momentum is carried by quarks. The other half is caused by the interquark forces, which are interpreted as quanta of the strong nuclear force: gluons. Since they are electrically neutral, they show up only as a missing momentum in the proton.

If we go back to the situation where the highly energetic photon probes the structure of the nucleon, it sees with its short wavelength the constituent partons like if they were free. In this case, the probe interaction with one constituent parton is completed before the interparton forces would have a chance to relay the event to the rest of the nucleon. This situation is strange because one parton was hit so hard that it flies off with high momentum, while the rest of the nucleon remains for a short time in the same state like if there wasn't any interaction. But this situation cannot last long, the struck parton will fly off the nucleon and we would expect to see a free quark. However this was never observed in Nature, instead a new quark-antiquark pair is pulled from the vacuum forming new hadrons. This behavior is quite opposite to the known electromagnetic force. If the wavelength of the photon is roughly 10^{-17} m, i.e. the distances probed are $\approx 10^{-17}$ m, the quarks can be observed as free particles because the strong force which connects them together is very weak. However when the distance between two constituent quarks increases to the size of the nucleon, i.e. 10^{-15} m, and more, the strong force grows causing the confinement of the quarks within the observed hadrons. The former phenomenon is called *asymptotic freedom* [7, 8], while the latter is called *confinement*.

1.1.3 Small-x physics

Before the Large Hadron Collider (LHC) era, the H1 and ZEUS experiments at HERA in Hamburg obtained nice results of a complex partonic structure of the proton [9]. The data were available in wider ranges of x and q^2 and revealed that the constancy of the scaling is no more valid. On Fig. 1.4 is depicted the structure function F_2 as a function of $Q^2 = -q^2$ for different values of x for four orders of magnitude in both x and Q^2. As can be seen here, the scaling is indeed valid at higher values of x, but with decreasing x becomes obvious the dependence on Q^2, the structure function rises with rising Q^2. The interpretation of the violation of the scaling behavior is the following: the probability of hitting the parton carrying the higher momentum of the nucleon by a probe is smaller while the probability to hit a parton carrying a small fraction of the momentum of the nucleon rises instead. In the sections above was mentioned the analogy of DIS with a microscope. Using this approach can be explained better the interpretation of the data. The probe with some momentum is like a microscope with some resolution. For this reason the $Q^2 = -q^2$ is, besides the virtuality, also called the resolution. The long-wavelength probe observes quarks inside the nucleon, thus the resolution is not so good, however the shorter-wavelength probe with a better resolution observes a quark accompanied with the gluon instead. The momentum carried by a quark seen by a long-wavelength probe has to be now divided into quark and a gluon accompanying it, see Fig. 1.3. Thus the greater the momentum is, the more subprocesses of QCD are revealed to a probe, such as gluons radiated by valence quarks, implying a decrease of the fraction of the momentum carried by the observed parton.

In Fig. 1.5 is demonstrated what was said above but with data. The F_2 structure functions and corresponding distribution of quarks and gluons are extracted from HERA data using perturbative QCD for the fixed virtuality Q^2, with decreasing x [10]. For the values $10^{-1} < x < 1$ are dominant the valence quarks of proton. The distribution is smeared because of the continuos exchange of the gluons between quarks. As the x is

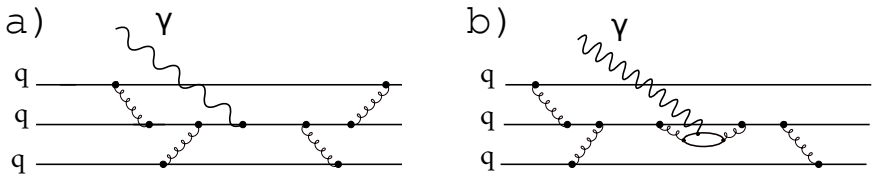

Figure 1.3: a) The short wavelength probe "seeing" a quark. b) The long wavelength probe "seeing" the subprocesses of the QCD.

decreasing there is clearly seen the raising dominance of the sea quarks and gluons inside the proton (note the logarithmic scale and also the factor by which are multiplied the gluon distributions).

From the ideas quoted above we can assume that with $q^2 \to \infty$ there would appear new and new partons. This obviously wouldn't last long since the nucleon has limited space and thus these new formed partons begin to recombine. This is called *saturation*.

1.1.4 Shadowing

One can suppose that summing all the structure functions of all nucleons in the nucleus one can obtain the structure function of this nucleus. It can be quantified as the nuclear ratio for structure function F_2 as in Eq. (1.6):

$$R_{F_2}^A(x, Q^2) = \frac{F_2^A(x, Q^2)}{AF_2^{nucleon}(x, Q^2)}, \tag{1.6}$$

where x and Q^2 are Bjørken-x and virtuality of the incoming photon, respectively, A is the number of nucleons in the nucleus and $F_2^{nucleon} = F_2^{deuterium}/2$ where nuclear effects are assumed to be negligible [12].

The behavior of this ratio is schematically shown in Fig. 1.6. If the assumption from above would be correct, the $R_{F_2}^A(x, Q^2)$ would be one, however there is clearly seen the deviation from this value and it could be divided in four regions going from the larger x to the smaller value of x: the Fermi motion, the EMC region, the antishadowing region and the shadowing region where Bjørken-$x < 0.1$.

Thus in small-x physics shadowing phenomenon will be dominant and we can assume that the smaller the value of x, the greater is the shadowing.

The origin of this behavior is mostly explained by a multiple scattering, i.e. the hadronic component of the virtual photon wave function interacts several times with different nucleons in the nucleus. The consequence of the multiple scattering is the reduction of the cross section σ_{γ^*-A} of this process related to F_2 as:

$$F_2^A(x, Q^2) = \frac{Q^2(1-x)}{4\pi^2\alpha_{EM}}\sigma_{\gamma^*-A}, \tag{1.7}$$

where α_{EM} is the fine structure constant.

There are different models which try to explain the origin of the shadowing. They have the same basis, i.e. the multiple scattering, but different approaches.

Glauber-Gribov formalism

The models based on Glauber-Gribov formalism are in coherent limit, which means that the hadronic fluctuation of the virtual photon interacts with the whole target [12]. In the laboratory frame the lifetime of the hadronic fluctuation, to be able to interact with the

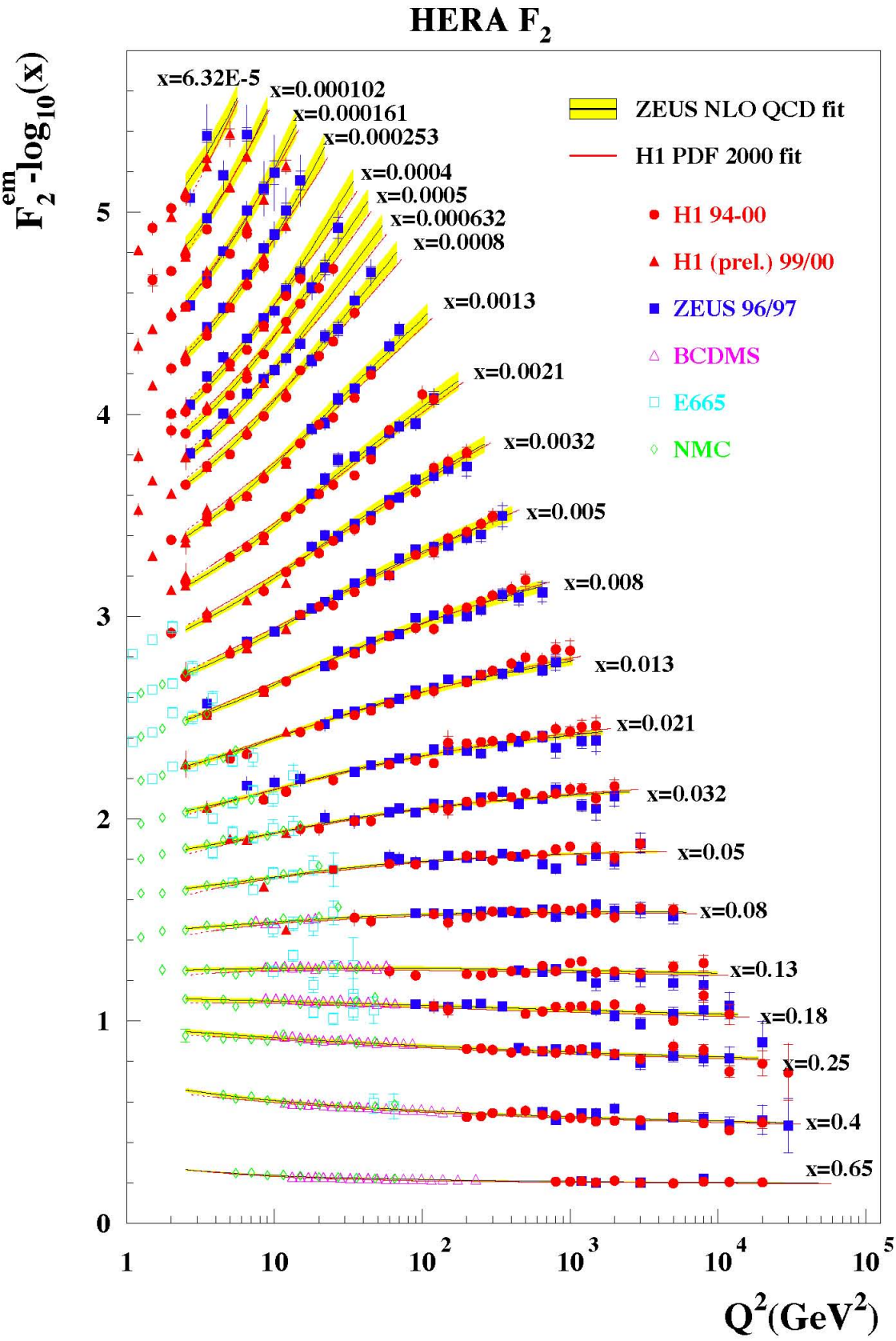

Figure 1.4: The violation of the scaling behavior. The data from ZEUS are shown at different values of x and Q^2. Taken from [11].

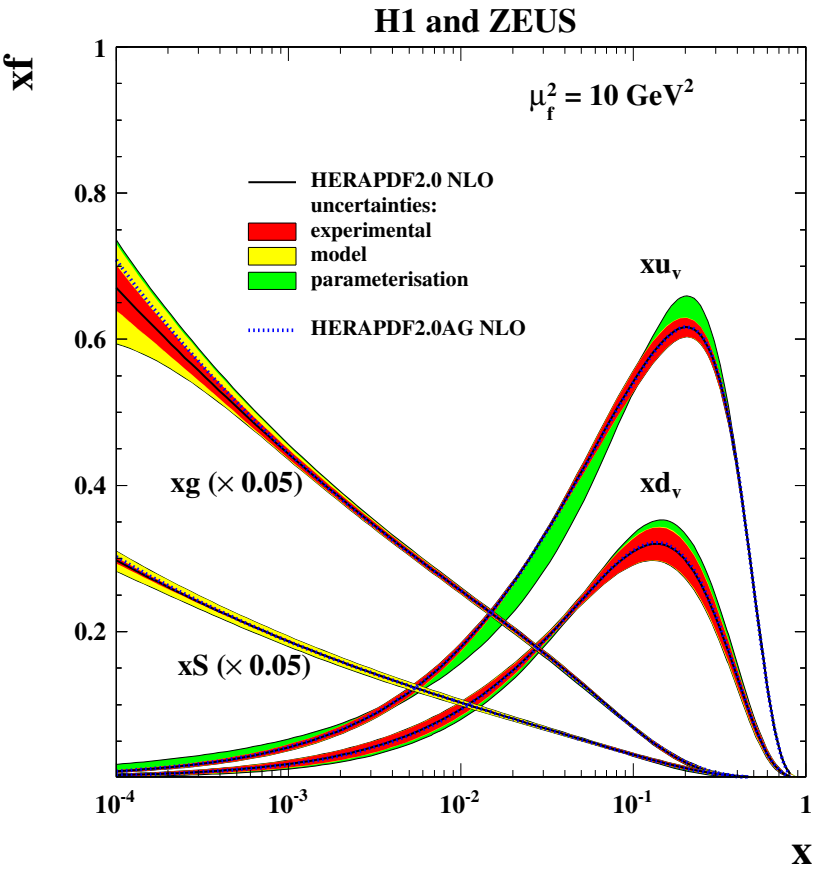

Figure 1.5: Parton distribution function with decreasing x at experiment HERA. For small-x there are dominant slow partons, the sea quarks xS and gluons xg while in small x are dominant valence quarks in proton xu_v and xd_v. Note the logarithmic scale. Taken from [10].

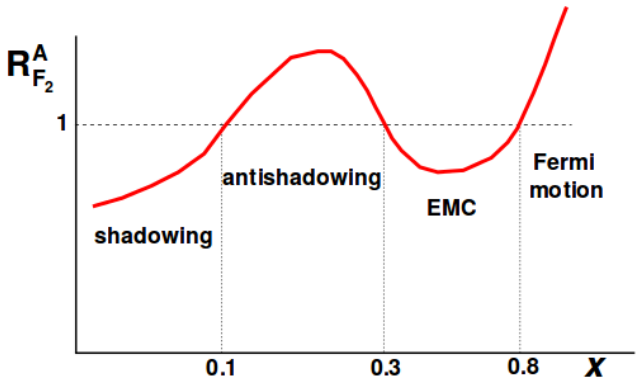

Figure 1.6: The behavior of the ratio $R_{F_2}^A(x, Q^2)$ as a function of x at fixed scale Q^2. Taken from [12].

target as a whole, has to be $\tau > R_A$, i.e. greater than the nuclear radius. Since the lifetime of this fluctuation is related to the nucleon mass and x through the relation in Eq. (1.8)

$$\tau \sim \frac{1}{2m_{nucleon}x}, \tag{1.8}$$

the mass spectrum of the intermediate fluctuation must be considered in Glauber-Gribov formalism. In this formalism the nucleus is considered as composed of nucleons with neglected binding energy. The hadronic fluctuation of the virtual photon maintains fixed size during the multiple scattering with such nucleus (the so called eikonal approximation) and usually is limited to the lowest Fock state order, the $q\bar{q}$ pair, i.e. the dipole model.

The total dipole-nucleus cross section is in Eq. (1.9)

$$\sigma_{dipole-A}(x,r) = \int d^2b\ 2\Big[1 - \exp\Big(-\frac{1}{2}AT_A(b)\sigma_{dipole-nucleon}(x,r)\Big)\Big], \tag{1.9}$$

where T_A is the nuclear profile, b is the impact parameter, which will be introduced in Chapter 2 and r is the size of the dipole [12]. Through Eq. (1.7) and with Eq. (1.10)

$$\sigma_{\gamma^*-A}(x,Q^2) = \int d^2r\rho(r,Q^2)\sigma_{dipole-A}(x,r), \tag{1.10}$$

the dipole-nucleus cross section can be related to the nuclear structure function F_2. The $\rho(r,Q^2)$ is the distribution of color dipoles with size r, which were created by the fluctuation of the incident photon into a $q\bar{q}$ pair.

Gribov inelastic shadowing

The relativistic Gribov model is a contrary to the classical Glauber model where the interactions between nucleons from the target colliding with those from the projectile occur subsequently without changing the intermediate states of the nuclei, they are same as they were at the beginning [12].

The Gribov theory suppresses the subsequent interaction at high energy and instead the collision proceeds through simultaneous interactions of the projectile with the nucleons in the nucleus. Here the intermediate states are no more the same as it is in Glauber model, but differ from the initial conditions, i.e. inelastic scattering.

When the Reggeon calculus and Abramovsky-Gribov-Kancheli (AGK) cutting rules are used, it allows to relate the cross section for diffractive dissociation of the projectile to two-scattering contribution to the projectile-target cross section, see Fig. 1.7. Applying some assumptions about diffractive DIS it can be shown, that it is directly related to the first contribution to the nuclear shadowing. For more detailed discussion see [12].

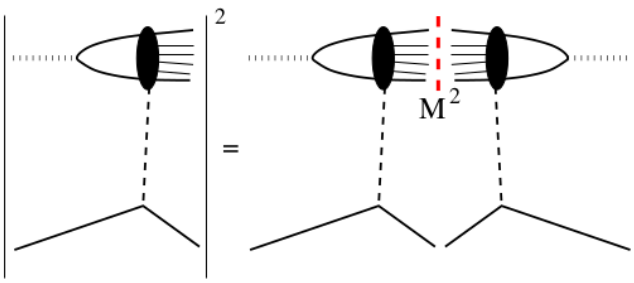

Figure 1.7: The diagrams, which relates the diffraction with two scattering contributions to the total cross section. Taken from [12].

McLerran-Venugopalan (MV) and Balitsky-Kovchegov (BK) equations

In the region of small-x the slow gluons, i.e. partons with small x in high-density QCD have high occupation number $\propto 1/\alpha_s$, where α_s is the running coupling [12]. The unintegrated gluon density N_g^A, i.e. the gluon density at fixed impact parameter, given per transverse momentum of the gluon, for an ultra-relativistic large nucleus is proposed by the McLerran-Venugopalan (MV) model in Eq. (1.11)

$$\frac{dN_g^A}{dyd^2bdk_T} \equiv \frac{d(xg_A)}{d^2bd^2k_T} \propto \frac{1}{\alpha_s}\int \frac{d^2x_T}{x_T^2} e^{-ix_Tk_T}\Big(1 - e^{-x_T^2Q_s^2/4}\Big), \tag{1.11}$$

where k_T is the transverse momentum of the lepton and $Q_s^2 \propto AT_A(b)xg_{nucleon}$ is the saturation scale or the squared saturation momentum. It is proportional to the gluon transverse momentum and grows up as the nuclear size increases or increases the energy, i.e. decreases x. With increasing energy, the number of partons is not modified, they are just redistributed in transverse momentum x_T, it is an analog to Glauber-like rescattering in the coherent, high-energy limit.

However, with increasing energy, additional gluons are radiated from the so-called source, i.e. "fast" valence quarks, and consequently absorbed by this source. The equation which describes the distribution of the color sources in the hadron, i.e. the dipole-hadron scattering amplitude is a non-linear Balitsky-Kovchegov (BK) equation [13, 14, 15, 16, 17, 18], where the use of the dipole model links it with the structure functions. The BK evolution equation in contrary to the MV model diminish the number of gluons.

The MV model can be used as an initial condition for the BK evolution from $x \sim 0.01$ towards smaller x. Now, the virtual photon-nucleon cross section in a dipole model is no more dependent on x and Q^2 but become a function of Q^2/Q_s^2, where all dependencies on x and nuclear size are included in Q_s^2 scale. For further details, consult with [12].

Dokshitzer-Gribov-Lipatov-Altarelli-Parisi (DGLAP) evolution

Other models instead of studying the origin of shadowing focus on the Q^2-evolution of nuclear ratios of parton densities through the evolution equations such as DGLAP [19, 20, 21].

The DGLAP is an integro-differential equation, which provides a tool to find analytically the parton distribution functions (PDF) at some values of x and Q^2 if there are given initial conditions at some Q_0^2. As was mentioned above, the initial state at large energies radiates gluons, i.e. it is accompanied with so-called collinear divergences and this radiation persists. That means that we must to account for these divergences in all orders when doing the perturbative theory. Choosing the right gauge theory, the divergences reduce to leading logarithms which can be summed up and included into the parton distribution functions. In the resummation, the PDFs become scale dependent and leads to the DGLAP evolution equation. The models above can be used as an initial condition for DGLAP evolution equation.

Thus the DGLAP relates the logarithmic Q^2-evolution of the structure functions to the gluon distribution and it has been extended to the nuclear ratio valid at LO and small x. These ratios are parametrized at value $Q_0^2 \sim 1-2$ GeV^2 due to availability of the perturbative theory in this region and cover the full range of x as $0 < x < 1$ [12]. Since this is the extention from nucleon to the nuclear case, the size of nuclei appears as an additional variable. These initial conditions are evolved through the DGLAP in $Q^2 > Q_0^2$ region and are compared with the experimental data. After the comparison, the initial parameters are adjusted to correspond with the data.

The gluon distributions, contrary to F_2 structure functions, can be constrained only indirectly in proton-nucleus or nucleus-nucleus collisions at Large Hadron Collider (LHC) in UPC.

Chapter 2

Ultra-peripheral collisions

In 1924, Enrico Fermi came up with an idea to treat the electromagnetic field of a fast charged particle as a flux of virtual photons [22]. He did notice that when a fast charged particle is seen from some distance away from its trajectory, its electric field pointing radially out and magnetic field circling it seems to be like the fields of a real photon. A consequence is the replacement of the electromagnetic field by a photon flux. This method called the equivalent photon method was a decade later applied to ultra-relativistic particles by Weiszäcker and Williams where the fields are Lorentz contracted.

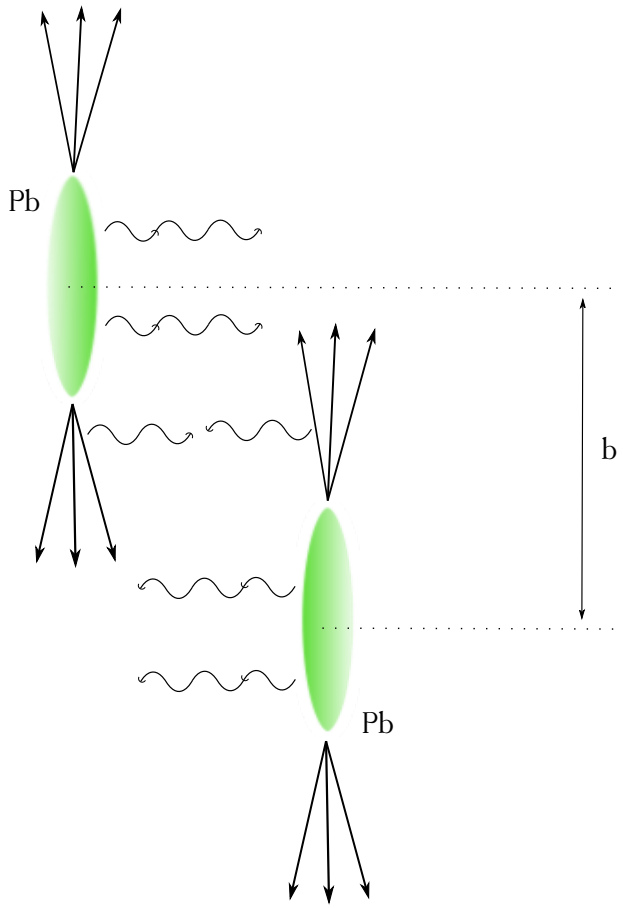

Figure 2.1: Schematic draw of an ultra-peripheral collision - the interaction of the cloud of virtual photons of ions of lead at impact parameter b greater than the sum of their radii.

2.1 Definitions

Before I present general characteristics of ultra-peripheral collisions, let me introduce definitions of the following terms: coordinate system, impact parameter and terms related to it, cross section, luminosity, rapidity and pseudorapidity.

2.1.1 Coordinate system

The coordinate system in high-energy particle physics has x, y and z components, in which center lies the interaction point (IP), see Fig. 2.2. The $z-$axis, the so-called longitudinal direction, is parallel to the beam and perpendicular x and y coordinates form the transverse plane. In this plane is defined the angle φ, which together with angle θ - the deviation from the $z-$axis, forms a polar coordinate system.

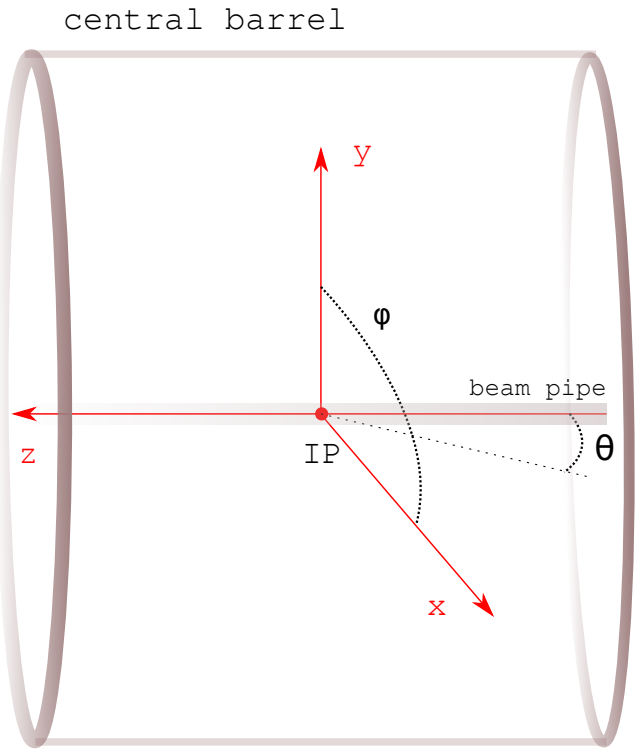

Figure 2.2: Schematic draw of the central barrel and of the coordinate system in high-energy physics.

2.1.2 Impact parameter, centrality, multiplicity

The impact parameter b is depicted in Fig. 2.1 and 2.3. It is a vector, which connects the centers of colliding nuclei in the transverse plane.

Through the impact parameter b can be defined the centrality of the collision. If the case is $b \ll R_A + R_B$, i.e. the two colliding nuclei A and B with radius R_A and R_B overlap in the collision, it is so-called central collision. In case that $b \approx R_A + R_B$ it is peripheral collision and if the two nuclei do not overlap in the collision in way that $b > R_A + R_B$ it is ultra-peripheral collision as seen in Fig. 2.1. For central and peripheral see Fig. 2.3 a) and b), respectively.

The number of particles produced is closely related to the centrality of the collision. The more central collision, the more produced particles will be expected. The number of particles produced in a collision is called multiplicity.

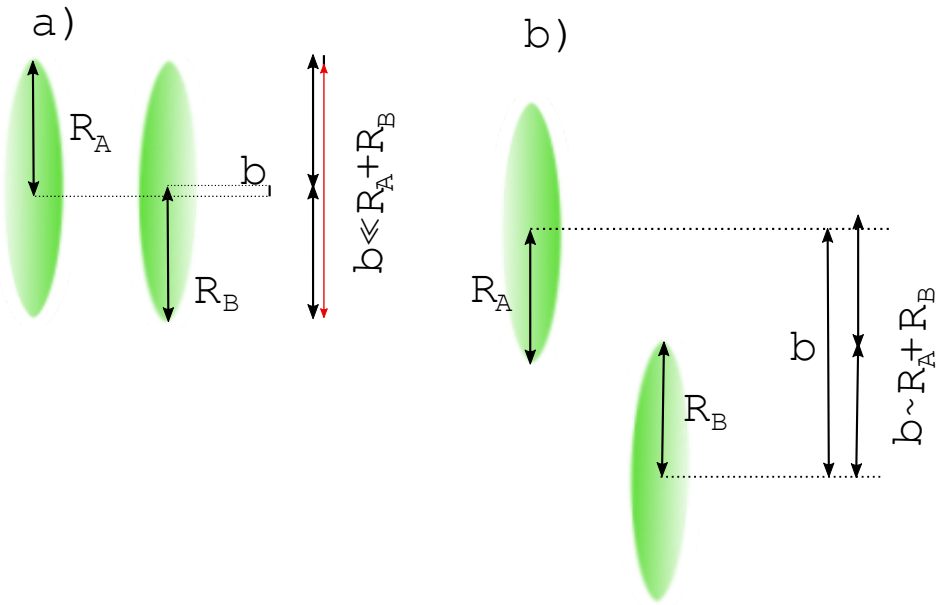

Figure 2.3: Schematic draw of a central a) and a peripheral b) collision.

2.1.3 Cross section

The probability that a certain event occurs in a collision is defined with a quantity called the cross section and it describes the effective area of the collision, thus it is given in units of m^2. In particle physics however this unit isn't practical and the barn $b = 10^{-28}$ m^2 is used instead. The differential cross section $\frac{\mathrm{d}\sigma}{\mathrm{d}\Omega}$ provides information about the production of particles in a solid angle. Total cross section σ_{tot} is then the integral over this solid angle ($\mathrm{d}\Omega = \sin(\theta)\mathrm{d}\theta\mathrm{d}\varphi$) as

$$\sigma_{tot} = \int_0^{2\pi} \int_0^{\pi} \frac{\mathrm{d}\sigma}{\mathrm{d}\Omega} \sin\theta \mathrm{d}\theta \mathrm{d}\phi. \tag{2.1}$$

2.1.4 Luminosity

The number of events N produced in a collision per unit of time t -rate R, is directly proportional to the interaction cross section σ as

$$R = \frac{\mathrm{d}N}{\mathrm{d}t} = \sigma L. \tag{2.2}$$

The units of luminosity are then from Eq. (2.2) cm^{-2}s^{-1} or more useful b^{-1}s^{-1}.

In the case of a circular accelerator, where two beams accelerated separately in two beam pipes, contain bunches carrying some number of particles n, which have a Gaussian profile σ_x and σ_y with a frequency of a collision f, the luminosity is given as following:

$$L = f \frac{n_1 n_2}{4\pi\sigma_x\sigma_y}. \tag{2.3}$$

To obtain information of the amount of recorded data during some period, the luminosity from Eq. (5.15) is integrated over this time period as:

$$\mathscr{L} = \int L \mathrm{d}t. \tag{2.4}$$

2.1.5 Rapidity and pseudorapidity

The rapidity can be understood as the velocity of the particle defined in a following way:

$$y = \frac{1}{2} \ln \frac{E + p_L}{E - p_L}, \tag{2.5}$$

where E is the total energy of the particle and p_L is the longitudinal momentum, i.e. in the direction of the beam line. The rapidity is not a Lorentz-invariant, however it is additive in Lorentz transformations along the z coordinate.

A useful definition is the pseudorapidity since it only depends on the polar angle θ and it can be measured easily in a detector. It is defined as:

$$\eta = \ln \tan \frac{\theta}{2} = \frac{1}{2} \ln \frac{|\vec{p}| + p_L}{|\vec{p}| - p_L}. \tag{2.6}$$

If we go to relativistic energies where the rest mass of the particle can be neglected, we note, that the pseudorapidity η converges to the rapidity definition y, since $|\vec{p}| \sim E$.

2.2 The photon flux and processes of UPC

The interactions where two ions interact via their clouds of virtual photons are called Ultra-Peripheral Collisions (UPC). A Fourier transform of the time-dependent electromagnetic field gives the number of photons in the cloud surrounding the nuclei with energy ω, $n(\omega)$ [22]. The amount of photons is proportional to the atomic number Z^2. Thus collisions provided with heavy ions of lead in LHC are highly favored for these types of interactions.

In the laboratory frame the maximum energy of the photon flux ω^{max} of the relativistic heavy ions is limited by the boost of the source, Eq. (2.7), which is several TeV at the LHC:

$$\omega^{max} = \frac{\hbar}{\Delta t} \sim \frac{\gamma \hbar v}{b}. \tag{2.7}$$

It depends on the projectile velocity v, the interaction time Δt, γ the Lorentz factor and the impact parameter b. These photons are quasi-real with the virtuality dependent on the nuclear radius R_A, $Q^2 = -q^2 \approx (\hbar/R_A)^2$. One possible type of interaction of the target and projectile (Pb–Pb interaction) mediated by a single quasi-real photon is the production of a vector meson (VM). This process is called photoproduction of a vector meson. In case when the interchanged photon is virtual, the process would be called electroproduction of a vector meson.

The flux of virtual photons per unit area $N(\omega, b)$ at large energies such as at Large Hadron Collider (LHC) $\approx 1 - 10$ TeV is in Eq. (2.8):

$$N(\omega, b) = \frac{Z^2 \alpha \omega^2}{\pi^2 \gamma^2 \hbar^2 v^2 \beta^2 c} \Big[K_1^2(x) + \frac{1}{\gamma^2} K_0^2(x) \Big], \tag{2.8}$$

where $n(\omega) = \int N(\omega, b) d^2 b$, x is $x = \omega b / \gamma \beta \hbar$, $\alpha = 1/137$ is the fine constant, βc is the velocity of the particle and finally $K_{0,1}$ are the modified Bessel functions, where K_0 results

from the transversely polarized flux of photons with respect to the ion direction and the K_1 results from longitudinally polarized photon flux with respect to the beam direction. When the energy of the photon ω would be larger than a limit, such as seen in Eq. (2.7) $\omega > \gamma\hbar\beta c/b$, the photon flux will be exponentially suppressed.

The interaction between target and the projectile may occur in different ways. Either the high energy photon radiated from the projectile interacts directly with the target, or this photon 'interacts' directly with other photon emitted from the target. In both cases Pb ions with some final state X are present in final state; Pb–Pb $\rightarrow$ Pb–PbX. The cross section for the first manner of the interaction is as following in Eq. (2.9):

$$\sigma_X = \int d\omega \frac{n(\omega)}{\omega} \sigma_X^{\gamma}(\omega), \tag{2.9}$$

where $\sigma_X^{\gamma}(\omega)$ is the photon–target cross section, ω is the energy of photon and $n(\omega)$ is the number of photons [23].

For the latter process there is a logical change in the cross section Eq. (2.10), where $\sigma_X^{\gamma\gamma}$ for two-photon cross section appears:

$$\sigma_X = \int d\omega_1 d\omega_2 \frac{n(\omega_1)}{\omega_1} \frac{n(\omega_2)}{\omega_2} \sigma_X^{\gamma\gamma}(\omega_1, \omega_2), \tag{2.10}$$

When speaking about the interaction of two photons, we refer to a loop diagram involving a fluctuation, since it's known from quantum electrodynamics (QED) that two photons do not interact with each other. In particular, for this thesis the interesting type of the photoproduction of VM is the interaction of quasi-real photon with the projectile γPb. The virtual photon fluctuates into a color dipole formed by a $q\bar{q}$ pair. Only now the color field interacts with the target through the gluon field producing the vector meson as a free particle, which can be subsequently detected, Fig. 2.4. The perturbative QCD can be applied to this type of interaction, where in leading order (LO) the contribution of two gluons in the color singlet state is present. To calculate this process, the convenient reference frame must be used since the lifetime of the $q\bar{q}$ pair must be long enough to be able to interact with the target.

2.2.1 The experimental observables of a VM

The experimental observables of the vector meson (VM) are the transverse momentum p_{T}, the azimuthal angle, its invariant mass and the rapidity y. The rapidity of the VM is defined as following

$$y = \ln \frac{(p_0 + p_z)}{(p_0 - p_z)}, \tag{2.11}$$

where p_0 and p_z refer to the zero and third component of the four momenta of the VM, respectively. The kinematic description of the process depicted in the Fig. 2.4 is provided by the center-of-mass energy of the photon-target $W_{\gamma\mathrm{Pb}}$ system as

$$(W_{\gamma\mathrm{Pb}})_{\pm}^2 = M\exp(\pm|y|)\sqrt{s}, \tag{2.12}$$

M is the mass of the vector meson and $\sqrt{s}$ is the center-of-mass energy of the Pb-Pb.

The differential cross section for the coherent photoproduction of the VM in a Pb-Pb UPC is [24]

$$\frac{d\sigma_{\mathrm{PbPb}}(y)}{dy} = N_{\gamma/\mathrm{Pb}}(y, M)\sigma_{\gamma/\mathrm{Pb}}(y) + N_{\gamma/\mathrm{Pb}}(-y, M)\sigma_{\gamma/\mathrm{Pb}}(-y), \tag{2.13}$$

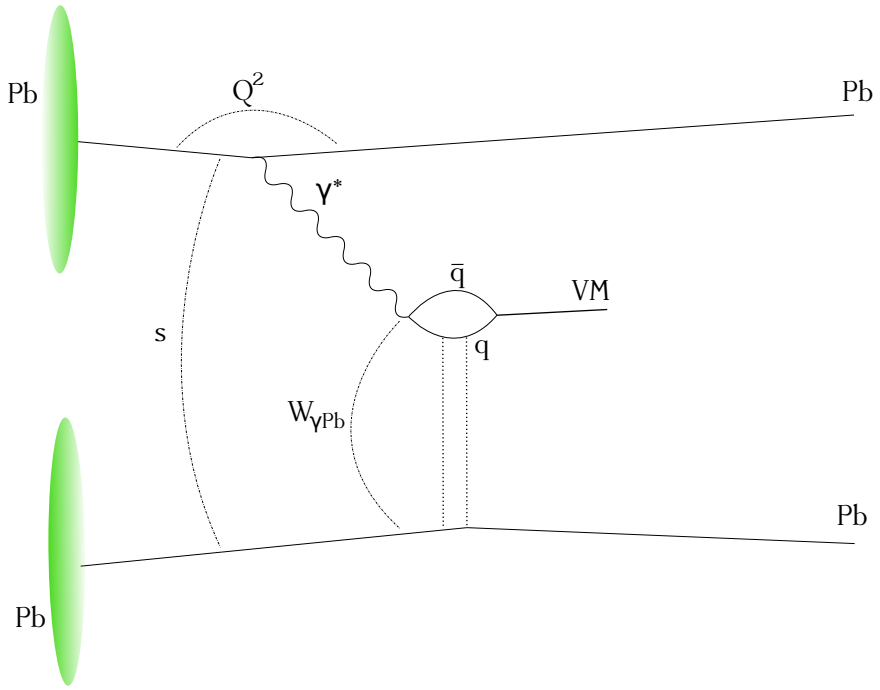

Figure 2.4: Schematic draw of the coherent photoproduction of a vector meson.

where M is the mass of the VM, in our case is the J/ψ, y is the rapidity in the laboratory system

$$y = \ln\left(\frac{2\omega}{M}\right), \tag{2.14}$$

ω is the energy of photon, the $\sigma_{\gamma/Pb}(y)$ is the cross-section of the corresponding photoproduction and $N_{\gamma/Pb}$ is the photon flux. The terms in the sum represent the incoming nuclei - target and projectile - each acting as a source of photon. The probability of emitting the photon at mid-rapidity ($y = 0$) is the same for both target and projectile since they are symmetric, see Eq. (2.13). The fraction per nucleon of the longitudinal momentum of the nuclei participating in the interaction, x, probed by the J/ψ is

$$x = \left(\frac{M_{\mathrm{J}/\psi}}{W_{\gamma\mathrm{Pb}}}\right) = \left(\frac{M_{\mathrm{J}/\psi}}{\sqrt{\mathrm{s}}}\right)\exp(\pm y). \tag{2.15}$$

Thanks to the relation between $W_{\gamma\mathrm{Pb}}$ and x, we can probe the gluon distribution at different x by measuring the cross section of $\gamma\mathrm{Pb} \to \mathrm{PbJ}/\psi$ at various $W_{\gamma\mathrm{Pb}}$.

The formulas in this section are valid for both the coherent and the incoherent production of the vector meson.

2.2.2 Types of exclusive photoproduction

The photoproduction of the vector mesons can be either coherent or incoherent. Coherent denotes the process where the colour dipole interacts with the whole colour field of the target, i.e. the emitted photon has to have the wavelength greater or at least as it is the nuclear radius [22]. Its main characteristic is the small transverse momentum $p_{\mathrm{T}} \approx 60$ MeV/c of the final state. The nucleus normally does not break up, however the additional interchange of the photons may lead to the break-up or disintegration of the nucleus. On the other hand there is incoherent photoproduction which means the colour dipole

couples to a single nucleon. It is characterized by higher transverse momentum of the VM $p_{\mathrm{T}} \approx 500$ MeV/c. In this case the nucleus breaks-up almost every time.

The consequence of the coherent photoproduction is the creation of only one VM, no nuclear fragments or other particles are present, see Fig. 2.5. This interaction is thus called the *exclusive photoproduction*. In case of additional interaction of photons, there might be besides the VM some neutrons detected at very forward rapidities.

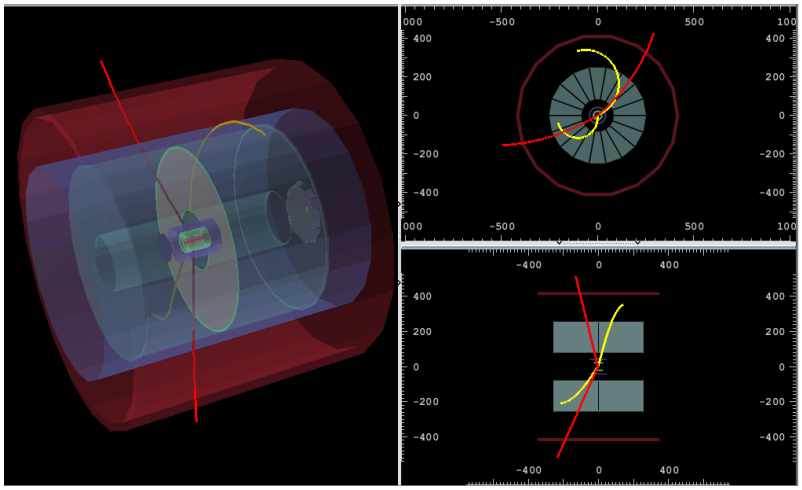

Figure 2.5: An event of the coherent photoproduction of a VM in this case the $\psi(2S)$ decaying into a J/ψ and a π^+ π^-, with the J/ψ decaying into a muon pair, from a Pb–Pb collision in ALICE at $\sqrt{s_{NN}} = 2.76$ TeV from Run1. The red lines correspond to the $\mu^{\pm}$ and the yellow lines to the $\pi^{\pm}$. Taken from ALICE repository.

2.3 The J/ψ vector meson

Since this Master's Thesis concerns the study of the cross section of the coherent and incoherent photoproduction of the vector meson J/ψ, this section will be dedicated to its discovery and characteristics. Recent studies on it will be present in the next Chapter 3.

2.3.1 Discovery

In the issue from November, 1974 of the Physical Review Letters appeared in the same volume two different publications announcing the discovery of the same very narrow resonance with mass $M = 3.1$ GeV [25, 26]. Two different approaches were used to get the same conclusion, the discovery of a charmonium J/ψ. While in the Brookhaven National Laboratory (BNL) in 30 GeV alternating-gradient synchrotron used the reaction of $p + Be \rightarrow e^+ + e^- + X$, where the beam with 10^{10} to 2×10^{12} protons per pulse were guided to the Be target, in the Lawrence Berkley Laboratory in the Stanford Linear Accelerator Center (SLAC) at the electron-positron storage ring a sharp peak was observed in the invariant mass distribution of the e^+e^- pair when measuring the process colliding $e^- + e^+ \rightarrow$ hadrons. While the former method is suitable to looking for new particles due to the large spectrum obtained as a result, the later method is more useful to estimate precise properties of the particle. The leader of the team in BNL was Samuel Ting and he proposed to name this resonance as J. In the other experiment at SLAC, Burton Richter, proposed to call it ψ since the reaction of $e^-e^+ \rightarrow$ J/ψ, where J/$\psi \rightarrow \pi^-\pi^+$ has a shape like ψ.

Both obtained a Nobel prize in 1976 for the discovery of the J/ψ and the confirmation of a new existing quark–charm quark c.

2.3.2 Characteristics of J/ψ

Such a narrow resonance, in times of the discoveries its width was practically 0, i.e. it was less than the resolution of the detector, was never observed before. From the relation between the lifetime of the particle and the width $\tau = \hbar/\Gamma$ is clear that this resonance has an unexpected long lifetime $\approx 10^{-21}$s. With such a long lifetime, resonances normally live $\sim 10^{-23}$ s, and such large mass, the only explanation for the composition of J/ψ was the charm quark c. Indeed, it is a hidden charmonium, i.e. it consists of a quark-antiquark pair $c\bar{c}$ and the charmness–the total charm quantum number is 0. Another remark of the presence of the charm quark is the large cross section, an enhancement roughly 100 times larger than outside the resonance, see Fig. 2.6. On this Figure is depicted the ratio as in Eq. 2.16 as a function of the invariant mass:

$$R = \frac{\sigma(e^-e^+ \to hadrons)}{\sigma(e^-e^+ \to \mu^-\mu^+)} = 3\Big(\sum_f Q_f^2\Big), \tag{2.16}$$

where Q_f^2 is the fractional charge of the quark flavor $f = u, d, s, c, b$ active at the interaction energy. There is clearly seen the increase in ratio as new quarks forms new particles, i.e. J/ψ and its charmonium family, after that Υ with b quarks, etc.

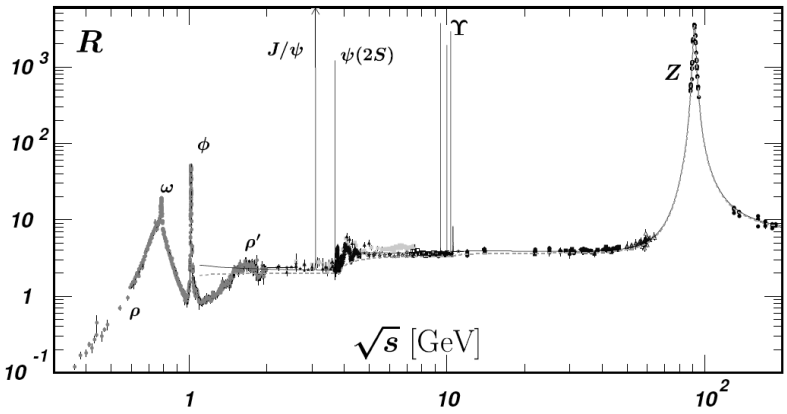

Figure 2.6: The ratio of the e^-e^+ annihilation. Taken from [27].

The list of summed up J/ψ properties can be found in Table 2.1.

Mass	3096.900 ± 0.06 MeV/c^2
Full width	92.9 ± 2.8 keV/c^2
J^{PC}	1^{--}
BR (J/$\psi \to e^-e^+$)	$(5.940 \pm 0.006)\%$
BR (J/$\psi \to \mu^-\mu^+$)	$(5.930 \pm 0.006)\%$
BR (J/$\psi \to hadrons$)	$(87.7 \pm 0.5)\%$

Table 2.1: The properties of J/ψ with branching ratios. Taken from [28].

Chapter 3

Brief review of models and previous measurements

In this chapter I will summarize measurements of J/ψ vector meson photoproduction in UPC in different experiments. I will also briefly mention some of the models that have been used to attempt to describe the measured data.

3.1 Models for J/ψ photoproduction in photon-nucleus interactions

The experimental results have to be compared with models in order to get some physical conclusion about nuclear phenomena. Different models use different approaches how to calculate the cross section of the photonuclear interaction. These models can be divided into two groups, where first one is based on an explicit dependence on the square of the nuclear gluon distribution and the second one uses the dipole model approach to estimate the photonuclear interaction. The former group is formed by the AB, RSZ and GSZ models and the latter by the GM, CSS, LM and also STARLIGHT models.

3.1.1 A. Adeluyi and C.A. Bertulani (AB) model

This model focuses on investigating the sensitivity of direct photoproduction of heavy quarks and exclusive production of vector mesons to the gluon distributions. The constraints on nuclear shadowing can be done with help of results of gluon distributions obtained from global fits to data on J/ψ photoproduction off proton targets [29].

There are two classification of Fock states, i.e. the interaction of photon with nuclei: direct and resolved. The photon interacts like a point-like particle in direct interaction while in resolved interaction, the photon fluctuates into $q\bar{q}$ pair or more complex state including also gluons. The latter contribution is interprated as a hadroproduction of heavy quarks and at LO involves gluon-gluon and $q\bar{q}$ subprocesses. Summing both contributions, the cross section of photoproduction of a pair of heavy quarks can be obtained [29]. The total photoproduction cross section is then obtained as a convolution of this sum with the photon flux as in Eq. (2.8).

The cross section for the exclusive vector meson V production in nucleus-nucleus collisions at LO is expressed in formula Eq. (3.1) at zero transferred momentum in the interaction vertex, i.e. $t = 0$, where t is the Mandelsthram variable. In case $t = 0$ the cross section is called forward cross section.

$$\frac{d\sigma^{\gamma A\to VA}}{dt}\Big|_{t=0} = \chi\frac{16\pi^3\alpha_s^2\Gamma_{ee}}{3\alpha M_V^5}[xg_A(x,Q^2)]^2, \tag{3.1}$$

where $x = (M_V^2/W_{\gamma p})^2$ is the fraction of the nucleon momentum carried by the gluons. The $g_A(x,Q^2) = g_p(x,Q^2) \times R_g^A(x,Q^2)$ is the nuclear gluon distribution in nuclei obtained by multiplying the gluon distribution in proton $g_p(x,Q^2)$ by the gluon modification $R_g^A(x,Q^2)$, χ is the correction for phenomenological factors, Γ_{ee} is the leptonic decay width, α_s and α are the strong and fine coupling constant, respectively and $Q^2 = (M_V/2)^2$ is the scale, the momentum transfer with mass of the vector meson.

The relation between the gluon distribution in proton and that in nuclei is an important feature of the AB theory. The gluon distribution in the proton is experimentally known and with this relation, the information about the effects in the nuclei and their influence to the observed gluon density is incorporated in the gluon modification factor $R_g^A(x,Q^2)$.

The cross section in Eq. (3.1) can be extended to the general form, where t is non-zero, using the target form factor, which is the Fourier transform of the Wood-Saxon nuclear density.

Four different parametrization sets for the nuclear modification $R_g^A(x,Q^2)$ were used to describe parton distributions. For the proton it was used the Martin-Stirling-Thorne-Watts (MSTW08) parton distributions available up to next-to-next-to-leading order (NNLO). For the nuclear case, there are three sets available. Eskola, Paukunnen and Salgado have two sets EPS08 up to leading order (LO) and EPS09 up to next-to leading order, such as the third one HKN07 by Hirai-Kumano-Nagai. In this case, the factorization scale is $Q^2 = M_{\mathrm{J}/\psi}^2$ for the elastic photoproduction of the J/ψ meson [29].

The MSTW08 model has as a purpose to describe the nuclear modification with the absence of nuclear effects, that is $R_g^A(x,Q^2) = 1$. Then as seen in Fig. 3.1, the HKN07 parameterization shows weak gluon shadowing as a function of low x and it extends well into the antishadowing region directly into the Fermi motion region, without any mark about the EMC nor, antishadowing effects, see for comparison Fig. 1.6. Stronger, or in other words, moderate nuclear gluon shadowing shows the EPS09 prediction with clear antishadowing and EMC effects and quite visible Fermi motion. The strongest nuclear shadowing exhibits the EPS08 model, which also predicts quite strong antishadowing and EMC effects to the substantial Fermi motion.

The prediction from Eq. (3.1), which connects the cross section with the gluon distribution can be seen in Fig. 3.2, where is depicted the cross section of the photoproduction of J/ψ at nominal energy $\sqrt{s_{\mathrm{NN}}} = 5.5$ TeV. There can be nicely seen the strong suppression of the cross section with the prediction of the strongest nuclear gluon shadowing, which is EPS08 while on the other hand, the cross section is enhanced with a model which does not include any nuclear effects, i.e. MSTW08.

3.1.2 V. Rebyakova, M. Strikman, M. Zhalov (RSZ) model

As in the AB model, also here the studies were performed for $\sqrt{s_{\mathrm{NN}}} = 5.52$ TeV. The RSZ model assumes coherent J/ψ photoproducton in UPC through the interaction of a small color dipole of a size $\sim 0.2 - 0.25$ fm, where the dominant mechanism is the coupling of two gluons to the $c\bar{c}$ dipole, in case of J/ψ, thus forming the beginning of a gluon ladder. Similar to the AB model, the photonuclear cross section can be calculated using Eq. (3.1). When this formula is applied to the proton and nuclear target, the cross section for the photoproduction of the hidden heavy flavor vector meson J/ψ off heavy nuclei can be obtained. The key of the RSZ model is similarly as in AB the ratio of the nuclear gluon

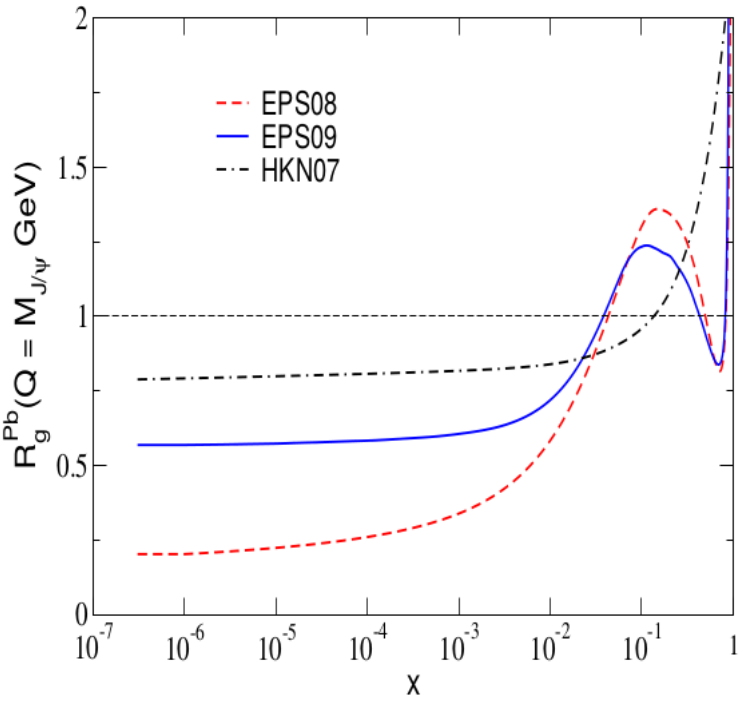

Figure 3.1: Nuclear gluon modification $R_g^A(x, Q^2)$ in particular for Pb ion $R_g^{Pb}(x, Q^2 = M_{J/\psi}^2)$ as a function of x with different prediction depicted. Taken from [29].

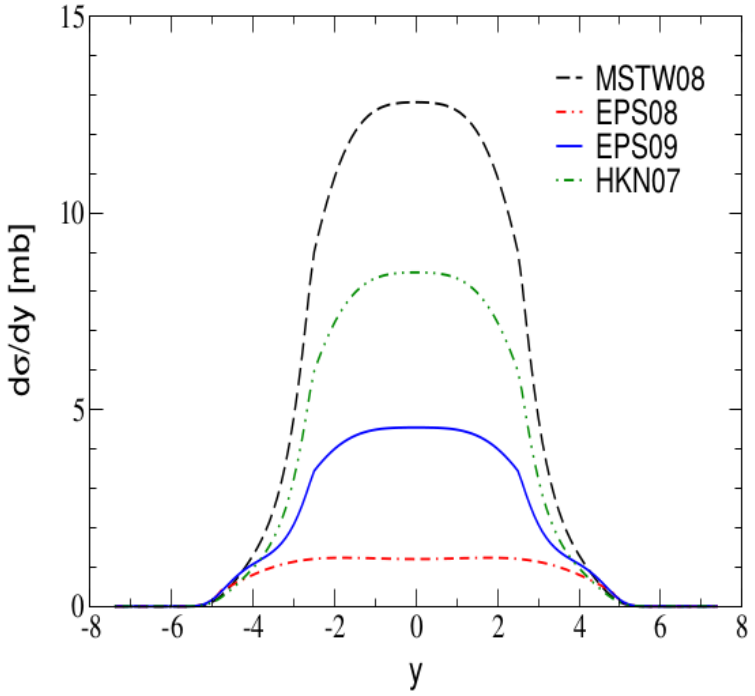

Figure 3.2: Rapidity distributionss of exclusive photoproduction of J/ψ in PbPb collisions at the LHC compared to different model predictions, see text. Taken from [29].

density distribution $G_A(x,\mu^2)$ to the proton gluon distribution $G_N(x,\mu^2)$, where μ is the scale $\mu = M_{J/\psi}/2$ [30].

This ratio can be evaluated with the Leading Twist Approximation (LTA) to nuclear shadowing, which describes the interaction of the virtual photon as a series of the simultaneous interactions with nucleons in nucleus, where in the final state can be the J/ψ meson.

The basis for the LTA is Gribov's theory of inelastic shadowing, DGLAP evolution equations and factorization, see Section 1.1.4. As an input to this model serves nucleon diffractive parton distribution functions (PDF) available at NLO and LO and for this study was chosen the LO PDFs. Besides, the LO gluon density $G_N(x,\mu = 2.5\ \mathrm{GeV}^2)$ in proton found by Durham-PNPI group in the range $10^{-4} < x < 10^{-2}$ by fitting the cross section by HERA was used as another input.

3.1.3 V.P. Goncalves and M.V.T. Machado (GM) model

The GM model also assumes the photon flux of two colliding nuclei with atomic number Z to be described by Eq. (2.8) where both target and projectile could be emitters of the photons [31].

The GM model is based on a color dipole framework, where the hadron carries the most of the energy, while the photon has just a small fraction enough to dissociate into a $q\bar{q}$ pair, see Section 1.1.4.

3.1.4 A. Cisek, W. Schäfer and A. Szczurek (CSS) model

The CSS model uses a framework to predict the exclusive coherent diffractive production of J/ψ and Υ vector mesons, based on Glauber-type rescattering of color dipoles in the nuclear matter and on gluon shadowing corrections, which are associated with the multiple rescattering of the $q\bar{q}g$ - Fock states [32].

As was already mentioned in Sec. 1.1.4, with increasing energy more nuclear subprocess become visible to the probe, i.e. higher Fock-states $q\bar{q}g$, $q\bar{q}gg$, etc. Iterating the nonlinear Balitsky-Kovchegov evolution equation can be obtained the multiple scattering of the $q\bar{q}g$-Fock states off a heavy nucleus. First, it is evaluated for the higher x and then evolved to the lower x.

The impulse approximation (IA) serves well to quantify the multiple scattering, i.e. nuclear effects. Since the impulse approximation uses an assumption of only one nucleon interacting in the nucleus and the rest of nucleons are just spectators, it provides a good reference as a comparison to the nuclear effects in the nuclei through the ratio $R_{coh}(W)$, where W is the center-of-mass energy; $x = m_V^2/W^2$.

$$R_{coh}(W) = \frac{\sigma_{\mathrm{tot}}(\gamma A \to VA; W)}{\sigma_{\mathrm{tot,IA}}(\gamma A \to VA; W)}, \tag{3.2}$$

where σ_{tot} is the total photoproduction cross section on the nucleus and $\sigma_{\mathrm{tot,IA}}$ is the impulse approximation. In Fig. 3.3 we can see this ratio as a function of W for the lead nucleus for both J/ψ and Υ vector meson production. As can be seen, the J/ψ displays stronger gluon shadowing, nuclear effects, than the Υ. The reason can be found in the dipole formalism, where the dipole radius is given as $r \propto 1/m_Q$. Thus the smaller dipole will experience less scattering effects, which is the case of Υ in comparison to J/ψ.

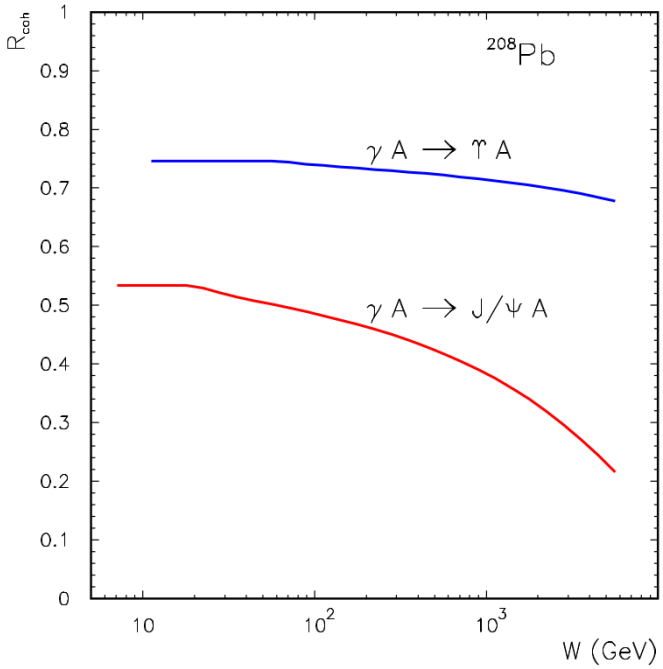

Figure 3.3: The ratio R_{coh} of the nuclear cross section for vector mesons J/ψ and Υ to the impulse approximation as a function of W. Taken from [32].

3.1.5 T. Lappi and H. Mäntysaari (LM) model

Another model based on the color dipole formalism is the model by Lappi and Mäntysaari [33]. The LM model assumes the validity of the dipole model in the region of slow gluons, i.e. $x < 0.02$. Different parametrizations of the dipole-proton cross section are available. Ideal situation would be fitting the initial condition of the BK evolution equation to the DIS data, after that solve BK equation, extract the dipole amplitude for further use like computing the diffractive vector meson production. When in the BK is included dependence on the impact parameter, the BK then leads to strange results with the evolution, such as growing of the size of the proton. This can be regulated at the confinement scale, for more detail see [34]. Due to this feature, two phenomenological dipole cross section parametrizations dependent on realistic impact parameter are used, i.e. IIM dipole cross section which uses values from the fit to HERA data in BK evolution equation and IPsat model, which uses DGLAP-evolved gluon distribution. In Fig. 3.4 is depicted the coherent diffractive J/ψ photoproduction cross section in Pb–Pb collisions at $\sqrt{s_{\mathrm{NN}}} = 2.76$ TeV for $Q^2 = 0$ GeV^2 computed using fIPsat and IIM parametrizations and are compared to ALICE data, where fIPsat is some approximation of IPsat, see [33].

3.1.6 STARLIGHT by Spencer R. Klein and Joakim Nystrand

The authors consider the exclusive reaction of $A + A \rightarrow A + A + V$, where A is the heavy nucleus and V is the vector meson and this reaction proceeds through the photon-Pomeron or photon-meson interaction [35].

In this model, it is assumed the rest frame of one of the nuclei-target, and large energy of the photon, but small transfer momentum, $t_{\mathrm{min}} = \sqrt{M_V^2/4k}$, where k is the photon momentum. The nuclear density is described by a Woods-Saxon distribution. The photo-nucleus cross section $\gamma A \rightarrow VA$ is calculated using Glauber model with photo-nucleon cross section $\gamma p \rightarrow Vp$ as an input. The cross section can be parametrized using fits to

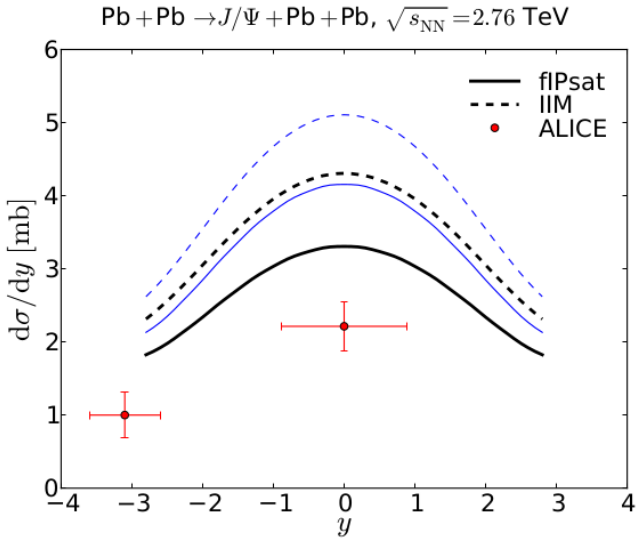

Figure 3.4: The model prediction with data from ALICE. Taken from [32].

available data at HERA. Authors then used the Vector Dominance Model (VDM) to relate this cross section to nuclei as

$$\frac{\mathrm{d}\sigma(\gamma p \to Vp)}{\mathrm{d}t}\Big|_{t=0} = \frac{4\pi\alpha}{f_v^2}\frac{\mathrm{d}\sigma(Vp \to Vp)}{\mathrm{d}t}\Big|_{t=0}, \tag{3.3}$$

where t is the squared 4-momentum transfer between the proton and vector meson, α is the electromagnetic coupling constant and f_v is the coupling of vector meson to photon [35]. The total cross section of the photo-nucleon process is given by the optical theorem as

$$\sigma_{\mathrm{tot}}^2(VP) = 16\pi\frac{\mathrm{d}\sigma(Vp \to Vp)}{\mathrm{d}t}\Big|_{t=0} \tag{3.4}$$

and with Glauber calculation the total cross section for heavy nuclei is

$$\sigma_{\mathrm{tot}}(VA) = \int \mathrm{d}^2\vec{r}\Big(1 - e^{-\sigma_{\mathrm{tot}}(Vp)T_{AA}(\vec{r})}\Big), \tag{3.5}$$

where $T_{AA}(\vec{r})$ is the overlap function.

Applying again the optical theorem for nucleus A and a generalized vector meson dominance model (GVDM), which includes some necessary corrections, see [35], we find a photonuclear cross section as

$$\frac{\mathrm{d}\sigma(\gamma A \to VA)}{\mathrm{d}t}\Big|_{t=0} = \frac{\alpha\sigma_{\mathrm{tot}}^2(VA)}{4f_v^2} \tag{3.6}$$

Using the nuclear form factor and integrating the photonuclear cross section over the photon spectrum we obtain the total cros section $\sigma(AA \to AAV)$.

3.2 Photoproduction of J/ψ and high mass e^-e^+ in ultra-peripheral Au+Au collisions at $\sqrt{s_{\rm NN}} = 200$ GeV.

Here, I review the first measurement of photoproduction of J/ψ and two-photon production of high-mass e^-e^+ pairs in UPC with Au+Au data at $\sqrt{s_{\rm NN}} = 200$ GeV [36]. The study with PHENIX detector at the BNL Relativistic Heavy Ion Collider (RHIC) focuses on the measurement of exclusively produced high-mass e^+e^- pairs, i.e. there is basically zero background, at mid-rapidity in a process of Au+Au $\rightarrow$ Au+Au+e$^-$e$^+$. At RHIC energies the Lorentz factor $\gamma = 108$ and the maximum photon energy, from Eq. (2.7) is $\omega_{max} \sim 3$ GeV. This corresponds to maximum photon-nucleon center-of-mass energies $W_{\gamma N}^{max} \sim 34$ GeV. J/ψ probes nuclear Bjørken-x at values of $x \sim m^2_{\rm J/\psi}/W^2_{\gamma A} \approx 1.5 \times 10^{-2}$, which is the region where nuclear shadowing effect is present. The Feynman diagrams for exclusive photoproduction of J/ψ and dielectrons in UPC Au+Au collision at PHENIX is depicted in Fig. 3.5.

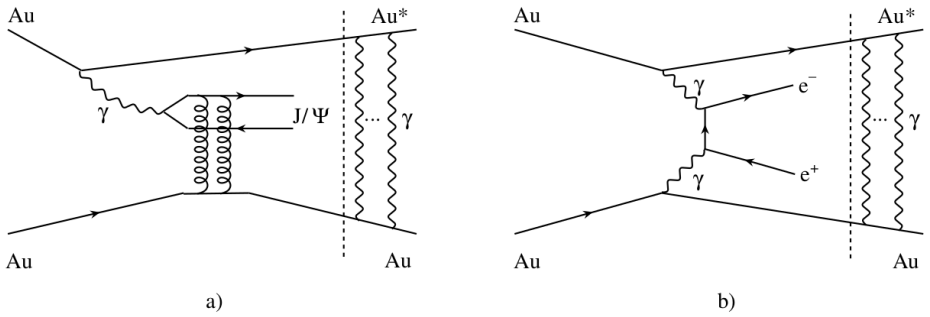

Figure 3.5: The Feynmann diagrams for exclusive photoproduction of J/ψ a) and dielectrons b) in UPC Au+Au collision at PHENIX. Taken from [36].

3.2.1 Selection criteria and results

The events used in the UPC analysis at PHENIX were collected for the first time with the UPC trigger set up in 2004. The efficiency of the trigger was estimated to the value $\epsilon^{e^-e^+}_{trigg} = 0.9 \pm 0.1$. The 8.5×10^6 UPC triggered events were collected from which the total number of 6.7 M satisfied standard data quality assurance criteria, see more in [36]. The corresponding integrated luminosity was $\mathscr{L} = 141 \pm 12\ \mu$b^{-1} computed from the minimum bias triggered events. After the selection criteria in [36], the PHENIX collaboration found 28 events of e^-e^+ pair within $2 < m_{e^-e^+} < 6$ GeV. After the subtraction of the e^-e^+ continuum, the total number of found J/ψ was $N_{\rm J/\psi} = 9.9 \pm 4.1({\rm stat}) \pm 1.0({\rm syst})$. The final cross section of J/$\psi + Xn$, where Xn is a number of emitted neutrons in the coherent photoproduction, calculated from Eq. (3.7) can be seen in Fig. 3.6.

$$\frac{{\rm d}\sigma}{{\rm d}y} = \frac{N_{\rm J/\psi}}{{\rm BR}({\rm Acc} \times \epsilon \times \epsilon_{\rm trigg})\mathscr{L}\Delta{\rm y}} = 76 \pm 31\ ({\rm stat}) \pm 15\ ({\rm sys})\ \mu{\rm b}. \tag{3.7}$$

3.3 Coherent J/ψ photoproduction in ultra-peripheral Pb–Pb collisions at $\sqrt{s_{\rm NN}} = 2.76$ TeV

Also the ALICE Collaboration has made the first measurements at the LHC of J/ψ photoproduction in ultra-peripheral collisions at $\sqrt{s_{\rm NN}} = 2.76$ TeV [37].

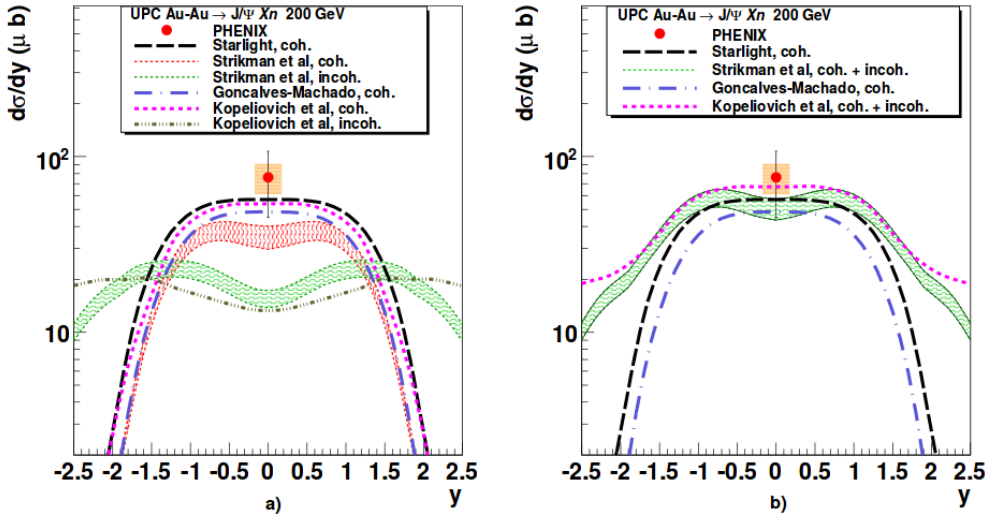

Figure 3.6: The cross section of $J/\psi + Xn$ at mid-rapidity at $\sqrt{s_{\rm NN}} = 200$ GeV compared to the theoretical predictions of STARligt, Strikman, Goncalves-Machado and Kopeliovich. Coherent and incoherent theoretical calculations are shown separately in a) and summed up in b). Taken from [36].

At ALICE were studied the two-photon and photonuclear interactions in coherent photoproduction, but in this case the sources for these interactions were lead ions. The study was done in the forward rapidity region ($-3.6 < y < -2.6$) through the dimuon decay, which with the Eq. (2.15) at hard scale $Q^2 \approx M^2_{\rm J/\psi}/4$ results in values of Bjørken-x at $x \sim 10^{-2}$ and $x \sim 10^{-5}$ where the first component contributes the majority (more than 90%) of the cross section.

3.3.1 Analysis and the results

The analysis is done on a sample of events collected during the 2011 Pb–Pb run, on which was applied a special UPC trigger to obtain a dimuon pair within the acceptance of the detector. The integrated luminosity during this time periods was $\mathscr{L} = 55\ \mu{\rm b}^{-1}$. For more details about the special requirements of the UPC trigger see [37]. The total number of triggered events was 3.16×10^6.

The muon spectrometer was used for the forward analysis, which had to satisfied the requirement of only two tracks hit and very low J/ψ transverse momentum. The $p_{\rm T}$ cut for the dimuon pairs was chosen to be $p_{\rm T} < 300$ MeV due to the study of coherent photoproduction and to reconstruct the J/ψ, the pairs had to be in an invariant mass region of $2.8 < M_{inv} < 3.4$ GeV, which reduced the number of accepted events to 122.

The acceptance and efficiency of coherent and incoherent J/ψ reconstruction was calculated from Monte Carlo simulation. The events generated by STARLIGHT, which is defined in Chapter 5, were passed through the simulated detector layout to obtain a number of reconstructed events. From the ratio of reconstructed events over generated, the acceptance and efficiency (Acc $\times\, \epsilon$) is estimated to be 16.6 % and 14.4 % for coherent and incoherent J/ψ, respectively.

To obtain the cross section, the same formula as in Eq. (3.7) was used. The J/ψ yield was extracted by fitting the invariant mass spectrum in range $2.2 < M_{\rm inv} < 4.6$ GeV with an exponential and Crystal Ball function to describe the continuum and the signal, respectively. After that corrections for the J/ψ coming from the feed down f_D of

ψ(2S) and to the incoherent contribution f_I in coherent J/ψ yield were done, giving the resulting values $f_D = (11 \pm 6)\%$ and $f_I = 0.12^{+0.14}_{-0.04}$. Hadronic contamination was found to be negligible, i.e. ~ 0.8 hadronic events in p_{T} region $p_{\mathrm{T}} < 300$ MeV. After all corrections the final yield of coherent J/ψ is $N^{\mathrm{coh}}_{\mathrm{J}/\psi} = 78 \pm 10(\mathrm{stat})^{+7}_{-11}(\mathrm{syst})$. Putting all together, the cross section was calculated to be $\mathrm{d}\sigma^{\mathrm{coh}}_{\mathrm{J}/\psi}\mathrm{dy} = 1.00 \pm 0.18(\mathrm{stat})^{+0.24}_{-0.26}(\mathrm{syst})$ mb.

In Fig. 3.7 can be seen this cross section compared to the different models. The best agreement is with models including moderate nuclear shadowing, which are RSZ-LTA, AB-EPS09 and AB-EPS08.

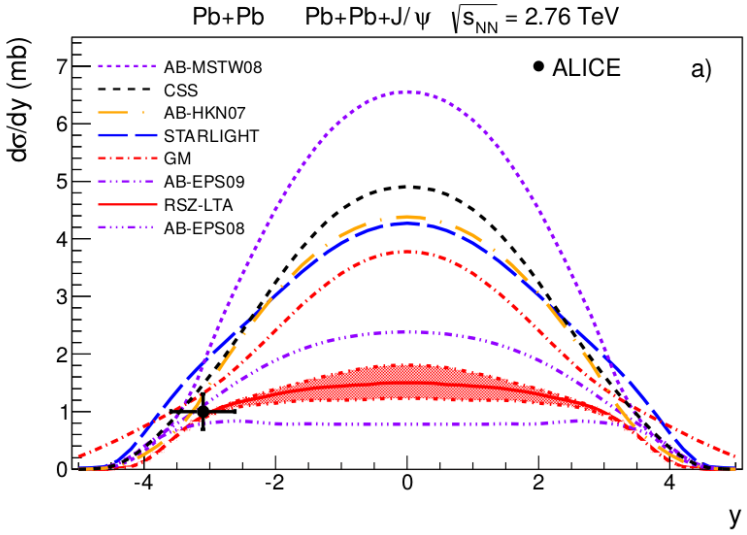

Figure 3.7: The cross section of J/ψ at forward rapidity at $\sqrt{s_{\mathrm{NN}}} = 2.76$ TeV compared to the theoretical predictions. Taken from [37].

3.4 Charmonium and e^+e^- pair photoproduction at mid-rapidity in ultra-peripheral Pb–Pb collisions at $\sqrt{s_{\mathrm{NN}}} = 2.76$ TeV

Another measurement of J/ψ photoproduction was provided by the ALICE Collaboration at the LHC at $\sqrt{s_{\mathrm{NN}}} = 2.76$ TeV, but this time at mid-rapidity [38]. The measurement at mid-rapidity allow the exploration of nuclear gluon distribution at $x \approx (M_{\mathrm{J}/\psi}/\sqrt{s_{\mathrm{NN}}})\exp(\pm y) \approx 10^{-3}$. The result of this analysis is the measured cross section of both coherently and incoherently produced J/ψ vector mesons and a comparison with the model predictions.

3.4.1 Event selection and results

This analysis was based on a sample collected during 2011 Pb–Pb data taking, which were selected by a dedicated Barrel Ultra-Peripheral Collision trigger set up to trigger events with only two hits in otherwise empty detector. For detailed characteristics of BUPC see [38]. The total amount of selected events by BUPC was 6.5×10^6. The integrated luminosity was $\mathscr{L} = 23.0^{+0.7}_{-1.2}\ \mu b^{-1}$. Here, with the central barrel is possible to study the decay channel of J/ψ to dimuons, but also to dielectrons. After the event selection, the p_{T} cut to dileptons was applied. To obtain the incoherent enriched sample of dimuons, the

events were selected with $p_{\mathrm{T}} > 200$ MeV and for dielectrons $p_{\mathrm{T}} > 300$ MeV in an invariant mass range $2.8 < M_{\mathrm{inv}} < 3.2$ GeV. The analysis of the invariant mass spectrum was done similarly as in the previous section, fitting with the Crystal Ball function and with the exponential function and the result from fit was corrected to incoherent contribution and that from feed down, see [38]. The acceptance and efficiency was calculated similarly as in previous section and gave the result for $\mathrm{J}/\psi \to e^-e^+(\mu^-\mu^+)$ 2.71 (4.57 %) and 1.8 (3.19 %) for coherent and incoherent J/ψ, respectively.

The cross section for the dimuon channel is $\mathrm{d}\sigma^{coh}_{\mathrm{J}/\psi}/\mathrm{d}y = 2.27 \pm 0.14\ (\mathrm{stat})^{+0.30}_{-0.20}(\mathrm{syst})$ mb and for dielectron is $\mathrm{d}\sigma^{coh}_{\mathrm{J}/\psi}/\mathrm{d}y = 3.19 \pm 0.50\ (\mathrm{stat})^{+0.45}_{-0.31}(\mathrm{syst})$ mb. The weighted cross section is $\mathrm{d}\sigma^{coh}_{\mathrm{J}/\psi}/\mathrm{d}y = 2.38^{+0.34}_{-0.24}\ (\mathrm{stat} + \mathrm{syst})$ mb.

The incoherent yield was also corrected for the feed down f_D and for the coherent contribution f_C, see Table 3.1 and cross section for dielectron is $\mathrm{d}\sigma^{\mathrm{inc}}_{\mathrm{J}/\psi}/\mathrm{dy} = 0.87 \pm 0.20(\mathrm{stat})^{+0.26}_{-0.14}$ (sys) mb and for dimuons is $\mathrm{d}\sigma^{\mathrm{inc}}_{\mathrm{J}/\psi}/\mathrm{dy} = 1.03 \pm 0.17(\mathrm{stat})^{+0.15}_{-0.12}$ (sys) mb. The weighted cross section is $\mathrm{d}\sigma^{\mathrm{inc}}_{\mathrm{J}/\psi}/\mathrm{dy} = 0.98^{+0.19}_{-0.17}\ (\mathrm{stat} + \mathrm{syst})$ mb.

Sample	Coherent $\mathrm{J}/\psi \to \mu^-\mu^+$	Coherent $\mathrm{J}/\psi \to e^-e^+$	Incoherent $\mathrm{J}/\psi \to \mu^-\mu^+$	Incoherent $\mathrm{J}/\psi \to e^-e^+$
f_D	$0.1^{+0.05}_{-0.06}$	$0.1^{+0.05}_{-0.06}$	0.095 ± 0.055	0.11 ± 0.07
f_I	0.044 ± 0.014	0.15 ± 0.02	-	-
f_C	-	-	0.03 ± 0.03	0.47 ± 0.09

Table 3.1: Summary of the correction to feed down f_D, coherent f_C and incoherent f_I contribution of the yield. Taken from [38].

In Fig. 3.8 are depicted the weighted cross sections, coherent cross section a) and incoherent b). Both measurements are compared with the model predictions. The EPS09 nuclear gluon prediction by Adeluyi and Bertulani is in very good agreement. Those calculations using Glauber model overestimates data by a factor 1.5-2. In other hand, the model which includes strong gluon shadowing AB-EPS08 underestimates the cross section by a factor of 2.

The incoherent cross section is compared to three different models STARLIGHT, RSZ-LTA and LM, where no model agrees with the measured data well.

An interesting calculation is the ratio of incoherent over coherent cross section, which gives the value $0.41^{+0.10}_{-0.08}$(stat+sys). This ratio can be compared with 0.41 from STARLIGHT, 0.17 from RSZ-LTA and 0.21 from LM. Although STARLIGHT has the correct ratio, it does not reproduce any of the measured cross section. The RSZ-LTA is in relatively good agreement with the coherent cross section at mid-rapidity, however it unpredicts the incoherent cross section and so does the LM model with the ratio.

3.5 Coherent $\psi(2\mathrm{S})$ photo-production in ultra-peripheral Pb–Pb collisions at $\sqrt{s_{\mathrm{NN}}} = 2.76$ TeV

This is the first measurement of the coherent $\psi(2\mathrm{S})$ cross section in UPC Pb–Pb collision at the LHC with ALICE [39]. This charmonium state was studied through the reconstructed direct decay channel $\psi(2\mathrm{S}) \to l^-l^+$, i.e. direct decay channel into two leptons and through $\psi(2\mathrm{S}) \to \mathrm{J}/\psi + \pi^-\pi^+$ decay, where $\mathrm{J}/\psi \to l^-l^+$. This measurement was done at mid-rapidity $|y| < 0.9$ and no other measurements of $\psi(2\mathrm{S})$ coherent photo-production off nuclear targets has been done previously.

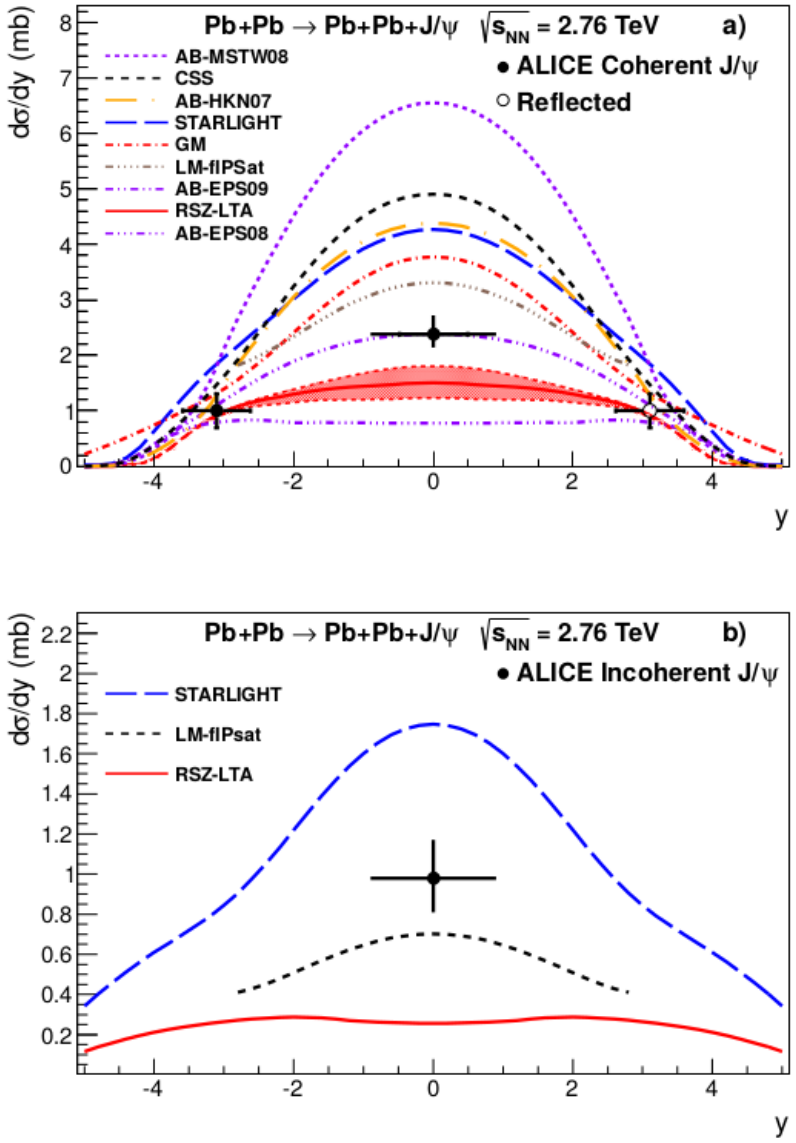

Figure 3.8: Coherent cross section a) compared to different models and incoherent cross section b). Taken from [37].

3.5.1 Analysis and results

As in the previous section, here it was also used the the same trigger (the same data sample) as for previous barrel J/ψ, since this analysis was done at mid-rapidity. The integrated luminosity was $\mathscr{L} = 22.4^{+0.9}_{-1.2}\ \mu\text{b}^{-1}$. The detailed event selection for both channels can be seen in [39]. After the event selection, the dilepton pairs coming from the direct decay channel were selected in p_{T} in the way $p_{\text{T}} < 0.15$ GeV for dimuons and $p_{\text{T}} < 0.3$ GeV for dielectrons. To obtain the yield of ψ(2S), the invariant mass spectrum was fitted by a Crystal Ball to extract the number of ψ(2S) and the background was evaluated by a fit with an exponential function. The acceptance and efficiency was calculated again as the ratio of the number of the reconstructed events from Monte Carlo to the number of generated events with the ψ(2S). Also here the yield of ψ(2S) was corrected to the contribution of incoherently produced ψ(2S) and for the remaining background studying the wrong sign events, which was estimated to be 0. Finally the cross section $\text{d}\sigma^{\text{coh}}_{\psi(2\text{S})}/\text{d}y = 0.76 \pm 0.40(\text{stat})^{+0.12}_{-0.13}(\text{sys})$ mb. For the decay channel where ψ(2S) decays into pions and leptons, the event selection was slightly different, but the p_{T} cut was the same. The measured cross section for $\psi(2\text{S}) \to \mu^-\mu^+\pi^-\pi^+$ was $\text{d}\sigma^{\text{coh}}_{\psi(2\text{S})}/\text{d}y = 0.81 \pm 0.22(\text{stat})^{+0.09}_{-0.10}(\text{sys})$ mb and for $\psi(2\text{S}) \to e^-e^+\pi^-\pi^+$ was $\text{d}\sigma^{\text{coh}}_{\psi(2\text{S})}/\text{d}y = 0.89 \pm 0.31(\text{stat})^{+0.13}_{-0.12}(\text{sys})$ mb. These cross sections were combined as a weight using the statistical and the uncorrelated systematic uncertainty. The average cross section is then $\text{d}\sigma^{\text{coh}}_{\psi(2\text{S})}/\text{d}y = 0.83 \pm 0.19(\text{stat} + \text{sys})$ mb. Fig. 3.9 shows the weighted cross section of ψ(2S) compared to different model predictions. This measurement disfavors models, which consider that all nucleons contribute to the scattering and those with strong shadowing.

The authors of this article also did the comparison of cross sections of coherently produced J/ψ and ψ(2S) at mid-rapidity. The ratio obtained from this comparison was $0.34^{+0.08}_{-0.07}(\text{stat} + \text{sys})$, which is more by 2-2.5 σ than predicted by models.

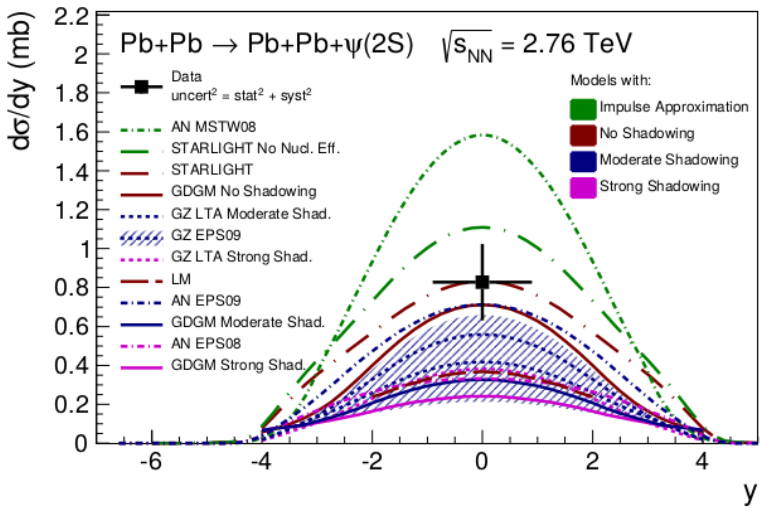

Figure 3.9: Measured differential cross section of ψ(2S) photoproduction in UPC Pb–Pb collisions at $\sqrt{s_{\text{NN}}} = 2.76$ TeV at mid-rapidity at ALICE. Taken from [39].

3.6 Coherent J/ψ photoproduction in ultra-peripheral PbPb collisions at $\sqrt{s_{\mathrm{NN}}} = 2.76$ TeV with the CMS experiment

Measurement accompanied by a neutron emission, at least one on one side of the IP and no neutron activity on the other side was measured with the CMS experiment in ultra-peripheral PbPb collisions at $\sqrt{s_{\mathrm{NN}}} = 2.76$ TeV in the rapidity interval $1.8 < |y| < 2.3$ [40]. The data sample used in this analysis was collected in the 2011 PbPb run and the J/ψ meson was reconstructed in the dimuon decay channel using zero degree calorimeters to detect the neutrons.

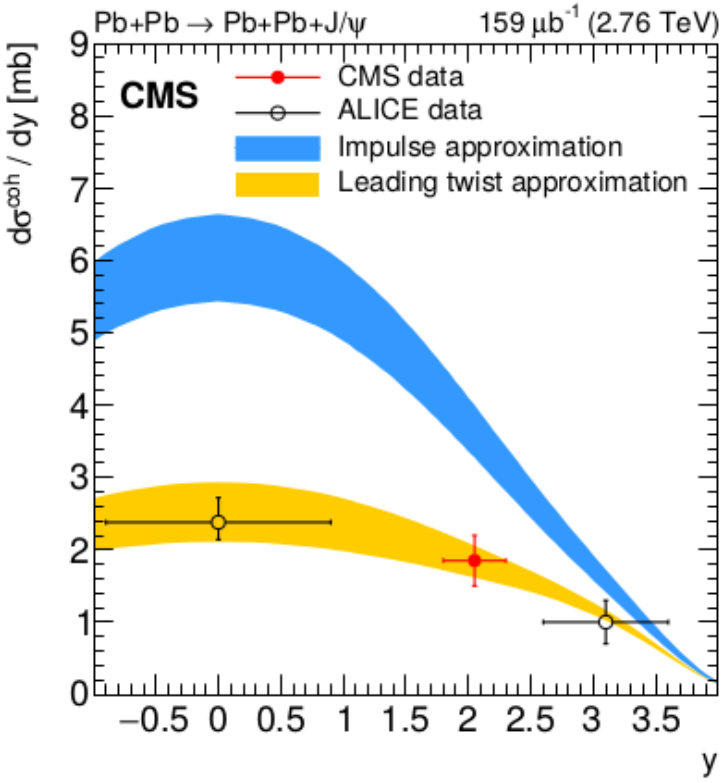

Figure 3.10: Measured differential cross section of J/ψ photoproduction in UPC Pb–Pb collisions at $\sqrt{s_{\mathrm{NN}}} = 2.76$ TeV at CMS compared to ALICE data and different model predictions. Taken from [40].

3.6.1 Results

The detailed event selection and signal extraction can be found in [40]. The coherent J/ψ cross section was given by an equation similar to Eq. (3.7).

$$\frac{\mathrm{d}\sigma^{\mathrm{coh}}_{\mathrm{X_n0_n}}}{\mathrm{d}y} = \frac{\mathrm{N}^{\mathrm{coh}}_{\mathrm{X_n0_n}}}{\mathscr{B}(\mathrm{J}/\psi \to \mu^-\mu^+)\mathscr{L}_{int}\Delta y (A\epsilon)^{\mathrm{J}/\psi}} \tag{3.8}$$

where the branching ratio $\mathscr{B}(\mathrm{J}/\psi \to \mu^-\mu^+) = 5.96 \pm 0.03\%$, $\mathrm{N}^{\mathrm{coh}}_{\mathrm{X_n0_n}}$ is the yield of prompt J/ψ candidates for the region of transverse momentum $p_{\mathrm{T}} < 0.15$ GeV. The integrated luminosity was $\mathscr{L}_{\mathrm{int}} = 159 \pm 8(\mathrm{sys})\mu\mathrm{b}^{-1}$, $\Delta y = 1$ and $(A\epsilon)^{\mathrm{J}/\psi} = 5.9 \pm 0.5$ (stat)% is the acceptance and efficiency. The coherent J/ψ yield was corrected for the feed down, i.e. the fraction of J/ψ coming from the ψ(2S) decay. The resulting differential

cross section is $\frac{\mathrm{d}\sigma^{\mathrm{coh}}_{\mathrm{X_n 0_n}}}{\mathrm{d}y} = 0.36 \pm 0.04(\mathrm{stat}) \pm 0.04(\mathrm{sys})$ mb. To compare this result, the scaling factor between the $X_n 0_n$ break-up mode and the total coherent J/ψ photoproduction cross section 5.1 ± 0.5 (theo) was used, giving the total coherent J/ψ cross section $\mathrm{d}\sigma^{\mathrm{coh}}/\mathrm{dy}_{\mathrm{J}/\psi} = 1.82 \pm 0.22(\mathrm{stat}) \pm 0.20(\mathrm{sys}) \pm 0.19(\mathrm{theo})$ mb. On Fig. 3.10 is compared the measured cross section of coherent J/ψ to ALICE measurements. As seen, the leading twist approximation prediction is in good agreement with both data, i.e. the calculation, which includes the nuclear gluon shadowing [40]. On the other hand, the model, which does not include the nuclear gluon shadowing, impulse approximation, is strongly disfavored.

Chapter 4

Experimental setup

4.1 The Large Hadron Collider

On 20 November 2009 the Large Hadron Collider (LHC) recorded the first proton–proton collision. Since then it completed two periods of data taking of p–p, p–Pb, Xe–Xe and Pb–Pb collisions, so called Run1 from 2010 to 2013 and Run2 from 2015 to 2018 [41].

This powerful machine is situated roughly 100 meters under the ground sharing the border between France and Switzerland, see Fig. 4.1. It is located in an old tunnel used for the former Large Electron Collider (LEP) with circumference around 27 km.

Technically speaking, the LHC is not a perfect circumference [42, 43]. It consists of eight straight sections and eight arcs. Thanks to the electric and magnetic fields the charged particles can be accelerated and travel in a circular trajectory. They are bent in the arcs by a dipole magnets while in the straight sectors they are accelerated to almost the speed of light by radio-frequency cavities. Accelerated particles do not travel alone. They travel in bunches - groups of $\sim 1.10^{11}$ protons or 7.10^{7} lead ions. To avoid the expansion of the bunches they are squeezed by a specific constellation of quadrupole magnets. Up to 2808 proton bunches and 632 lead ion bunches can be simultaneously accelerated in the LHC. The particles used in the LHC have the same charge sign, thus to produce a collision there are needed two beam pipes in which protons and lead ions circulate separately. Collision then occurs in one of the eight intersection points. Four of them are located at the main experiments of the LHC: ALICE, ATLAS, LHCb and CMS. A very high vacuum must be maintained in the beam pipe in order to avoid any problems such as the interaction of the bunch particles with the residual gas in the beam pipes. The energy reached in Pb–Pb collision is $\sqrt{s_{\mathrm{NN}}} = 5.02$ TeV and that of p–p is $\sqrt{s_{\mathrm{NN}}} = 13$ TeV. To reach such energies there are needed superconductive magnets which must be constantly cooled down to a temperature of 1.9 K. This is achieved by a distribution system of liquid helium.

4.2 A Large Ion Collider Experiment (ALICE)

ALICE focuses on the study of the Quantum Chromodynamics (QCD). It was designed to recreate the extreme conditions of our early Universe such as extreme energy density and temperature. The purpose of these conditions is to create a strongly interacting state of matter called the Quark-Gluon Plasma (QGP).

What is doing ALICE attractive is its excellent Particle Identification (PID) and its low material budget, which is able to withstand high particle multiplicity, to measure hadrons, electrons, muons, photons and detect these particles in a very wide range of the

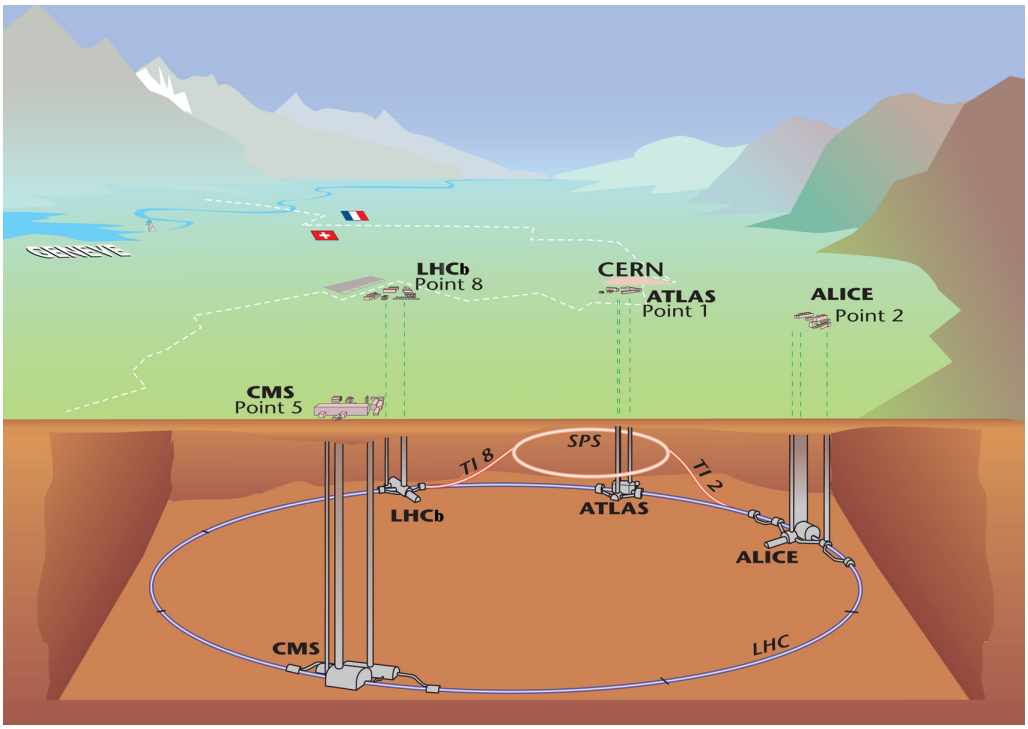

Figure 4.1: The schematic view of cross section of the LHC and its intersection point. ALICE is situated in Point 2. Taken from [44].

transverse momentum down to very low $p_{\mathrm{T}} \sim 0.1$ GeV. Besides this, ALICE also provides a measurement of p–p and p–Pb collisions as a reference measurement to Pb–Pb collisions.

ALICE with its 10 000 t and $26 \times 16 \times 16$ m in dimension is located on the France site 56 m below the surface [46]. The detector consists of two parts: the central barrel part located in a large solenoid magnet with a magnetic field of 0.5 T and the forward muon spectrometer as seen on Fig. 4.2. The mid-rapidity detectors are the following: Inner Tracking System (ITS), Time-Projection Chamber (TPC), Transition Radiation Detector (TRD), Time-Of-Flight (TOF), High-Momentum Particle Identification Detector (HMPID), PHOton Spectrometer (PHOS), ElectroMagnetic CALorimeter (EMCAL) and Alice COsmi Radiation DEtector (ACORDE). It is completed with the forward-rapidity detectors such as Zero Degree Calorimeter (ZDC), Photon Multiplicity Detector (PMD), Forward Multiplicity Detector (FMD), V0, T0 an Diffractive Detector (AD).

The detectors only used for the purpose of this Thesis will be described in more details in the following sections beginning with the closest one to the beam pipe in central barrel to the ones located in the forward rapidity region.

4.2.1 Inner Tracking System (ITS)

The Inner Tracking System is the closest detector to the beam pipe, surrounding it in the whole azimuth and with a pseudorapidity coverage of $|\eta| \leq 0.9$ [46]. It consists of six cylindrical layers of silicon detectors, with a diameter going from 4 cm for the inner layer to 43 cm for the outer layer, Fig. 4.3. Its main tasks are to localize the precise position of the primary vertex, to reconstruct the decay vertices of hyperons and heavy flavor D and B mesons, to track particles and provide particle identification via the energy loss information, $\mathrm{d}E/\mathrm{d}x$, at low momentum and to track the particles which enter the dead regions of the TPC and improve the resolution of tracks reconstructed by the TPC. It

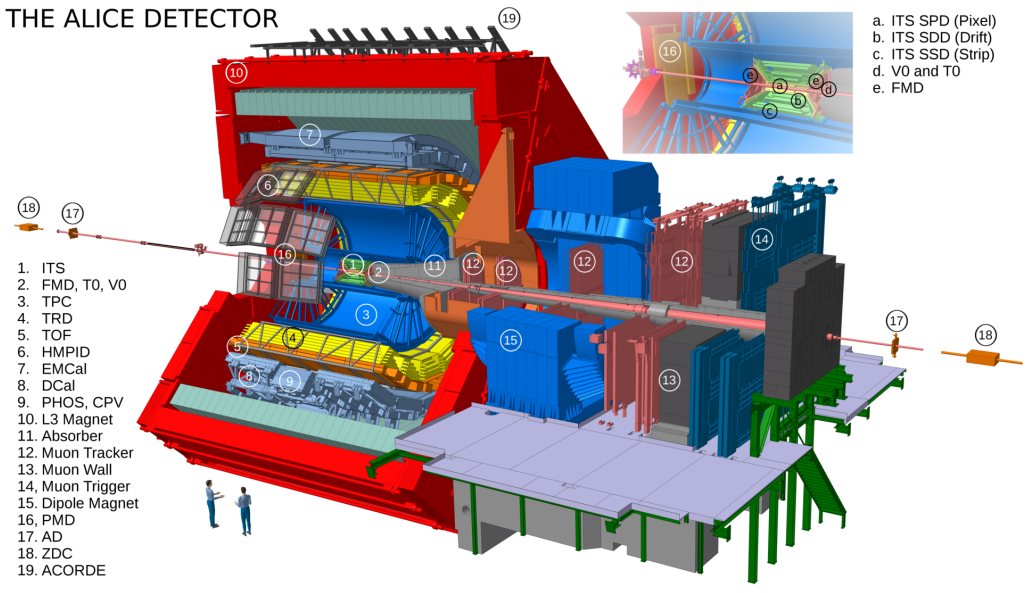

Figure 4.2: The schematic view of the ALICE during Run2 data taking. The red solenoid magnet L3 surrounds the central barrel. The blue magnet is dipole magnet in part where forward muon spectrometer is located. Taken from [45].

contributes to almost all physics provided by the ALICE experiment.

Since ITS is the closest detector to the beam pipe, it is affected the most by the large particle density created in the collision. The density decreases with the distance from the point of the collision. This fact is reflected in the design of the ITS since it has to deal with a large multiplicity and still reconstruct the primary vertices with a high resolution.

For each two layers a different layout was chosen. The two inner layers are formed by the Silicon Pixel Detector (SPD). The middle layers form the Silicon Drift Detector (SDD) and the outer layers form the Silicon Strip Detector (SSD). The four outer layers have analog readout therefore are used for particle identification via energy loss down to low p_{T}. It was important to chose a low budget material to avoid a secondary production of particles an multiple scattering.

The SPD is based on silicon pixels which are split into a two-dimensional matrix of reverse-biased silicon diodes. Each diode is connected to the output of a readout chip. When a charged particle passes through the detector, it transfers the energy to the valence electrons. In case that this energy is sufficient, the electron crosses the energy gap and gets to the conductive band. The electron-hole pair is created and free electrons are collected by the anodes creating a signal to be read out. The advantage of semiconductor detectors is that there is needed around 10 times smaller energy to create an electron-hole pair than that required for the gas ionization and creation of the electron-ion pair instead. The readout is binary, i.e. the readout output is set to 0 unless the signal crosses the given threshold and it changes to 1.

The SDD is operating in moderate particle density. The sensitive area is split into two by a central cathode strip forming two drift regions, Fig. 4.3. The holes are collected by the nearest cathode, while the electrons are conducted to the edge of the detector thanks to the parabolic potential. The SDD provides a two-dimensional information, one dimension is obtained from the signal readout from a row of 256 collection anodes, where electrons are driven and consequently collected and the second dimension is reached from the information of the drift velocity.

The SSD with its two outer layers forms an important role in matching the tracks from

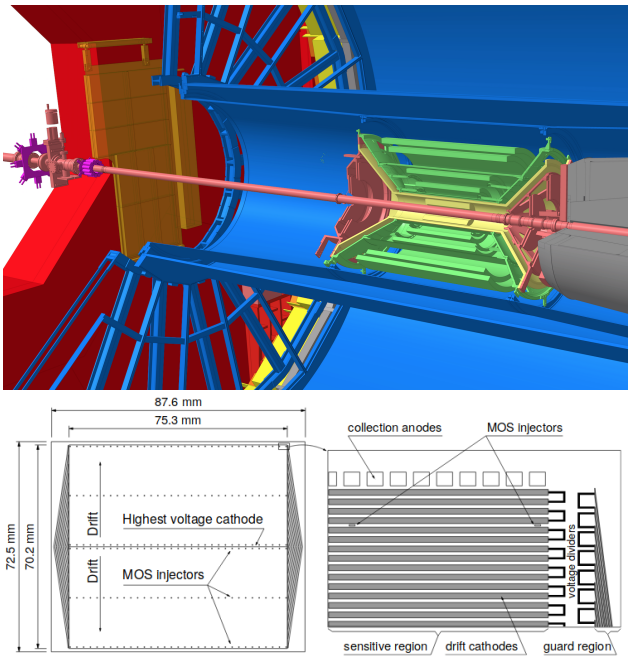

Figure 4.3: Up: The schematic view of the ITS upgrade for Run2 data taking. Down: the cross section along the beam line of the Silicon Drift Detector (SDD) [45, 46].

ITS to the TPC. Since it is located in a region with lower particle density, there is no need to have a layout achieved with the silicon pixel detectors. The SSD consist of double sided strips detectors where the sensors are mounted almost parallel to the magnetic field and readout on the edges of each strip. A hit in one strip is assumed to correspond to one particle, so SSD provides a good spatial precision in the region with low particle density.

4.2.2 Time Projection Chamber (TPC)

The TPC is the main tracking detector of the central barrel [46]. The phase space coverage in pseudo-rapidity is $|\eta| \leq 0.9$. TPC main tasks are to provide charged-particle momentum measurements, particle identification by the energy loss and vertex determination. The particle tracking can be done in a wide momentum range $0.1 \leq p_T \leq 100$ GeV/c with a good resolution.

This cylindrical cage of an inner (outer) radius of about 85 cm (250 cm) and 500 cm in length is filled with 90 m^3 of $Ne/CO_2/N_2$ (90/10/5). Besides, there can be also used Ar gas. The choice of gas is crucial. The mixture must be optimized for drift speed, low diffusion, quenching capability to absorb high energy photons, which might have enough energy to further ionize gas molecules. There were probed another mixtures such as CH_4 and CF_4 but rejected because of ageing properties. The choice of the N_2 fraction improved the quenching. The Ne/CO_2 is so called cold gas, which has a dependence of the drift velocity on the temperature causing the requirement of the TPC thermal stability in the drift volume with $\Delta T \leq 0.1$ K. These fractions are also maintained constant to ensure the stable drift velocity and the gas gain. The filling gas is circulating and constantly cleaning from the impurities with very low fresh gas injection. The pressure is maintained at the same value as the ambient pressure.

When a charged particle traverses this volume, it ionizes the gas molecules creating the electron-ion pairs along its trajectory. In the center of the TPC is located a 100 kV

high-voltage electrode constructed from an thin aluminized Mylar foil of 22 μm. The same reasons for the low budget material as for the ITS are present also in TPC. Together with two opposite axial potential dividers they create a highly uniform electrostatic field with a 400V/cm voltage grade causing the drifting of the primary electrons along the 2.5 m distance to the end plates with a maximum drift time of about 90 μs. Every drifted electron will end in the endcap leaving a sample of the track, which implies up to 159 space points allowing the full reconstruction of the particle trajectory. The combination of the time information from the drift chamber with the 2-dimensional information of the position at the readout chamber provides all together 3D information.

The readout chambers are based on Multi-Wire Proportional Chamber (MWPC), which consists of an anode wire grid centered between two cathode pads, Fig. 4.4. In front of the anode plane the cathode wires with ground potential are placed. This is a precaution to avoid the distortion of the local electric field. Due to the energy gain of drifting electrons, additional electron-ion pairs cause avalanches onto anodes where a large amount of positive ions are created. A consequence of the accumulation of the space charge is that positive ions drift back towards the sensitive volume and distort the electric field. They have to be collected before this could happen.

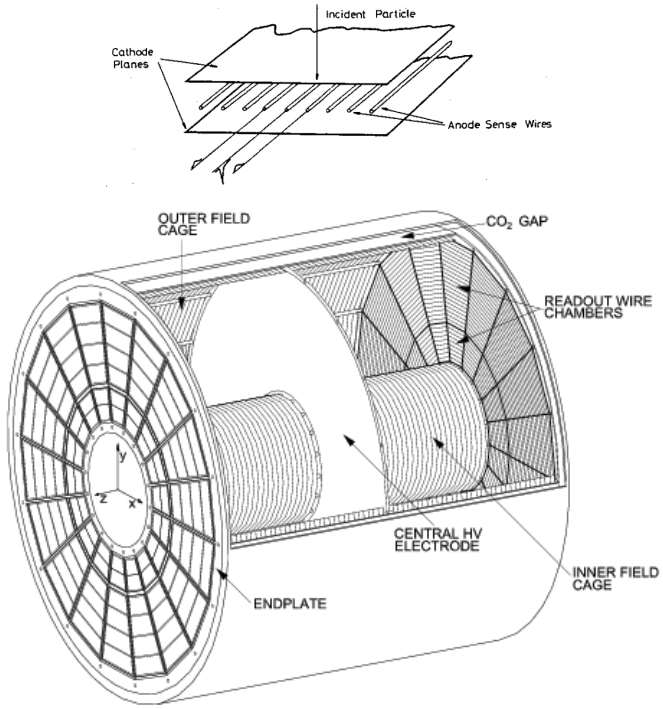

Figure 4.4: Schematic view of the MWPC and TPC during Run2 data taking [46, 47].

4.2.3 Time Of Flight (TOF)

The TOF detector is used mainly for Particle IDentification (PID) in the intermediate momentum range [46]. The pions and kaons are identified below 2.5 GeV/c, protons up to 4 GeV/c and it can provide separation of π/K and K/p better than 3σ. Together with ITS and TPC forms a good tool for track reconstruction. Although for the purpose of this analysis its main use is for triggering.

Due to the large area which had to be covered, again a gaseous detector was chosen

with Multi-gap Resistive-Plate Chamber (MRPC) technology. The electric field is high and uniform in the whole sensitive area. When a charged particle enters the gaseous volume and produces ionization, the avalanches are immediately produced. The generated signal is then picked-up on the electrodes. Particle identification is provided combining time-of-flight of the particle with information on the momentum and track length given by the TPC.

Thanks to the MRPC choice the chamber can operate at the atmospheric pressure, the signal is the analogue sum of signals from gaps, thus it has a well defined peak separated from zero without a tail. There is possibility of a high-gain operation because the resistive plates quench and do not produce sparks and finally the requirements for the construction are rather simple and therefore it could be done from commercially available materials.

The TOF detector is segmented into 18 parts called SuperModules (SM), each 7.5 m long, Fig. 4.2. Every segment contains five gas-tight modules located along the beam-axis. In addition the SM posses the MRPC, the cooling, gas distribution system and the front-end readout board. Also here the geometry of the segments is inclined in different angles to avoid dead zones. The overall area of 141 m^2 results in a low occupancy and good performance.

4.2.4 The forward rapidity detectors: V0, ZDC and AD

The V0 detector consists of two arrays of scintillator counters, [46]. Each counter is installed on either side of the ALICE interaction point (IP). From this is derived the denomination of the scintillators, V0A for the detector situated on A side heading to the ATLAS experiment, 340 cm from the ALICE IP and V0C for the one on C side, C as the CMS experiment, at 90 cm from IP. The pseudo-rapidity coverage is different, $2.8 < \eta < 5.1$ (V0A) and $-3.7 < \eta < -1.7$ (V0C).

The main tasks of the V0 are the triggering and separation of beam-beam (BB) interactions from the accelerator backgroung (beam-gas (BG)). Besides it also contributes to the estimation of the centrality of the collisions and the measurement of the luminosity, which is required to determine absolute cross-sections.

Another forward detector for estimating the centrality is the quartz spaghetti fibre calorimeter called Zero-Degree Calorimeter (ZDC). It takes the advantage of the fact that spectator nucleons, i.e. the nucleons which did no interact in the collision, keep the forward direction (0° relative to the beam pipe) and hit the ZDC. For this reason the ZDC are located at a distance of 112,5 m on either side of ALICE IP. Each ZDC is composed of the neutron calorimeters (ZN) and proton calorimeter (ZP). The neutron spectators are measured by the ZN located between beam pipes, while the charged particles - proton spectators are measured by the ZP placed at the external part of the outgoing beam pipe. Charged particles are deflected by the magnetic field and in this way they are separated from the neutrons.

Another scintillation detector in forward rapidities situated on either sides of the ALICE IP is the Diffractive Detector (AD). It was installed in the long shutdown period between Run1 (2009–2013) and Run2 (2015–2018) to improve the acceptance for diffractive systems with masses below 10 GeV/c^2 and besides that to improve the capability to veto used in case of UPC analyses. AD form 2 groups of 4 scintillator stations each consisting of two scintillating pads covering the pseudo-rapidities $4.9 < \eta < 6.2$ (ADA) and $-6.9 < \eta - 4.9$ (ADC). Charged particles passing through the scintillator layers generate light, which is collected by Wave-Length Shifting bars (WLS), which are connected to photomultiplier tubes by optical fibres.

Each cell of the AD and V0 detector can determine the time when a signal has arrived.

They define time ranges corresponding to arrival times of particles coming from BB or BG interactions.

4.3 The ALICE trigger system

Collisions in the LHC occur at a very high rate so a large amount of different events are created. With a different readout speed of each subsystem of the ALICE detector and limited storage for the data it is impossible to collect data from every single collision, thus only the events with interesting physics must be selected. In addition not all events are suitable to study a particular branch of physics. The events must undergo a process of the selection based on specific criteria, in other words they are triggered. Only after passing successfully whole criteria imposed by different analyses they can be collected, stored and processed. This feature occurs online and it is controlled by the online control system of ALICE. Events are then selected more precisely in the offline framework.

4.3.1 Online control system of ALICE

The Detector Control System (DCS) controls detectors during data taking, checks for possible errors and issues instructions to recover from these failures, thus maximizes the efficiency of the data acquisition [46].

Detectors generating a trigger decision send signals, the so-called inputs, to the Central Trigger Processor (CTP) where they are processed. CTP is the main part of the ALICE trigger, makes a decision about weather to take or reject the event. In case of a positive decision, the CTP then ships the processed information through the Local Trigger Unit (LTU) back into the detector. An event signal is then sent to the front-end read-out electronics (FERO) of the detectors to start the readout. After that the data are injected into Detector Data Links (DDL). Each DDL has on its receiving side the Readout Receiver Card (D-RORC) electronic modules. D-RORC then ships the event fragments into the Local Data Concentrators (LDC) where they are logically assembled into sub-events. Depending on the buffer occupancy of the LDC the Data Acquisition System (DAQ) can decide to enable or disable the most common triggers and send this information to the CTP. After this the sub-events from LDCs are transferred into the Global Data Collectors (GDC) where thanks to the event-building network are built into the whole event. These events then go into the Permanent Data Storage (PDS). At the same time a copy of the raw data is sent into the High Level Trigger (HLT), which permits to select interesting events and send them to the LDCs. The diagram of the flow of the data is depicted in Fig. 4.5.

Every trigger signal has a different latency, i.e. the time between the moment when a collision occurs till the moment when a signal from the interaction is sent to the trigger system. The inputs with similar latencies form three different levels: 24 inputs for Level 0 (L0), 24 inputs for Level 1 (L1) and 12 inputs for Level 2 (L2). The function of the levels is to reject unsatisfactory events as soon as possible and thus reduce the dead time of the system.

The L0 Level has the shortest latency, the trigger decision must be made in less than 1.2 μs. The L0 inputs arrive at the detector within 800 ns. Its decision is based only on a small amount of information from a fraction of detectors with fast response such as SPD, V0, TOF and muon trigger.

Another fast trigger signal is L1 which makes its decision based on the remaining fast detector inputs, like ZDC. The trigger decision arrives back to the detector in 6.5 μs after the collision. Both L0 and L1 carry out the first physics selections.

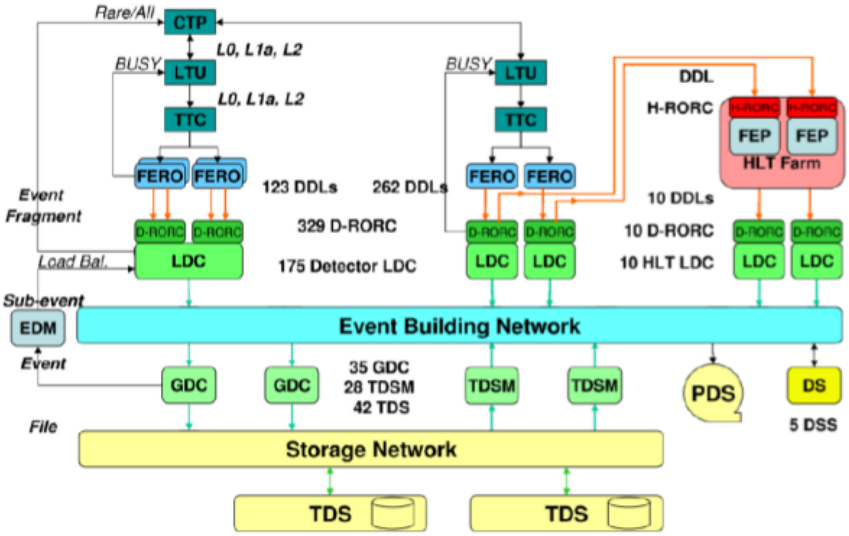

Figure 4.5: The scheme of DAQ. Taken from [46].

An important problem is the contamination of the data sample which may be caused by pile-up effects, i.e. multiple events that occur within a short time window, they have an interaction vertex within ALICE acceptance. As a consequence a mixing of tracks from such events with tracks from triggered events occur. To eliminate this problem, the signal for the requested events is controlled in a time window before and after the collision by the past-future protection circuit (p/f). Although every level checks p/f, the slowest level which waits for the response from all detectors including the slowest TPC and p/f is L2. Because of the long drift time the inputs from L2 arrive at the CTP about 90 μs after the collision.

The trigger system can be set to more than just one configuration in order to select an interesting event of some specific properties. There can be formed the so called trigger class, which defines what trigger detectors are required to have a certain logical combination of a signal. With this manner it defines the input to the CTP.

4.3.2 Offline Framework - Aliroot

After the online process, the events are selected offline according to the particular physics requirements. To do so, it is necessary to have the offline framework with the following tasks: simulation, reconstruction, detector alignment, calibration, visualisation and analysis of data. Particularly for the ALICE collaboration this framework is called Aliroot.

Chapter 5

Analysis results

5.1 Processing of the data until analysis

After the data taking the triggered raw data must pass the process of the reconstruction until they get to the user, i.e. the electronic signal must be converted into the physics quantities. Through the reconstruction several factors must be considered. Every information about the condition of the detector is stored in a database. A set of data which posses stable conditions is called a run. Runs where all detectors needed for a given analysis were working in good condition are selected.

The selected data, i.e. triggered data, are stored in disk and tapes for further analysis. As was already mentioned above, the data are stored in runs. Runs with similar characteristics are stored in periods. In ALICE the denomination of the periods has its own system and every period has its own name, e.g. LHC15o = the LHC stands for Large Hadron Collider, the two number 15 define the year of data taking and the letter o is the given period.

We look at the events in the selected runs, which were triggered by the trigger we chose as a basis for our analysis. The luminosity of this sample is determined at this point. After this, the sample is ready for further preselection.

A set of selection criteria are applied in each event to maximize the efficiency and to minimize the background. Depending on the level of a selection criteria, the data are written in the format of ALICE objects: RAW, ESD and AOD. Raw data are never used for the analysis, as was mentioned above, the ESD is the first reconstruction and preselection which can ocasionally be used for a specific study of the analysis. The smallest object is the AOD and this format is the closest to the analysis.

The data are stored all over the world in computer clusters forming together the ALICE computing GRID. User data analysis on the GRID is parallelized to a set of jobs which can be submitted either by the user or in an organized way using a train of the analysis tasks of several users from the same physics working group. The second option is favored in the collaboration to optimize the use of resources.

To find the optimal selection criteria and to estimate the acceptance of the detector and the efficiency to measure the signal, we use Monte Carlo (MC) simulations. The events from MC are produced by a special program, in UPC is called STARLIGHT, see 3.1.6, which produces different vector mesons and decaying particles using a simulation of two-photon and photon-Pomeron interactions between relativistic nuclei and protons for each event. Then, the interaction of these particles with the ALICE detector is simulated via another program called GEANT3. The output of GEANT is similar to the raw data. The exact same criteria as for the real data are then applied to the MC events.

5.2 Analysis of the coherent and incoherent photoproduction of J/ψ vector mesons

The analysis in this Master's Thesis uses data taken during Run2 in 2015 with Pb–Pb collisions at $\sqrt{s_{\mathrm{NN}}} = 5.02$ TeV at mid-rapidity $|y| < 0.9$ using data collected with the ITS, TPC, V0, AD, TOF and ZDC detectors with ALICE. The data sample used are from the LEGO train UD_PbPb_AOD, run 398, period LHC15o. For the analysis of the photoproduction of the J/ψ vector meson were also used the Monte Carlo (MC) data LHC18b14. The processes used in this thesis are following:

- kCohJpisToMu
- kCohJpsitoElRad
- kIncohJpsiToMu
- kIncohJpsiToElRad
- kCohPsi2sToMuPi
- kCohPsi2sToElPi
- kIncohPsi2sToMuPi
- kIncohPsi2sToElPi

where the type of the process is indicated by the name.

It is known that the simulation of the TOF trigger inputs in the MC is not describing the data due to various issues with the trigger efficiency during the data taking. Study of these issues is still ongoing. Due to its complexity was considered to be out of the scope of this thesis. The original sample contained some 14 million events while after the train preselection the sample had about 1.3 million events. Because some runs did not accomplish quality standards, they were rejected. In Table 5.1 you can find the complete list of good runs used in this thesis.

5.3 Global event selection

Since the analysis is provided at mid-rapidity, there was selected a special trigger class CCUP8-B dedicated to trigger UPC events in central barrel. The trigger class consists of the following trigger inputs: *0VBA *0VBC *0UBA *0UBC 0STP 0OMU;

- * = negation,
- 0VBA = signal in V0A in beam-beam (BB) window,
- 0VBC = signal in V0C in BB window,
- 0UBA = signal in ADA in BB window,
- 0UBC = signal in ADC in BB window,
- 0STP = SPD topological trigger, where are required at least two tracklets (pairs of fired SPD chips) back-to-back in azimuth,
- 0OMU = Between 2 and 6 TOF pad triggered with at least two pads in a back-to-back topology in azimuth.

List of good runs:
244975, 244980, 244982, 244983, 245064, 245066, 245068, 245145, 245146, 245151, 245152, 245231, 245232, 245259, 245343, 245345, 245346, 245347, 245349, 245353, 245396, 245397, 245401, 245407, 245409, 245410, 245411, 245441, 245446, 245450, 245453, 245454, 245496, 245497, 245501, 245504, 245505, 245507, 245535, 245540, 245542, 245543, 245544, 245545, 245554, 245683, 245692, 245700, 245702, 245705, 245738, 245775, 245793, 245829, 245831, 245833, 245923, 245949, 245952, 245954, 246001, 246003, 246012, 246036, 246037, 246042, 246048, 246049, 246052, 246053, 246087, 246089, 246113, 246115, 246151, 246152, 246153, 246178, 246180, 246181, 246182, 246185, 246217, 246222, 246225, 246271, 246272, 246275, 246276, 246424, 246428, 246431, 246434, 246487, 246488, 246493, 246495, 246750, 246751, 246757, 246758, 246759, 246760, 246763, 246765, 246766, 246804, 246805, 246807, 246808, 246809, 246810, 246844, 246845, 246846, 246847, 246851, 246928, 246945, 246948, 246980, 246982, 246984, 246989, 246991, 246994

Table 5.1: Table of good runs.

5.4 AD and V0 vetoes

Although the CCUP8-B trigger has already included veto for any activity in the forward detectors AD and V0, we repeat this requirement also offline. The coherent photoproduction of J/ψ vector meson is an exclusive process, where only decay particles are present at the detector. For this reason, since the study is provided at mid-rapidity, additional veto to forward region activity is necessary. In Fig. 5.1 is shown the correlation of AD and V0 detector offline decisions in events with the CCUP8-B trigger. The decisions are depicted as 4 classes, where each class represents different AD or V0 decision, see for explanation Table 5.2. Our interest is in class 0, which means the detectors were empty. As seen on Fig. 5.1, it is indeed necessary to apply an offline veto against activity in the forward region.

Class	Explication
0	No timing measurement V0 and AD detector
1	Time in Beam-Beam (BB) window
2	Beam-Gas collision (BG)
3	Fake signal - Timing measurement but out of both BB and BG window

Table 5.2: The different offline decisions of AD and V0 detectors in different classes.

Due to the presence of high and low multiplicity hadronic events in Pb–Pb collisions there was observed the time slewing, as seen in diagram on Fig. 5.2, causing that the wide time-versus-charge distribution couldn't be covered whole in the proper time window of AD and V0 electronics, which is 14 ns. This explains the behavior in Fig. 5.1. To solve this feature the V0 was setup to cover all high charges and not vetoing low multiplicities, while AD was setup in opposite way. It covered low multiplicity hadronic events and

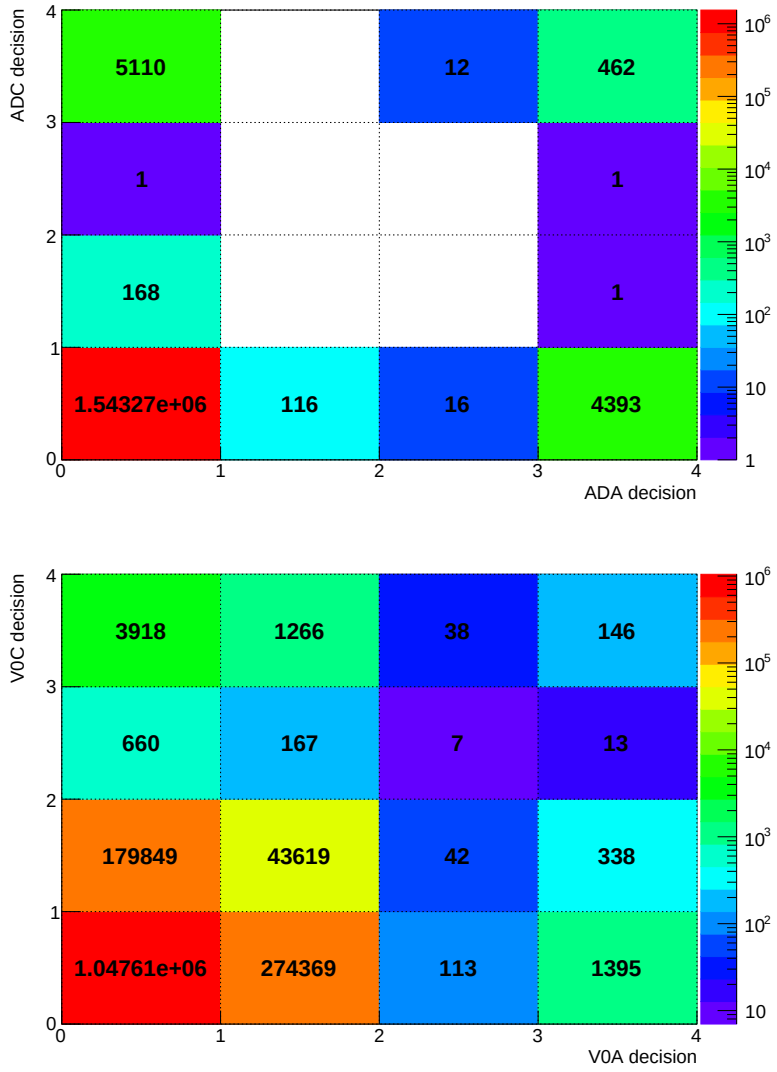

Figure 5.1: Correlations of the offline trigger decisions in the CCUP8 triggered events; ADA vs ADC (top) and V0A vs V0C (bottom).

missing higher ones.

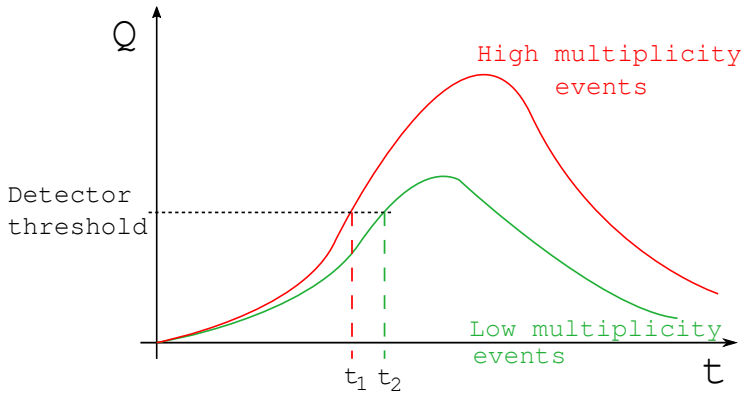

Figure 5.2: The scheme of time slewing in V0 and AD detectors with charge Q as a function of time t. With a given threshold the high multiplicity events, depicted with red line, trigger an earlier signal at t_1, while the low multiplicity events, shown with a green line, trigger a signal at $t_2 > t_1$ with the same threshold.

5.5 Selection of tracks

In this Thesis we are studying the vector meson J/ψ decaying into two leptons, muons and electrons in coherent and incoherent photoproduction at mid-rapidity. Since, as was mentioned already, is the exclusive photoproduction, i.e. in the central barrel are only decay particles in an otherwise empty detector, the requirement of exactly two tracks takes place. These two tracks have to have opposite charges to avoid a hadronic background which would come from like-sign events. The additional criterion for the transverse momentum is applied and it raises from the kinematics of the J/ψ. Since with its mass of about 3.1 GeV/c^2 decays almost at rest to muons or electrons with masses about ∼105 Mev/c^2 or ∼0.5 MeV/c^2, respectively, at least one of the leptons should have transverse momentum larger than 1 GeV/c.

To distinguish between the two channels, we use the TPC particle identification (PID) by their energy loss dE/dx. We suppose that muons and electrons are within 3 σ of the muon or electron PID hypothesis. Here σ means the resolution of the measurement of the dE/dx at a given particle momentum, see Fig. 5.3.

The coherence and incoherence of the photoproduction is mainly distinguished by the transverse momentum of the vector meson J/ψ. We studied the p_{T} distribution in Monte Carlo and decided to cut p_{T} below 200 MeV/c for coherent events and above $p_{\mathrm{T}} > 200$ MeV/c for incoherent events for both channels, see Fig. 5.4. The green line at value $p_{\mathrm{T}} = 200$ MeV/c is border between the coherent and incoherent photoproduction. The p_{T} distribution is then shown by blue and red line for coherent and incoherent process, respectively.

To assure that we are reconstructing the vector meson J/ψ at mid-rapidty, we select the range to be $|y| < 0.9$. After that we select for invariant mass of J/ψ. In case of J/$\psi \to \mu^-\mu^+$ the selection was (2.8 GeV/$c^2 < M_{\mathrm{inv}} <$ 3.2 GeV/c^2) and for J/$\psi \to e^-e^+$ we used (2.6 GeV/$c^2 < M_{\mathrm{inv}} <$ 3.5 GeV/c^2). The list of used cuts can be seen in Table 5.3.

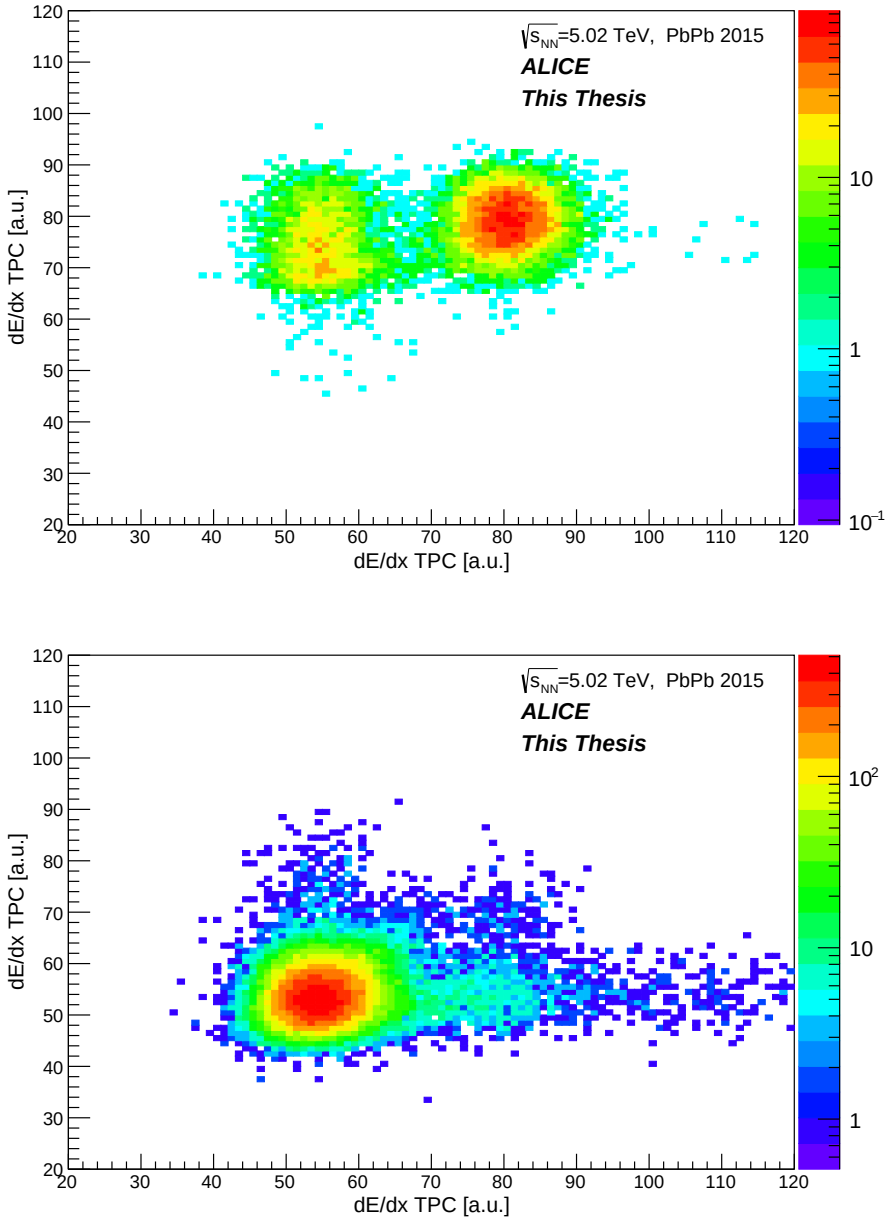

Figure 5.3: Energy loss $\mathrm{d}E/\mathrm{d}x$ of electrons (top) and of muons (bottom) both after the PID cut.

Cut	$\mathrm{J}/\psi \to \mu^-\mu^+$	$\mathrm{J}/\psi \to e^-e^+$
Trigger CCUP8-B	1553548	1553548
AD and V0 veto	1041498	1041498
Opposite-sign	733970	733970
At least one $p_\mathrm{T} > 1$ GeV	71087	71087
PID TPC $< 3\sigma$	53153	12423
p_T of coh/inc J/ψ	7223/45930	5323/7100
Cut for inv. mass of J/ψ	2323/1070	2520/1236

Table 5.3: Event statistics at various stages of the data selection.

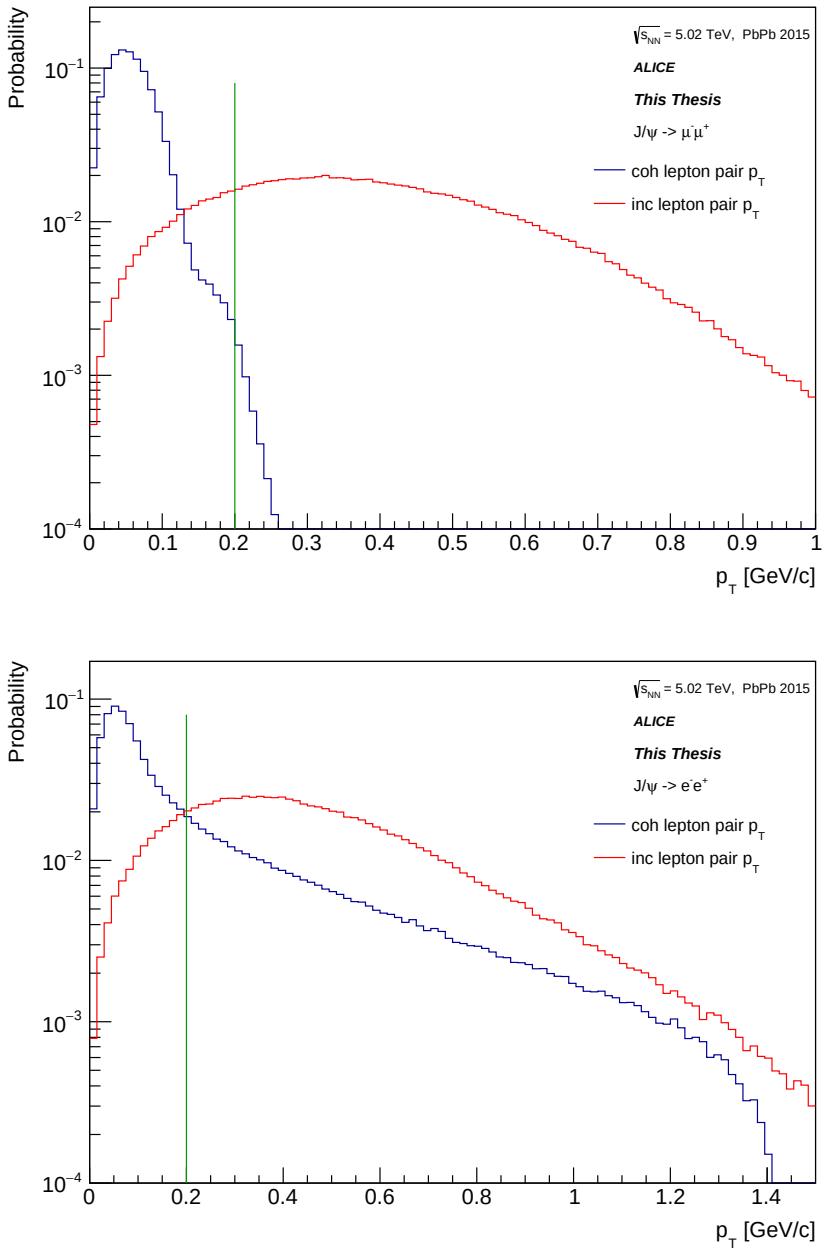

Figure 5.4: p_{T} distribution of lepton pairs of muons (top) and electrons (bottom) from Monte Carlo reconstructed tracks. The red line represents the transverse momentum of incoherent photoproduction of J/ψ, while the blue line the coherent one. The green line is the cut to distinguish the coherent photoproduction of the incoherent. Distributions are normalized to unity.

5.6 The extraction of the J/ψ signal

To extract the signal of J/ψ from the invariant mass spectrum we used the most common model describing the J/ψ peak, the Crystal Ball function. It consists of a Gaussian core with a power law and exponential tail described by parameters α and N. These two parameters are very sensitive to background and is difficult to determine them correctly. We fixed the values of N and α to the ones found in MC. Besides the α and N parameters, Crystal Ball contains another two parameters, mean $m_{\mathrm{J}/\psi}$ and $\sigma_{\mathrm{J}/\psi}$ which were left free in a fit of data. To fit data we included an exponential function to describe the background from continuous l^+l^- production. Fig. 5.5, 5.6, 5.7 and 5.8 show distributions of invariant mass of J/ψ for each channel studied in this Thesis with corresponding Monte Carlo fit and their parameters. The $\mathrm{N}_{\mathrm{J}/\psi}$ is the resulting yield of the J/ψ obtained from the fit.

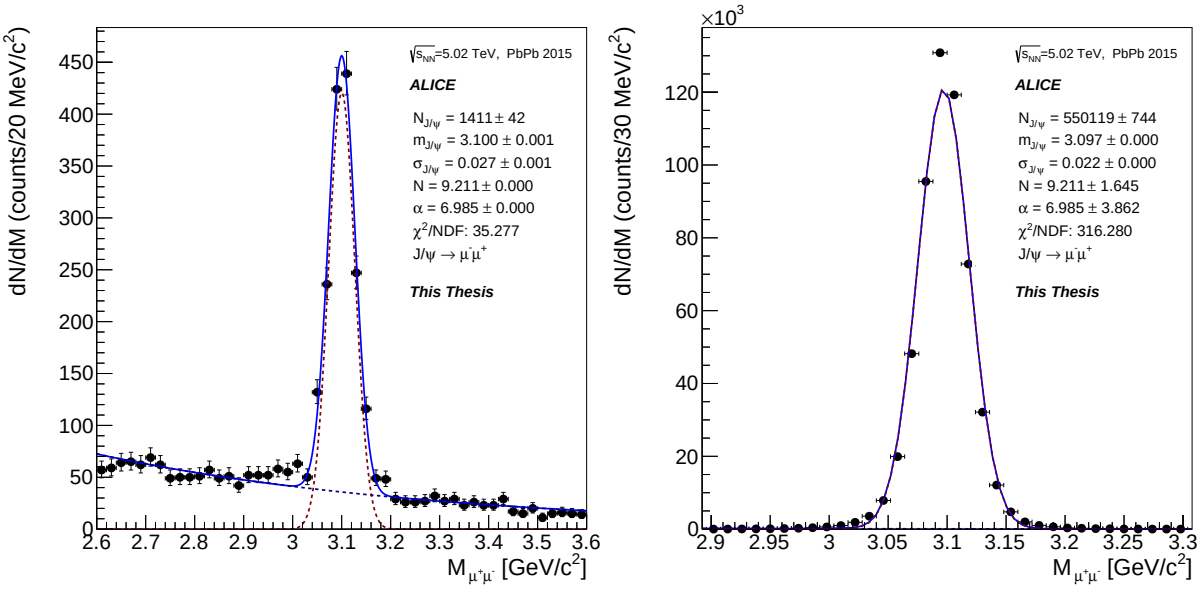

Figure 5.5: Invariant mass distributions of the J/ψ candidates in the coherent sample (left) and MC (right). The fitting function and results of the fit are shown.

5.7 Calculation of the cross section

The differential cross section is calculated in this Thesis as in Eq. (5.1)

$$\frac{\mathrm{d}\sigma^{\mathrm{coh/inc}}_{\mathrm{J}/\psi}}{\mathrm{d}y} = \frac{N^{\mathrm{coh/inc}}_{\mathrm{J}/\psi}}{(A\times\epsilon)_{\mathrm{J}/\psi} BR(\mathrm{J}/\psi\to l^-l^+)\mathscr{L}_{\mathrm{int}}\Delta y}, \tag{5.1}$$

where $N^{\mathrm{coh/inc}}_{\mathrm{J}/\psi}$ is the yield of coherent/incoherent J/ψ, $(A\times\epsilon)_{\mathrm{J}/\psi}$ is the acceptance and efficiency of J/ψ, $BR(\mathrm{J}/\psi\to l^-l^+)$ is the corresponding branching ratio, which can be found in Table 5.6, $\mathscr{L}_{\mathrm{int}}$ is integrated luminosity and Δy is the rapidity region.

5.7.1 Coherent and incoherent yield $\mathrm{N}^{\mathrm{coh/inc}}_{\mathrm{J}/\psi}$

The extracted yield from the fit in Fig. 5.5, 5.6, 5.7 and 5.8 is not pure coherent/incoherent yield of J/ψ. It is measured yield and it contains fractions from feed down, in case

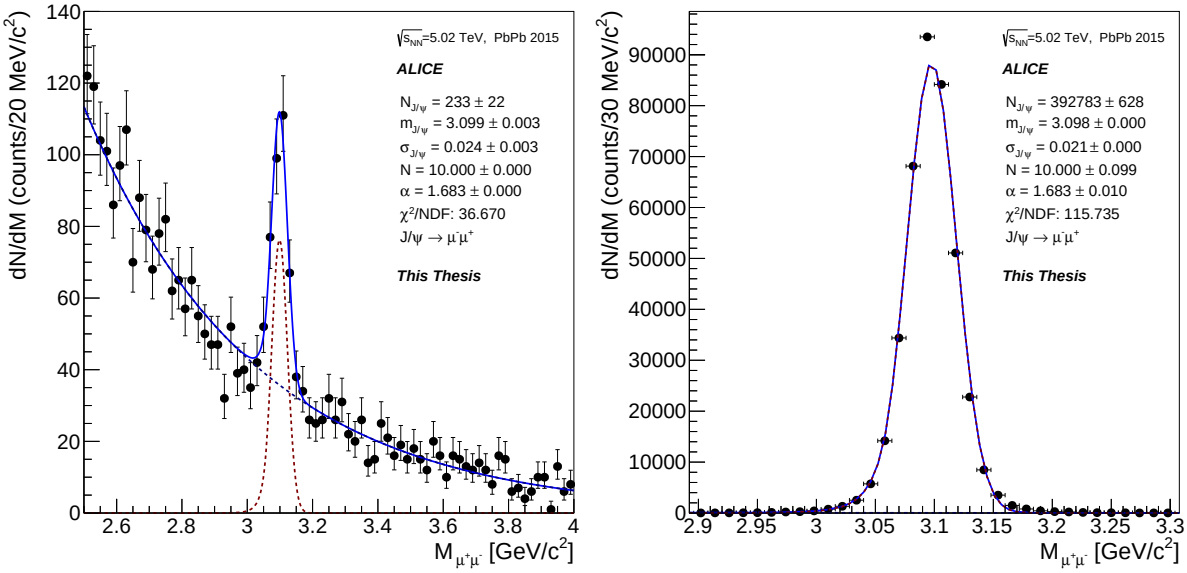

Figure 5.6: Invariant mass distributions of the J/ψ candidates in the incoherent sample (left) and MC (right). The fitting function and results of the fit are shown.

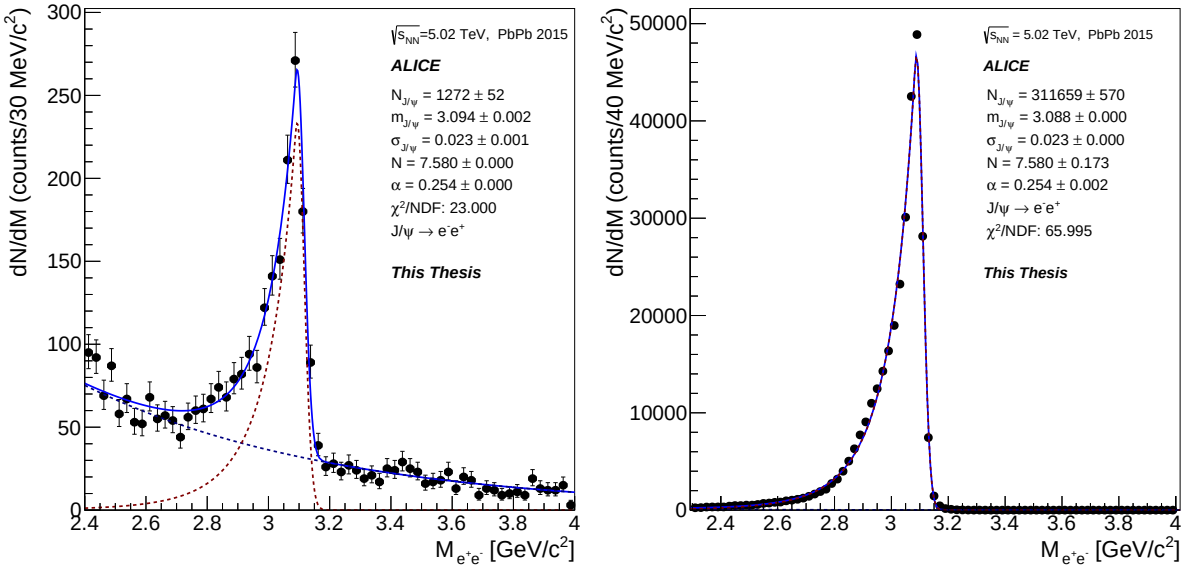

Figure 5.7: Invariant mass distributions of the J/ψ candidates in the coherent sample (left) and MC (right). The fitting function and results of the fit are shown.

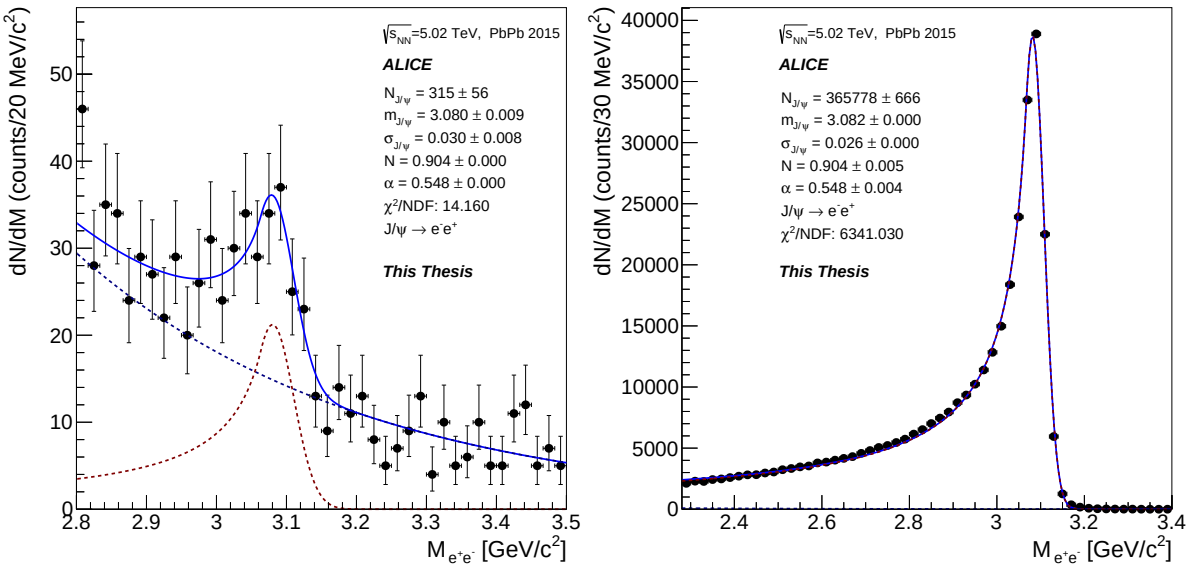

Figure 5.8: Invariant mass distributions of the J/ψ candidates in the incoherent sample (left) and MC (right). The fitting function and results of the fit are shown.

of coherent photoproduction contains also incoherent contamination of J/ψ events and analogously is for the incoherent yield from fit, thus the measured yield can be expressed as sum of each contribution

$$N^{\text{measured}} = N^{\text{coh}} + N^{\text{inc}} + N^{\text{feed down}}. \tag{5.2}$$

Here in Eq. (5.2) $N^{\text{feed down}}$ is a contribution from the decay of ψ(2S) into J/ψ + anything. Usually J/ψ is accompanied by 2 neutral or charged pions with low transverse momenta and thus they are not detected by ALICE. For this reason, the contribution to the measured yield must be corrected for the feed down, which can be expressed as a sum of the "charged" and "neutral" feed down part.

f_I and f_C corrections

The relation between incoherent and coherent yield can be written through the f_I fraction as

$$f_I = \frac{N^{\text{inc}}}{N^{\text{coh}}}, \tag{5.3}$$

and that from the feed down through fraction f_D

$$N^{\text{feed down}} = f_D^{\text{neutral}} N^{\text{coh}} + f_D^{\text{charged}} N^{\text{coh}}. \tag{5.4}$$

Analogously, these relations can be written for the coherent fraction in incoherent measured yield through the f_C fraction as in Eq. (5.5)

$$N^{\text{coh}} = f_C N^{\text{inc}}. \tag{5.5}$$

Putting all expresions from Eq. (5.3, 5.4) in Eq. (5.2), we obtain a formula for the final corrected coherent yield

$$N^{\text{measured}} = N^{\text{coh}}(1+f_I+f_D^{\text{neutral}}+f_D^{\text{charged}}) \rightarrow N^{\text{coh}} = \frac{N^{\text{measured}}}{1+f_I+f_D^{\text{neutral}}+f_D^{\text{charged}}}, \quad (5.6)$$

and in analogy with Eq. (5.6) we can write down the expression for the incoherent yield

$$N^{\text{inc}} = \frac{N^{\text{measured}}}{1+f_C+f_D^{\text{neutral}}+f_D^{\text{charged}}}. \quad (5.7)$$

We relate the measured events to the reconstructed by Monte Carlo simulations. Using the experimental cross section from Eq. (5.8)

$$\sigma = \frac{N_{J/\psi}^{measured}}{(A\times\epsilon)_{J/\psi} BR(J/\psi \rightarrow l^- l^+)\mathscr{L}_{int}} \quad (5.8)$$

and expressing f_I from Eq. (5.3) we obtain a formula for the correction on incoherent fraction f_I in Eq. (5.10).

$$f_I = \frac{_{meas}N^{inc}}{_{meas}N_{coh}} = \frac{_{rec}N_{J/\psi}^{inc}}{_{rec}N_{J/\psi}^{coh}} = \frac{\sigma^{inc}}{\sigma^{coh}} \frac{(A\times\epsilon)_{J/\psi}^{inc} BR(J/\psi \rightarrow l^- l^+)\mathscr{L}_{int}\Delta y}{(A\times\epsilon)_{J/\psi}^{coh} BR(J/\psi \rightarrow l^- l^+)\mathscr{L}_{int}\Delta y}, \quad (5.9)$$

which after the simplification leads to

$$f_I = \frac{\sigma_{J/\psi}^{inc}}{\sigma_{J/\psi}^{coh}} \frac{(A\times\epsilon)_{J/\psi}^{inc}}{(A\times\epsilon)_{J/\psi}^{coh}}. \quad (5.10)$$

In this case, $\sigma_{\text{J}/\psi}^{inc} = 5.247$ mb and $\sigma_{\text{J}/\psi}^{coh} = 12.504$ mb were taken from STARLIGHT.

The $(A\times\epsilon)_{J/\psi}^{inc}$ from Eq. (5.10) is acceptance and efficiency calculated in a region of p_{T} lower than 200 MeV/c dividing number of reconstructed incoherent J/ψ events by the incoherently generated events from Monte Carlo simulations.

The $(A\times\epsilon)_{J/\psi}^{coh}$ is classical acceptance and efficiency of the J/ψ, which will be introduced later on.

The correction on coherent fraction f_C in incoherent yield is in Eq. (5.11)

$$f_C = \frac{\sigma_{J/\psi}^{coh}}{\sigma_{J/\psi}^{inc}} \frac{(A\times\epsilon)_{J/\psi}^{coh}}{(A\times\epsilon)_{J/\psi}^{inc}}, \quad (5.11)$$

where $(A\times\epsilon)_{J/\psi}^{coh}$ is calculated in incoherent transverse momentum region $p_{\text{T}} > 200$ MeV/c.

In the Table 5.4 are summarized results of calculated fractions. The value of f_C (J/$\psi \rightarrow e^- e^+$) is $\sim$ 57%, which is due to strong radiative effects in decay containing electrons. These effects were included in Monte Carlo simulation, which can be also seen in distribution of the transverse momentum for this decay channel in Fig. 5.4 (lower panel). In comparison to the p_{T} distribution of muon pairs, p_{T} of coherent pairs drops rapidly, while the distribution of electron pairs drops constantly for coherent and incoherent lepton pairs after the cut in $p_{\text{T}} = 200$ MeV/c. There are indeed seen roughly 57 % of coherent events in expected incoherent region.

	Value
f_I ($J/\psi \to \mu^-\mu^+$)	0.0630 ± 0.0002
f_I ($J/\psi \to e^-e^+$)	0.0793 ± 0.0004
f_C ($J/\psi \to \mu^-\mu^+$)	0.0126 ± 0.0003
f_C ($J/\psi \to e^-e^+$)	0.5720 ± 0.0020

Table 5.4: The calculated values of corrections on coherent and incoherent fractions f_I and f_C.

f_D correction

As was mentioned already, we have to account also for the contamination from the feed down, which has two contributions, one becoming from $\psi(2S) \to J/\psi + \pi^-\pi^+$ and other from $\psi(2S) \to J/\psi +$ neutrals. The first fraction can be estimated using STARLIGHT as

$$f_D^{\text{charged}} = \frac{\sigma_{\psi(2S)} BR(\psi(2S) \to J/\psi + \pi^-\pi^+) A \times \epsilon_{(\psi(2S)\to J/\psi)}}{\sigma_{J/\psi} A \times \epsilon_{(J/\psi)}}. \tag{5.12}$$

Since the neutral pions can not be detected, the acceptance and efficiency for the feed down of J/ψ will be the same as for the primary J/ψ, thus formula in (5.12) will be simplified due to cancellation of the same factors

$$f_D^{\text{neutral}} = \frac{\sigma_{\psi(2S)} BR(\psi(2S) \to J/\psi + \text{neutrals})}{\sigma_{J/\psi}}. \tag{5.13}$$

The necessary terms are summarized in Table 5.5.

	Value
$\sigma^{\text{coh}}_{J/\psi}$ (STARLIGHT)	12.504 mb
$\sigma^{\text{inc}}_{J/\psi}$ (STARLIGHT)	5.247 mb
$\sigma^{\text{coh}}_{\psi(2S)}$ (STARLIGHT)	2.52 mb
$\sigma^{\text{inc}}_{\psi(2S)}$ (STARLIGHT)	0.92 mb

Table 5.5: Total cross sections calculated by STARLIGHT.

	Value
$BR(\psi(2S) \to J/\psi + neutral)$	25.37 %
$BR(\psi(2S) \to J/\psi + \pi^-\pi^+)$	34.67 %
$BR(J/\psi \to \mu^-\mu^+)$	5.93 %
$BR(J/\psi \to e^-e^+)$	5.94 %

Table 5.6: Total branching ratios for different decay channels of J/ψ and $\psi(2S)$. Taken from [28].

The acceptance and efficiency of the feed of $J/\psi + \pi^-\pi^+$ can be found in Fig. 5.9 and 5.10.

The total values of feed down, i.e. the sum from the charged and neutral contributions are summarized in Table 5.7.

From the fit in Fig. 5.5, 5.6, 5.7 and 5.8 we found the number of measured J/ψ events and using Eq. (5.6, 5.7) with values from Tables 5.4 and 5.7 we have prepared everything

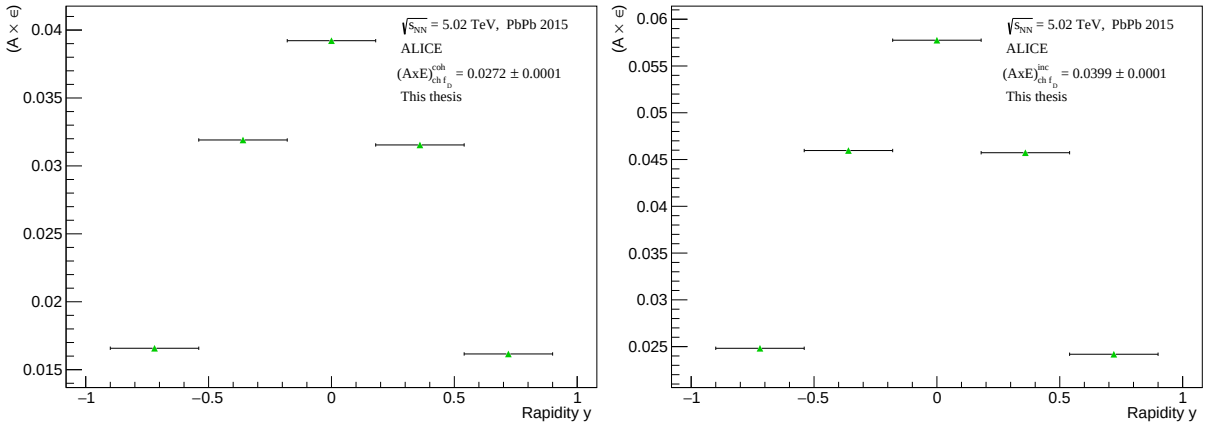

Figure 5.9: The feed down efficiency of coherent (left) and incoherent (right) $\psi(2S) \to J/\psi + \pi^-\pi^+$, where $J/\psi \to \mu^-\mu^+$.

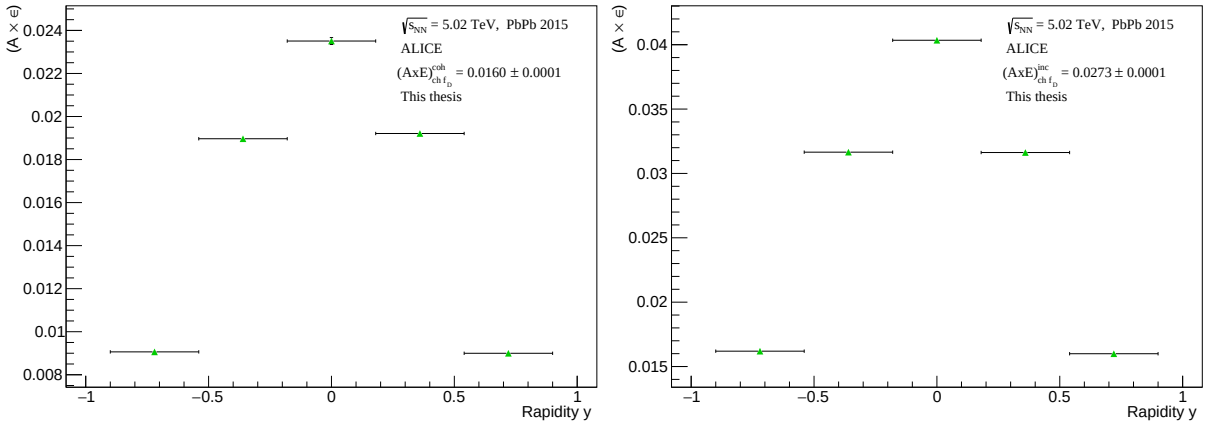

Figure 5.10: The feed down efficiency of coherent (left) and incoherent (right) $\psi(2S) \to J/\psi + \pi^-\pi^+$, where $J/\psi \to e^-e^+$.

	Feed down of $J/\psi \to \mu^-\mu^+$	Feed down of $J/\psi \to e^-e^+$
f_D coherent	0.08036 ± 0.00009	0.06646 ± 0.00007
f_D incoherent	0.0978 ± 0.0002	0.06844 ± 0.00008

Table 5.7: The summarized values of calculated corrections for feed down, where $f_D = f_D^{\text{charged}} + f_D^{\text{neutral}}$.

for final estimation of the coherent and incoherent J/ψ events, which can be found in Table 5.8.

Channel	Corrected number $N_{\mathrm{coh}}^{\mathrm{J}/\psi}/N_{\mathrm{inc}}^{\mathrm{J}/\psi}$
Coherent J/$\psi \to \mu^-\mu^+$	1234 ± 37
Coherent J/$\psi \to e^-e^+$	1110 ± 45
Incoherent J/$\psi \to \mu^-\mu^+$	209 ± 20
Incoherent J/$\psi \to e^-e^+$	192 ± 34

Table 5.8: The corrected number of J/ψ for both lepton channels in coherent and incoherent photoproduction.

5.7.2 Acceptance and efficiency $(A \times \epsilon)_{\mathrm{J}/\psi}$

With Monte Carlo simulations we can study how efficient was our detector, i.e. the study of how many candidates of coherent and incoherent J/ψ we have lost due to the imperfection of the detector and it's determined by the so-called acceptance and efficiency by Eq. (5.14)

$$(A \times \epsilon)_{\mathrm{J}/\psi} = \frac{\#\text{reconstructed events in } y}{\#\text{generated events in } y}. \tag{5.14}$$

It is determined as a ratio of number of reconstructed J/ψ events, i.e. generated collision passed through the simulated detector layout, over the number of generated J/ψ events and is seen in Fig. 5.11 and 5.12.

When doing this ratio, we assume the correctness of the Monte Carlo. However, due to the previously mentioned issues with the TOF trigger efficiency, we decided to study the ratio of incoherent cross section over the coherent since we expect that the problematic part of the efficiency, the single-hit efficiency in TOF, is the same for coherent and incoherent events and thus will cancel out in the ratio. We know that due to different kinematics (different p_{T}) of the coherent and incoherent J/ψ the azimuthal opening angle between the decay product will be different. To take into account a possible difference in the response of the topological part of the TOF trigger for coherent and incoherent event which will not cancel out in the ratio we performed the following study.

5.7.3 Study of $\Delta\varphi$ distribution

The TOF input trigger is set to trigger events which has at least two pads fired in the region between 150° and 180°. That means that we have to study how many tracks from coherent photoproduction hit this region in TOF and how much it varies from the case of incoherent photoproduction of J/ψ. For this study we use generated events from Monte Carlo.

In Fig. 5.13 and 5.14 can be seen the $\Delta\varphi$ distributions from coherent and incoherent photoproduction of J/ψ normalized to number of entries for both channels. Then we integrated the region of $\Delta\varphi \in (150°, 180°)$ and looked at the differences between this two types of photoproduction. The resulting values are in Table 5.9 and as already seen from figures, the two distributions are not similar, they differ by $\sim 15\%$. We have to bear it in mind when doing the ratio of the cross sections.

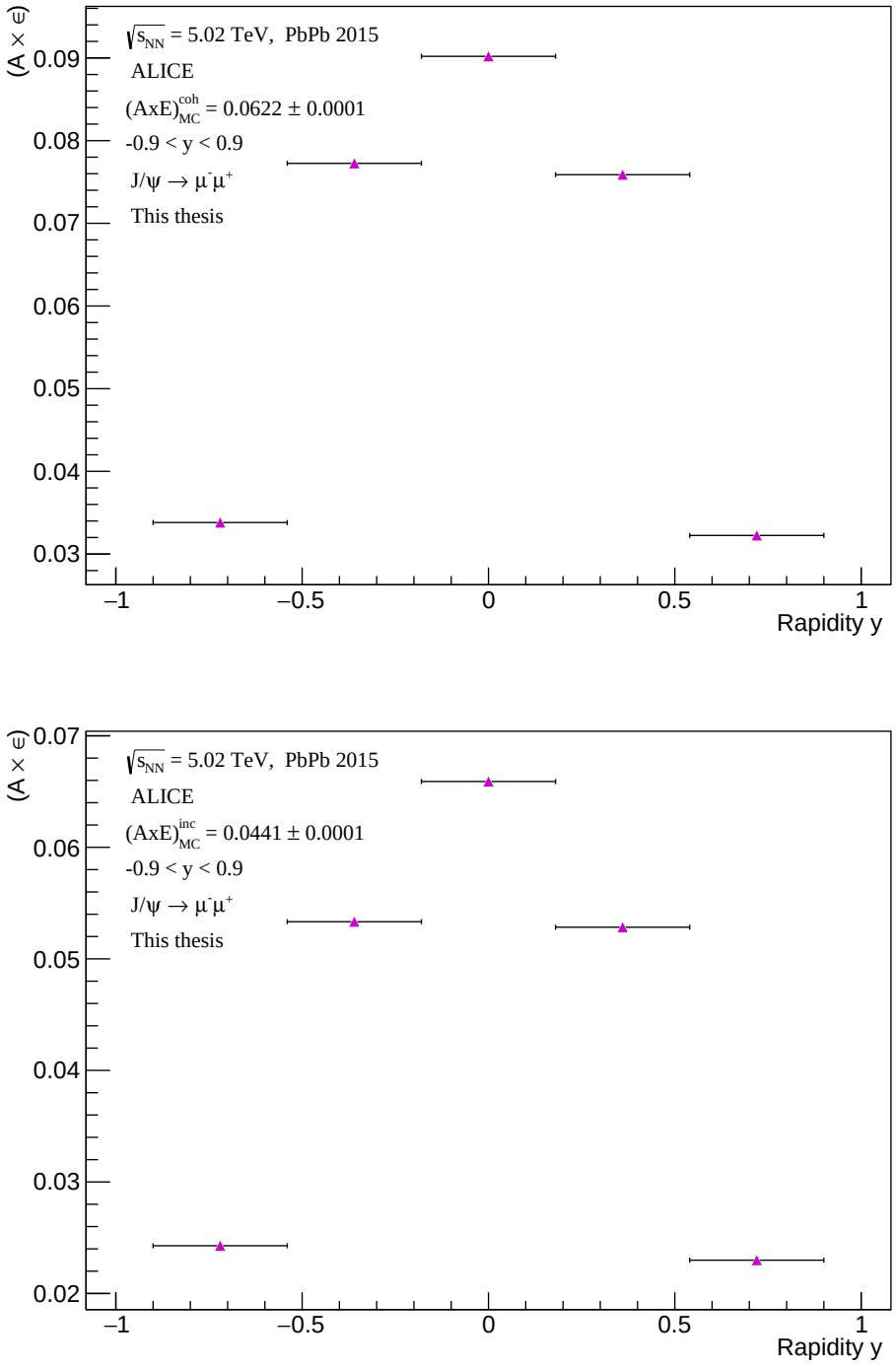

Figure 5.11: On this figure is depicted the acceptance and efficiency ($A \times \epsilon$) of coherent (top) and incoherent (left) $\mathrm{J}/\psi \to \mu^-\mu^+$.

$\Delta\varphi \in (150°, 180°)$	$\mathrm{J}/\psi \to \mu^-\mu^+$	$\mathrm{J}/\psi \to e^-e^+$
Coherent	99.74 %	99.75 %
Incoherent	84.70 %	84.76 %

Table 5.9: The table with integrated values of $\Delta\varphi \in (150°, 180°)$ distributions of two tracks coming from coherently and incoherently produced J/ψ.

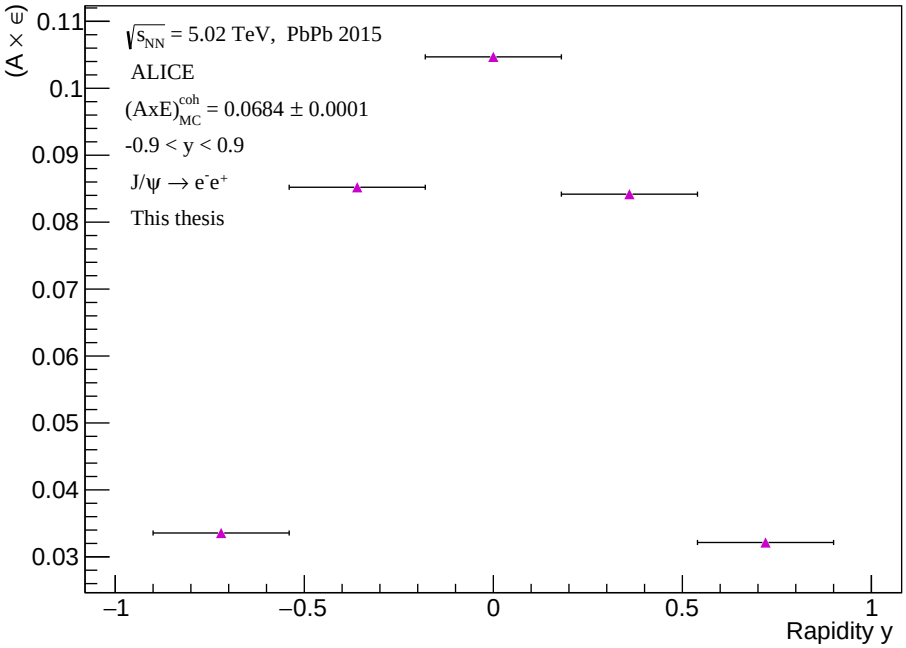

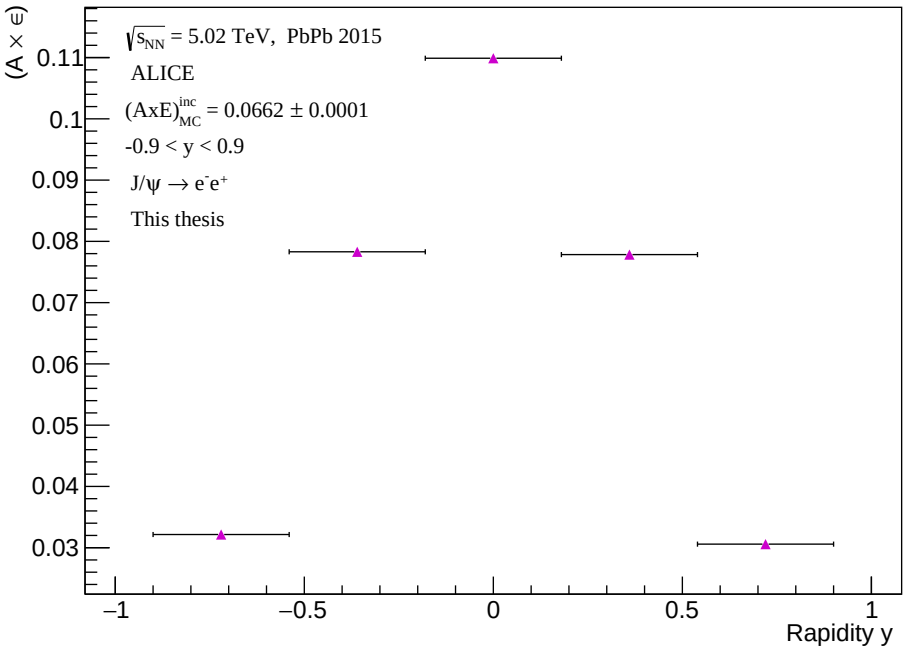

Figure 5.12: On this figure is depicted the acceptance and efficiency ($A \times \epsilon$) of coherent (top) and incoherent (left) $J/\psi \to e^- e^+$.

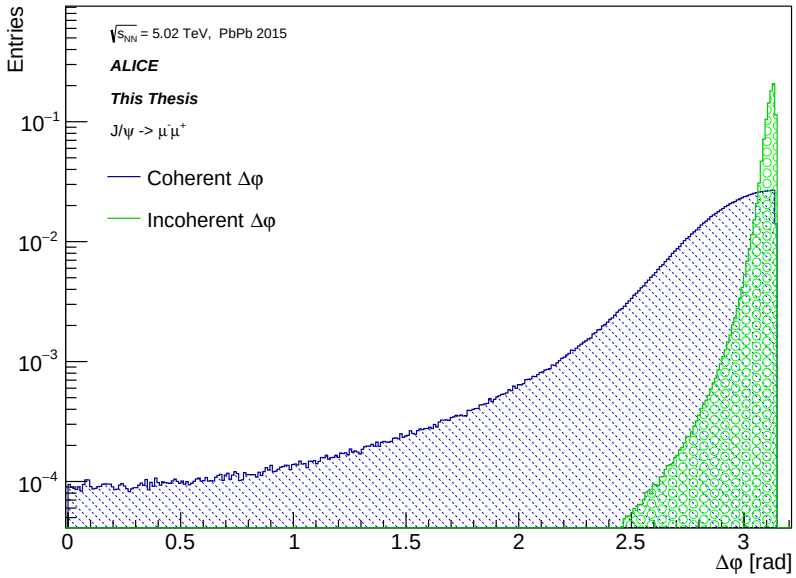

Figure 5.13: Two $\Delta\varphi$ distributions of tracks coming from coherently (blue line) and incoherently (green line) produced J/ψ in muon channel.

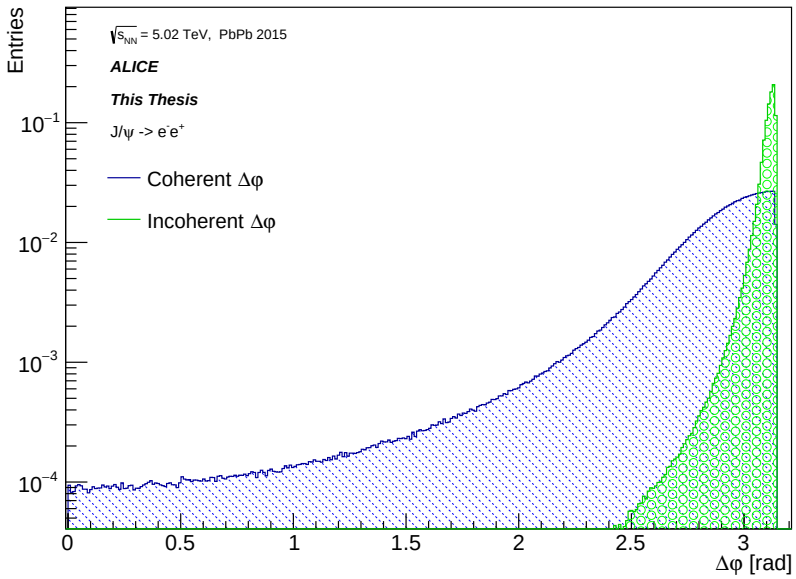

Figure 5.14: Two $\Delta\varphi$ distributions of tracks coming from coherently (blue line) and incoherently (green line) produced J/ψ in electron channel.

5.7.4 Luminosity

Another ingredient to the calculation of the cross section is the integrated luminosity. In Fig. 5.15 can be seen, that it is $\mathscr{L}_{\text{int}} = 110.209\ \mu\text{b}^{-1}$. The underlying concepts on luminosity determination at ALICE are explained in [48].

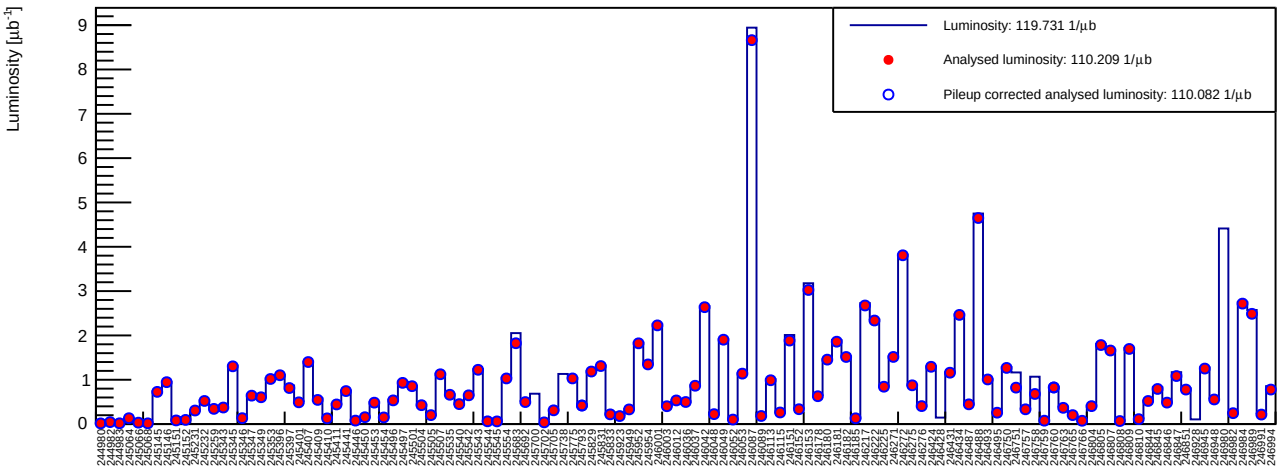

Figure 5.15: The integrated luminosity run-by-run.

5.7.5 The ratio of the cross sections of J/ψ

Now we have prepared every component needed to calculate the ratio of the cross sections of the J/ψ as seen in Eq. (5.1). A summary of the values necessary for the calculation of the ratio can be found in Table 5.10. Putting all information together, we obtained the $\frac{\mathrm{d}\sigma^{\text{inc/coh}}_{\mathrm{J}/\psi}}{\mathrm{d}y}$. The ratio of incoherent cross section over coherent including the correction for the topological trigger is

$$\frac{\mathrm{d}\sigma^{\text{inc}}_{\mathrm{J}/\psi}}{\mathrm{d}y} \Big/ \frac{\mathrm{d}\sigma^{\text{coh}}_{\mathrm{J}/\psi}}{\mathrm{d}y} = (0.28 \pm 0.04\ (\text{stat})) \quad \text{for } \mathrm{J}/\psi \to \mu^-\mu^+ \tag{5.15}$$

and

$$\frac{\mathrm{d}\sigma^{\text{inc}}_{\mathrm{J}/\psi}}{\mathrm{d}y} \Big/ \frac{\mathrm{d}\sigma^{\text{coh}}_{\mathrm{J}/\psi}}{\mathrm{d}y} = (0.20 \pm 0.04\ (\text{stat})) \text{ for } \mathrm{J}/\psi \to \mathrm{e}^-\mathrm{e}^+. \tag{5.16}$$

5.7.6 Systematic error

Since we are interested in the ratio of the cross section, many correlated systematic errors will be canceled. Unique systematic error in [38] which is not correlated is that of extraction of the signal from the fit.

We restricted the area in invariant mass spectrum of lepton pairs around the peak. From the fit was known the background shape, thus integrating over the restricted area and resting the background, we obtained the yield. The half of the difference between this method and the fit is our systematic error, see Table 5.11.

The final ratios with statistical and systematic errors are

$$\frac{\mathrm{d}\sigma^{\text{inc}}_{\mathrm{J}/\psi}}{\mathrm{d}y} \Big/ \frac{\mathrm{d}\sigma^{\text{coh}}_{\mathrm{J}/\psi}}{\mathrm{d}y} = (0.283 \pm 0.040\ (\text{stat}) \pm 0.009\ (\text{sys})) \quad \text{for } \mathrm{J}/\psi \to \mu^-\mu^+ \tag{5.17}$$

	Coh. $J/\psi \to \mu^-\mu^+$	Inc. $J/\psi \to \mu^-\mu^+$	Coh. $J/\psi \to e^-e^+$	Inc. $J/\psi \to e^-e^+$
$N_{\text{corrected}}$	1234 ± 37	209 ± 20	1110 ± 45	192 ± 34
$(A \times \epsilon)$	$6.22 \pm 0.01\%$	$4.41 \pm 0.01\%$	$6.84 \pm 0.01\%$	$6.62 \pm 0.01\%$
$BR(J/\psi \to l^-l^+)$	5.93 %	5.93 %	5.94 %	5.94 %
TOF correction	1.178	1.178	1.177	1.177
Luminosity $\mathscr{L}_{\text{int}}$	110.209 μb^{-1}	110.209 μb^{-1}	110.209 μb^{-1}	110.209 μb^{-1}
Δy	1.8	1.8	1.8	1.8

Table 5.10: Summary of values for the calculation of the ratio of differential cross section as a function of rapidity y for J/ψ vector meson at 2015 Pb–Pb collisions data taking with ALICE.

Chanel	Yield from fit	Yield from analytical method	Systematic error
Coherent $J/\psi \to \mu^-\mu^+$	1411	1445	1%
Incoherent $J/\psi \to \mu^-\mu^+$	233	223	2%
Coherent $J/\psi \to e^-e^+$	1272	1194	3%
Incoherent $J/\psi \to e^-e^+$	315	265	8%

Table 5.11: Table of systematic error of signal extraction for each decay channel.

and

$$\frac{\mathrm{d}\sigma^{\text{inc}}_{J/\psi}}{\mathrm{d}y} \Big/ \frac{\mathrm{d}\sigma^{\text{coh}}_{J/\psi}}{\mathrm{d}y} = (0.20 \pm 0.04\ (\text{stat}) \pm 0.02\ (\text{sys})) \text{ for } J/\psi \to \mathrm{e}^-\mathrm{e}^+, \tag{5.18}$$

and can also be seen in Fig. 5.16.

We also calculated the weighted ratio of differential cross section of coherently and incoherently produced J/ψ vector meson. These two ratios were divided and compared with the value from 2011 [38]. The resulting value is

$$\frac{\mathrm{d}\sigma^{\text{inc}}_{J/\psi}}{\mathrm{d}y} \Big/ \frac{\mathrm{d}\sigma^{\text{coh}}_{J/\psi}}{\mathrm{d}y} = 0.22 \pm 0.02\ (\text{stat} \pm \text{sys}) \tag{5.19}$$

and it can be seen in Fig. 5.17.

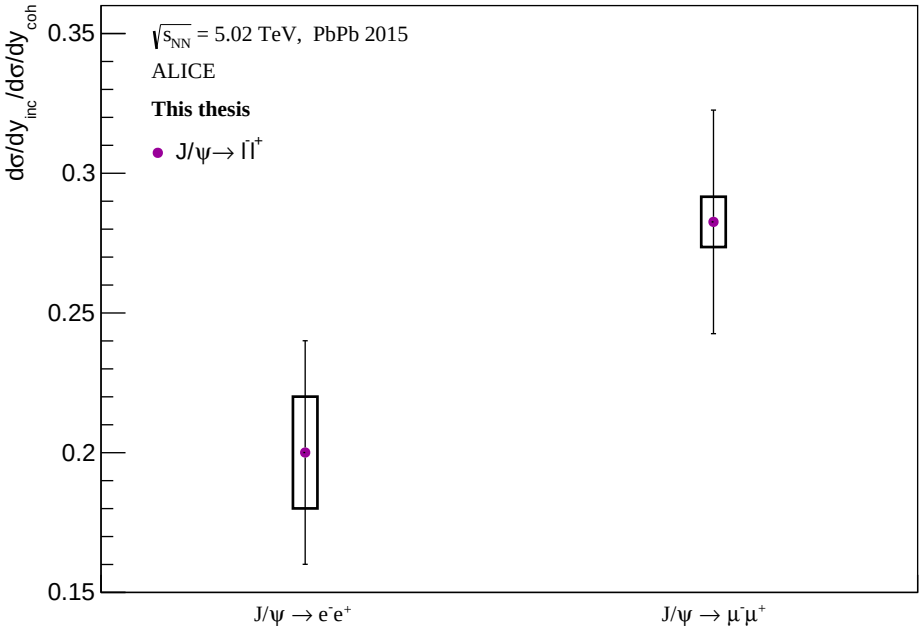

Figure 5.16: Calculated ratios of cross section with Pb–Pb collisions from 2015 data taking at ALICE for the decay channel $J/\psi \to e^- e^+$ (left) and for the $J/\psi \to \mu^- \mu^+$ (right) with systematic error depicted as a box and statistical error bar.

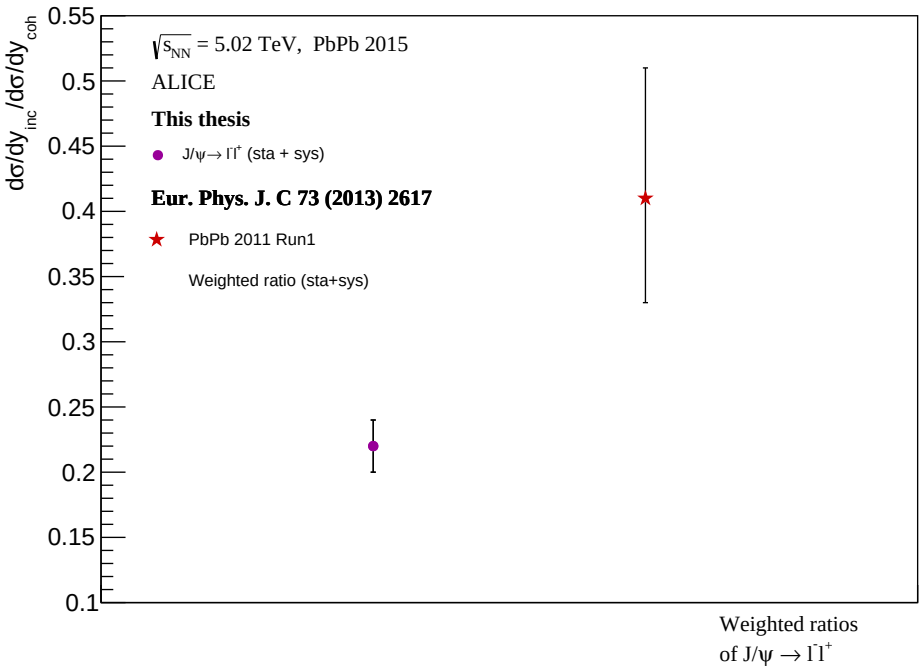

Figure 5.17: Calculated weighted ratios of cross section of J/ψ vector meson with Pb–Pb collisions from 2015 data taking at ALICE. The results are compared to the red point, i.e. the ratio of weighted cross section of J/ψ measured in 2011 Pb–Pb data taking at ALICE [38].

Chapter 6

Summary and Discusion

The motivation for the study of ultra-peripheral collisions is that the cross section is very sensitive to the gluon distribution function in nucleons and nuclei. At the LHC energies we are able to study the small-x physics, where are visible QCD phenomena such as nuclear shadowing. Different models have different theory predictions of the origin of the shadowing and of its evolution through the Q^2 and x. The measurement of the cross section of the photoproduction of the vector meson can constrain or reject some models described in Chapter 3.

In this Master's Thesis we calculated coherent and incoherent photoproduction cross section for lepton channels of vector meson J/ψ, i.e. J/$\psi \to \mu^-\mu^+$ and J/$\psi \to e^-e^+$ at mid rapidity $|y| < 0.9$ using data of Pb-Pb collisions at $\sqrt{s_{\mathrm{NN}}} = 5.02$ TeV measured by ALICE in 2015.

We used Eq. (5.2) to calculate the differential cross section. The selection criteria were applied to data to find potential J/ψ events. The measured yield was extracted by fitting the invariant mass spectrum of the lepton pairs by Crystal Ball function. This yield had to be corrected for the contaminations from feed down f_D coming from ψ(2S) and for contamination of the coherent enriched sample by incoherent events and vice versa. When we compared our measurements in Table 5.4 and 5.5 with [38] in Table 3.1, the f_I of the dimuon channel is in good agreement with [38], for dielectron channel we used different p_{T} cut, thus our value is lower than in [38]. We found large difference in f_C correction between dimuon and dielectron channel. Almost $\sim 57\%$ events form a contamination of the incoherent enriched sample by a coherent events in case of electron channel. This is nicely seen in p_{T} distribution in Fig. 5.4 where coherent and incoherent events decrease with the same slope above p_{T} 0.2 GeV/c. The dielectron channel suffers from strong radiative losses and Monte Carlo simulations included this feature what had as a consequence a large f_C in the dielectron channel. In [38] f_D varies from 4.4% to 11.8% for electrons and for muons varies from 4.3% to 14.7%. In this region are also our measurements, see Table 5.7. After applied corrections, the resulting pure number of J/ψ is shown in Table 5.8.

We studied the acceptance and efficiency of the J/ψ for each decay channel with Monte Carlo simulations. The resulting acceptance and efficiency is shown in Fig. 5.11 and 5.12 and in Table 5.10. These values are obtained as a ratio of the number of reconstructed events, which are events generated by STARLIGHT and passed through the simulated detector layout, over those generated. Since the problem with TOF trigger input, the MC simulation does not describe correctly the trigger and thus it isn't very relevant to compare our values with those values measured in [38]. What is relevant to do, is to study the difference in angle φ between two tracks coming from the primary vertex and to look at the distribution in range of the TOF requirement $\Delta\varphi \in (150°, 180°)$ for each coherent and incoherent photoproduction. If they are similar, then it is interesting to

focus on a ratio of incoherent photoproduction cross section to coherent photoproduction cross section because thus the problematic part will cancel out. Distributions for each channel can be seen in Fig. 5.14, 5.13 and in Table 5.9. Almost $\sim 15\%$ doesn't match and we have to bear in mind this fact when doing the ratio.

Accordingly to the [48] we calculated integrated luminosity in Fig. 5.15.

Finally we computed the cross sections in Table 5.10 and Fig. 5.16 and we estimated the systematic error. Only uncorrelated errors wouldn't cancel out in ratio, thus we studied the correlation of the errors in different channels in [38]. Only that of extraction of signal is uncorrelated and final results can be found in Table 5.11. The ratio for $\mathrm{J}/\psi \to \mu^-\mu^+$ is $\frac{\mathrm{d}\sigma^{\mathrm{inc}}_{\mathrm{J}/\psi}}{\mathrm{d}y} \Big/ \frac{\mathrm{d}\sigma^{\mathrm{coh}}_{\mathrm{J}/\psi}}{\mathrm{d}y} = 0.280 \pm 0.040\ (\mathrm{stat}) \pm 0.009\ (\mathrm{sys})$ and for $\mathrm{J}/\psi \to e^-e^+$ is $\frac{\mathrm{d}\sigma^{\mathrm{inc}}_{\mathrm{J}/\psi}}{\mathrm{d}y} \Big/ \frac{\mathrm{d}\sigma^{\mathrm{coh}}_{\mathrm{J}/\psi}}{\mathrm{d}y} = 0.20 \pm 0.04\ (\mathrm{stat}) \pm 0.02\ (\mathrm{sys})$. We calculated the weighted ratio $\frac{\mathrm{d}\sigma^{\mathrm{inc}}_{\mathrm{J}/\psi}}{\mathrm{d}y} \Big/ \frac{\mathrm{d}\sigma^{\mathrm{coh}}_{\mathrm{J}/\psi}}{\mathrm{d}y} = 0.22 \pm 0.02$ (stat + sys), see Fig. 5.17. It should be noted that the 2011 data [38] are dominated by the statistical uncertainty. The large event sample collected in 2015 data taking significantly decreased the statistical error.

The difference between the measured ratio in [38] $\frac{\mathrm{d}\sigma^{\mathrm{inc}}_{\mathrm{J}/\psi}}{\mathrm{d}y} \Big/ \frac{\mathrm{d}\sigma^{\mathrm{coh}}_{\mathrm{J}/\psi}}{\mathrm{d}y} = 0.41^{+0.1}_{-0.08}$ (stat+sys) and ours is 2.3σ. The value of this ratio predicted by STARLIGHT [35, 38] is in good agreement with that measured in 2011 [38]. However, we are comparing the ratio calculated at double the energy. This difference between 2011 and 2015 data could be either accidental or due to physics caused by higher energy. We have to bear in mind the trigger issues present in 2015 data taking. We tried to solve this problem by calculating the ratio where we hoped, it could cancel out. However, it showed up that it couldn't be canceled completely. We also studied the strange contamination in identification of electrons and muons by its energy loss in TPC, Fig. 5.3. The contamination in muons is negligible, while in electrons is roughly 2%. Further studies would be needed to cross check this residual contamination.

Recently we collected the last 2018 Pb–Pb data in Run2 and its careful study would help us with clearing the situation.

In conclusion, we have prepared necessary steps to measure the differential cross section of coherent and incoherent J/ψ production in Pb–Pb ultra-peripheral collisions. We estimated the cross section for each lepton decay and its ratio and compared it to the previous measurement in [38].

Bibliography

[1] C. G. D., D. J. E., and G. B. M., *The Ideas of Particle Physics*. Cambridge University Press, 2006.

[2] R. P. Feynman, "The behavior of hadron collisions at extreme energies," *Conf. Proc.*, vol. C690905, pp. 237–258, 1969.

[3] R. Barrett and D. Jackson, *Nuclear sizes and structure*. International series of monographs on physics, Clarendon Press, 1977.

[4] J. D. Bjorken, "Asymptotic Sum Rules at Infinite Momentum," *Phys. Rev.*, vol. 179, pp. 1547–1553, 1969.

[5] J. D. Bjorken and E. A. Paschos, "Inelastic Electron Proton and gamma Proton Scattering, and the Structure of the Nucleon," *Phys. Rev.*, vol. 185, pp. 1975–1982, 1969.

[6] C. G. Callan and D. J. Gross, "Crucial Test of a Theory of Currents," *Phys. Rev. Lett.*, vol. 21, pp. 311–313, 1968.

[7] H. D. Politzer, "Reliable Perturbative Results for Strong Interactions?," *Phys. Rev. Lett.*, vol. 30, pp. 1346–1349, 1973.

[8] D. J. Gross and F. Wilczek, "Ultraviolet Behavior of Nonabelian Gauge Theories," *Phys. Rev. Lett.*, vol. 30, pp. 1343–1346, 1973.

[9] M. Klein and R. Yoshida, "Collider Physics at HERA," *Prog. Part. Nucl. Phys.*, vol. 61, pp. 343–393, 2008.

[10] H. Abramowicz *et al.*, "Combination of measurements of inclusive deep inelastic $e^{\pm}p$ scattering cross sections and QCD analysis of HERA data," *Eur. Phys. J.*, vol. C75, no. 12, p. 580, 2015.

[11] "The ZEUS experiment." `http://www.mit.edu/~hasell/DKH_zeus.html`. Accessed: 2018-15-11.

[12] N. Armesto, "Nuclear shadowing," *J. Phys.*, vol. G32, pp. R367–R394, 2006.

[13] Y. V. Kovchegov, "Small x F(2) structure function of a nucleus including multiple pomeron exchanges," *Phys.Rev.*, vol. D60, p. 034008, 1999.

[14] Y. V. Kovchegov, "Unitarization of the BFKL pomeron on a nucleus," *Phys.Rev.*, vol. D61, p. 074018, 2000.

[15] I. Balitsky, "Operator expansion for high-energy scattering," *Nucl.Phys.*, vol. B463, pp. 99–160, 1996.

[16] I. Balitsky, "Factorization and high-energy effective action," *Phys.Rev.*, vol. D60, p. 014020, 1999.

[17] I. Balitsky, "Factorization for high-energy scattering," *Phys.Rev.Lett.*, vol. 81, pp. 2024–2027, 1998.

[18] I. Balitsky, "Effective field theory for the small x evolution," *Phys.Lett.*, vol. B518, pp. 235–242, 2001.

[19] V. Gribov and L. Lipatov, "Deep inelastic e p scattering in perturbation theory," *Sov.J.Nucl.Phys.*, vol. 15, pp. 438–450, 1972.

[20] G. Altarelli and G. Parisi, "Asymptotic Freedom in Parton Language," *Nucl.Phys.*, vol. B126, p. 298, 1977.

[21] Y. L. Dokshitzer, "Calculation of the Structure Functions for Deep Inelastic Scattering and e+ e- Annihilation by Perturbation Theory in Quantum Chromodynamics.," *Sov.Phys.JETP*, vol. 46, pp. 641–653, 1977.

[22] A. J. Baltz, "The Physics of Ultraperipheral Collisions at the LHC," *Phys. Rept.*, vol. 458, pp. 1–171, 2008.

[23] C. A. Bertulani, S. R. Klein, and J. Nystrand, "Physics of ultra-peripheral nuclear collisions," *Ann. Rev. Nucl. Part. Sci.*, vol. 55, pp. 271–310, 2005.

[24] J. G. Contreras and J. D. Tapia Takaki, "Ultra-peripheral heavy-ion collisions at the LHC," *Int. J. Mod. Phys.*, vol. A30, p. 1542012, 2015.

[25] J. J. Aubert *et al.*, "Experimental Observation of a Heavy Particle J," *Phys. Rev. Lett.*, vol. 33, pp. 1404–1406, 1974.

[26] B. Richter, "Discovery of the psi Particles: A Personal Perspective," *SLAC Beam Line. Vol. 7, No. 11. 11/1976*, 1976.

[27] R. J. Gonsalves, "Perturbative QCD at High Energy Colliders," *Int. J. Mod. Phys.*, vol. E17, pp. 870–890, 2008.

[28] "The parton model." `http://pdglive.lbl.gov/Viewer.action`. Accessed: 2018-21-11.

[29] A. Adeluyi and C. A. Bertulani, "Constraining Gluon Shadowing Using Photoproduction in Ultraperipheral pA and AA Collisions," *Phys. Rev.*, vol. C85, p. 044904, 2012.

[30] V. Rebyakova, M. Strikman, and M. Zhalov, "Coherent ρ and J/ψ photoproduction in ultraperipheral processes with electromagnetic dissociation of heavy ions at RHIC and LHC," *Phys. Lett.*, vol. B710, pp. 647–653, 2012.

[31] V. P. Goncalves and M. V. T. Machado, "Vector Meson Production in Coherent Hadronic Interactions: An update on predictions for RHIC and LHC," *Phys. Rev.*, vol. C84, p. 011902, 2011.

[32] A. Cisek, W. Schafer, and A. Szczurek, "Exclusive coherent production of heavy vector mesons in nucleus-nucleus collisions at LHC," *Phys. Rev.*, vol. C86, p. 014905, 2012.

[33] T. Lappi and H. Mantysaari, "$J/|psi$ production in ultraperipheral Pb+Pb and p+Pb collisions at energies available at the CERN Large Hadron Collider," *Phys. Rev.*, vol. C87, no. 3, p. 032201, 2013.

[34] J. Berger and A. M. Stasto, "Small x nonlinear evolution with impact parameter and the structure function data," *Phys. Rev.*, vol. D84, p. 094022, 2011.

[35] S. Klein and J. Nystrand, "Exclusive vector meson production in relativistic heavy ion collisions," *Phys. Rev.*, vol. C60, p. 014903, 1999.

[36] S. Afanasiev *et al.*, "Photoproduction of J/psi and of high mass e+e- in ultra-peripheral Au+Au collisions at s**(1/2) = 200-GeV," *Phys. Lett.*, vol. B679, pp. 321–329, 2009.

[37] B. Abelev *et al.*, "Coherent J/ψ photoproduction in ultra-peripheral Pb-Pb collisions at $\sqrt{s_{NN}} = 2.76$ TeV," *Phys. Lett.*, vol. B718, pp. 1273–1283, 2013.

[38] E. Abbas *et al.*, "Charmonium and e^+e^- pair photoproduction at mid-rapidity in ultra-peripheral Pb-Pb collisions at $\sqrt{s_{\rm NN}}$=2.76 TeV," *Eur. Phys. J.*, vol. C73, no. 11, p. 2617, 2013.

[39] J. Adam *et al.*, "Coherent ψ(2S) photo-production in ultra-peripheral Pb Pb collisions at $\sqrt{s}_{\rm NN} = 2.76$ TeV," *Phys. Lett.*, vol. B751, pp. 358–370, 2015.

[40] V. Khachatryan *et al.*, "Coherent J/ψ photoproduction in ultra-peripheral PbPb collisions at $\sqrt{s_{NN}} = 2.76$ TeV with the CMS experiment," *Phys. Lett.*, vol. B772, pp. 489–511, 2017.

[41] "The large hadron collider: 10 years and counting." `https://home.cern/about/updates/2018/09/large-hadron-collider-10-years-and-counting`. Accessed: 2018-08-10.

[42] "Taking a closer look at LHC." `https://www.lhc-closer.es/taking_a_closer_look_at_lhc/1.lhc`. Accessed: 2018-08-10.

[43] L. Evans and P. Bryant, "LHC Machine," *JINST*, vol. 3, p. S08001, 2008.

[44] "Some LHC milestones.... Quelques dates clés du LHC...," p. 1, Sep 2008. Cover article.

[45] "ALICE." `https://alice-figure.web.cern.ch`. Accessed: 2018-08-10.

[46] K. Aamodt *et al.*, "The ALICE experiment at the CERN LHC," *JINST*, vol. 3, p. S08002, 2008.

[47] W. Leo, *Techniques for Nuclear and Particle Physics Experiments: A How-to Approach*. Springer, 1994.

[48] E. Kryshen, "Luminosity determination for ultra-peripheral triggers in Pb-Pb at $\sqrt{s_{NN}} = 5.02$ TeV," *Analysis Note*. Accessed: 2018-03-12.